TRACE-ELEMENT MODELLING OF MELTING IN SPINEL PERIDOTITES

A thesis presented to the Faculty

of the State University of New York

at Albany

in partial fulfillment of the requirements

for the degree

of Master of Science

College of Arts and Sciences

Department of Geological Sciences

Susanne Petra Vogel

1993

TRACE-ELEMENT MODELLING OF MELTING IN SPINEL PERIDOTITES

Abstract of

a thesis presented to the Faculty

of the State University of New York

at Albany

in partial fulfillment of the requirements

for the degree

of Master of Science

College of Arts and Sciences

Department of Geological Sciences

Susanne Petra Vogel

1993

ABSTRACT

This study addresses three independent topics related to trace element modeling of spinel peridotites that are suggested by the pioneering work of Johnson et al. (1990) on abyssal harzburgites.

First, the fractional non-modal melting equation derived by Johnson and coworkers (1990) is algebraically modified to present a "one-element/two-phase" model. This model suggests a simple test for estimating mantle heterogeneity in the source rock of spinel lherzolites. This model is applied to data from the literature for samples from Dreiser Weiher, Germany; San Luis Potosi, Mexico; and Western Victoria, Australia.

Second, trace elements in clinopyroxenes of abyssal peridotites and continental spinel lherzolite nodules from multiple localities are compared. Plots of Ti versus Zr, Na_2O and REEs show data overlap in their distribution trends, and they are thought to have originated from broadly similar ratios in the source rock prior to partial melting and by generally similar melting processes.

Third, a modal melting (MM) diagram for abyssal peridotites based on the Johnson et al. (1990) melting equation is constructed that illustrates how modal proportions of mineral phases in a spinel-lherzolitic mineral assemblage change as a function of F (degree of melting). In accordance with this model, a method is introduced that allows F to be calculated based solely on the modal composition for a particular sample. This model is "calibrated" with Ti data for Cpx in abyssal harzburgites, and the original mantle composition is calculated at F=0 and compared to other suggested primitive upper mantle compositions. The sensitivity of this diagram to variations in input parameters is also shown. A further calibration with experimentally-established reaction coefficients for the upper mantle melting reaction (Kinzler & Grove 1992a, b; Baker & Stolper 1993) is also carried out in order to test similarities between these two independent approaches. The

calibration shows iterative values for the input parameter are in partial agreement with experimentally-derived reaction coefficients. While the resulting reaction coefficients confirm generation of olivine during melting as suggested by melting experiments, Opx and Cpx reaction coefficients show similar proportions (Cpx/Opx < 1). This observation does not concur with experimentally-determined mantle melt reaction (Cpx/Opx ~ 2 for Kinzler & Grove (1992a) and Baker & Stolper (1993)). A satisfactory link between trace-element modelling and high P-T melting experiments could therefore not be obtained through the MM-model.

ACKNOWLEDGMENTS

This thesis would never have been possible without the knowledge, encouragement and friendship of many people. All of them, my family and friends abroad in Germany as well as Professors and graduate students here in the Department of Geological Science helped me to gain education and experience -- that I never want to miss.

I am most grateful to my advisor Steve DeLong, who has introduced me to the secrets of trace-element modelling in igneous petrology. Innumerable discussions with Steve improved and developed my work invaluably, steered me into the right direction, and gradually changed my initial astonishment for this "kind" of science to an unexpected fascination. I will never forget Steve's encouragement, patience, and humor, which always kept me motivated during the ups and downs of my student-life. Thanks also for the important financial support!

Special thanks go to my committee members Mary Roden and Greg Harper for taking the effort and time to read and improve my thesis.

I also would like to express my thanks to Roger Nielsen and colleges at the Oregon State University at Corvallis who spent time teaching me more about trace-element modelling. My visit to Corvallis was not only an enrichment for my education and personality but it also gave me more confidence to approach my work.

Diane Paton is thanked for always being a caring secretary. Without her, the department would not have been so warm and friendly.

I thank my fellow graduate students, particularly Ben, Andreas, Mike, Michael, Albert (and, of course, his family), Christoph, Chris, Markos, Young-do, Laura, Sue, and Haig for all the fun (and sometimes suffering) we had together.

I consider Heather and Ben as good friends that I will expect, among others, for a visit in Germany. Hopefully soon! Hefty and endless discussions will then be continued. This time with German beer!

During my stay in Albany I could always rely on the mental and financial support of my dear mom and my sisters Ute and Heike, which is highly appreciated.

Finally, I would like to thank Rolf for his caring and understanding in so many ways. Thanks for being around when I needed someone to help me with my nerve-racking computer questions, for cheering me up, especially in the final stage of writing (shocking telephone bills were never regretted) and for being my best friend. Excitement and fun that we shared together on so many trips left me an unforgettable impression of this continent.

TABLE OF CONTENTS

ABSTRACT IV
ACKNOWLEDGMENTS VII
TABLE OF CONTENTS VIII
LIST OF FIGURES X
LIST OF TABLES XII

CHAPTER 1 : INTRODUCTION 1-1

1.1 General Introduction and Previous Work 1-1
1.2 Purpose of Study 1-4

CHAPTER 2 : SAMPLE DESCRIPTION 2-1

2.1 Abyssal Peridotites 2-1
2.2 Spinel Lherzolite Nodules 2-2
2.2.1 Classification of Spinel Lherzolite Nodules 2-2
2.2.2 Avoidance of Mantle Metasomatism in Spinel Lherzolite Nodules 2-4

CHAPTER 3 : ONE-ELEMENT / TWO-PHASE MODEL 3-1

3.1 Theoretical Framework 3-1
3.2 Application to Spinel Lherzolites 3-6
3.2.1 Spinel Lherzolites from Dreiser Weiher, Germany 3-6
3.2.2 Spinel Lherzolites from Xalapasco de La Joya, Mexico 3-7
3.2.3 Spinel Lherzolites from Western Victoria, Australia 3-8
3.3 Results 3-8
3.4 Summary 3-10

CHAPTER 4 : A COMPARATIVE STUDY OF MINOR- AND TRACE-ELEMENTS OF CLINOPYROXENES IN ABYSSAL PERIDOTITES AND SPINEL LHERZOLITE NODULES 4-1

4.1 Introduction 4-1
4.2. Choice of Elements 4-1
4.3 Results 4-5

CHAPTER 5 : MELTING IN ABYSSAL PERIDOTITES 5-1

5.1. Modal Melting Model 5-1
5.1.1 Historical Precedent: The MC-Diagram 5-1
5.1.2 Construction of the MM-Diagram 5-6
5.2 Implications for the MM-Diagram 5-9
5.2.1 Calculation of F 5-9
5.2.2 Calculation of the Starting Composition 5-14
5.2.3 Calculation of the Melt Composition 5-14
5.3 Sensitivity of the MM-Diagram to Model Parameters 5-20
5.3.1 Ti Concentration in Initial Clinopyroxene 5-20
5.3.2 Cpx/Liquid Distribution Coefficient for Ti 5-22
5.3.3 Other Trace-elements as Model Parameters 5-26
5.4 Calibration of the MM-Diagram 5-31
5.4.1 Analysis of Internal Consistency 5-34
5.4.2 Analysis of External Consistency 5-39
5.4.3 Results 5-43

REFERENCES Reference-1

APPENDICES: Appendix-1

A Nomenclature and Abbreviations Appendix-1
B Calculation of F Appendix-2
C Calculation of the Melt Composition Appendix-28

LIST OF FIGURES

Figure		Page
1.1	Location map of dredge locations from American-Antarctic ridge and SW Indian ridge	1-6
1.2	Zr versus Ti in diopside of abyssal peridotites	1-7
3.1	Schematic one-element/two-phase diagram	3-4
3.2	Schematic one-element/two-phase diagram for a heterogeneous starting composition	3-5
3.3	Schematic one-element/two-phase diagram for a homogeneous starting composition	3-5
3.4	One-element/two-phase diagrams of Lanthanum	3-11
3.5	One-element/two-phase diagrams of Cerium	3-12
3.6	One-element/two-phase diagrams of Neodymium	3-13
3.7	One-element/two-phase diagrams of Samarium	3-14
3.8	One-element/two-phase diagrams of Europium	3-15
3.9	One-element/two-phase diagrams of Terbium	3-16
3.10	One-element/two-phase diagrams of Dysprosium	3-17
3.11	One-element/two-phase diagrams of Holmium	3-18
3.12	One-element/two-phase diagrams of Thulium	3-19
3.13	One-element/two-phase diagrams of Ytterbium	3-20
3.14	One-element/two-phase diagrams of Lutetium	3-21
3.15	One-element/two-phase diagrams of Lanthanum	3-22
3.16	One-element/two-phase diagrams of Europium	3-23
3.17	One-element/two-phase diagrams of Lutetium	3-24
3.18	One-element/two-phase diagrams of Chromium	3-25
3.19	One-element/two-phase diagrams of Nickel	3-26
4.1	Ti versus Zr in peridotite clinopyroxenes	4-4
4.2	Ti versus Na_2O in peridotite clinopyroxenes	4-5
4.3	Ti versus Ce in peridotite clinopyroxenes	4-6
4.4	Ti versus Nd in peridotite clinopyroxenes	4-7

4.5	Ti versus Sm in peridotite clinopyroxenes	4-8
4.6	Ti versus Eu in peridotite clinopyroxenes	4-9
4.7	Ti versus Dy in peridotite clinopyroxenes	4-10
4.8	Ti versus Er in peridotite clinopyroxenes	4-11
4.9	Ti versus Yb in peridotite clinopyroxenes	4-12
5.1	MC-diagram	5-3
5.2	Gain and loss models	5-4
5.3	Overlay of diagrams from Figure 5.2	5-5
5.4	MM-diagram for abyssal peridotites	5-8
5.5	Least-squares MM-Model	5-12
5.6	Schematic MM-diagram	5-13
5.7	F versus microprobe analyses of olivine	5-16
5.8	F versus microprobe analyses of orthopyroxene	5-17
5.9	F versus microprobe analyses of clinopyroxene	5-18
5.10	F versus microprobe analyses of spinel	5-19
5.11	Ti concentration in initial clinopyroxene	5-21
5.12 a	MM-diagram recalculated with $D_{Ti} = 0.2$	5-24
5.12 b	MM-diagram recalculated with $D_{Ti} = 0.6$	5-24
5.13 a	F versus CaO in clinopyroxene	5-25
5.13 b	F versus Al_2O_3 in clinopyroxene	5-25
5.14	MM-diagram of Zirconium	5-27
5.15	MM-diagram of Neodymium	5-28
5.16	MM-diagram of Europium	5-29
5.17	MM-diagram of Erbium	5-30
5.18	Reaction coefficients for mantle melting reaction	5-33
5.19	Operation ③ of Table 5.2	5-37
5.20	Operation ⑥ of Table 5.2	5-38
5.21	Distribution coefficient versus modal starting composition	5-41
5.22	Distribution coefficient versus reaction coefficients	5-42
A-1	Sample # versus degree of melting	A-3

LIST OF TABLES

Table		Page
3.1	REE analyses for separate minerals in spinel lherzolites	3-27
3.2	Ni and Cr analyses for separate minerals in spinel lherzolites	3-28
4.1	Ti, Zr and Na_2O analyses in clinopyroxenes	4-13
4.2	Ti and REE analyses in clinopyroxenes	4-15
5.1	Upper mantle starting compositions	5-15
5.2	Internal consistency	5-36
5.3	Modal analyses of abyssal peridotites	5-45
5.4	Microprobe analyses of abyssal peridotites	5-47

1. INTRODUCTION

1.1 General Introduction and Previous Work

The lithospheric mantle is a concentric layer that underlies the crust with a varying thickness of about 60-120 km. In very general terms the lithospheric mantle forms together with the crust the strong outer layer of the Earth that is relatively strong with respect to the asthenosphere. According to plate tectonic theory, the lithosphere is broken into several plates that move about the surface of the earth.

In spite of its inaccessibility there is good evidence to believe that the upper lithospheric mantle is mainly peridotitic. Although seismic s- and p-waves are not uniquely indicative of a peridotitic density (e.g. Anderson 1990), exposures of fossil upper mantle and xenoliths are consistent with this assumption. Such peridotites can be found at the base of ophiolites and within fold belts (the so-called alpine-type or orogenic peridotites); they occur as xenoliths in alkali basalts and kimberlites; and they have been dredged as abyssal peridotites at transform faults of slow spreading ridges.

Mineralogic studies of abyssal peridotites have shown that these rocks are products of a large range of partial melting (Dick et al. 1984; Michael & Bonatti 1985), a process taking place in the zone of upwelling due to adiabatic decompression of ascending mantle lherzolites underneath mid ocean ridges and generating mid-ocean ridge basalts. The molten basaltic fraction extracted from the mantle is emplaced at mid-ocean ridges to form basalts, dolerites, gabbros and other related rocks, which are together form the oceanic crust.

Petrogenetic modeling explores this melting process, and there are two approaches that are useful in this respect: The study of more or less depleted ultramafic rocks of presumably mantle origin, and the study of basaltic magmas which are thought be partial melts from the upper mantle. Such studies ought to be complementary to each other and

are of importance to understand the fractionation of elements during the formation of crust and mantle.

While many studies correlate compositions of experimentally produced liquids to constrain melting processes (e.g. Mysen & Kushiro 1977; Jaques & Green 1980; Takahashi 1986), less has been done on the chemical pattern of abyssal peridotites -the residuals- to evaluate processes involved in igneous differentiation (Dick et al. 1984; Dick 1989; Johnson et al. 1990), because direct information on abyssal peridotites was limited due to the high degree of alteration and scarcity of samples. However, such studies are advantageous insofar as they ought to reflect the complementary relationship to the generation of primary magmas prior to polybaric crystal fractionation, assimilation and mixing of the melt en route to the surface.

It is now generally accepted that the chemistry of fertile upper mantle is similar to Ringwood's pyrolite model (e.g. Jagoutz et al. 1979; Maaloe & Aoki 1977). Thus, it appears from major, minor and trace element considerations of xenolithic, ophiolithic and abyssal peridotites that the lithospheric mantle is "residual", which means that a partial melt has been extracted leaving a more or less depleted mantle behind.

Quantitative modeling of the chemical changes that occur during melting is performed with the partitioning behavior of trace elements. Originally inspired by Schilling & Winchester (1967) and Gast (1968), this method places constraints on the petrogenetic evolution of igneous rocks. Trace elements are used for the following reasons (Wood & Fraser 1977):

① Properties of trace elements such as ionic radii, charge and possible ligand field stabilization are quite different from the major elements in a typical ultramafic mineral assemblage. Therefore, some trace elements are not easily accommodated in the structural sites of these minerals during partial melting and consequently exhibit strong preferences for one phase or the melt.

② Their low concentrations (much less than 1%) allows trace elements to obey Henry's Law, while their changes in abundance do not affect the stoichiometry of any major phase in the system.

③ Their incompatibility can result in changes of trace element concentration over several orders of magnitude during melting processes. This amplification effect provides valuable information about the actual mechanisms of magma generation in the mantle. In a peridotitic mineral assemblage usually clinopyroxene is the host for important trace elements, although present in low modal abundance (e.g. Stosch 1982; Zindler & Jagoutz 1988).

The impetus for this thesis was the study on melting in the oceanic upper mantle by Johnson and coworkers (1990). They reported the first study on trace element concentrations in pyroxenes of abyssal peridotites. Samples have been dredged at a number of fracture zones (Figure 1.1). Their study area covers a geographical length of about 5000 km.

Systematic correlations of trace elements in diopsides, including Ti, Zr and REE, clearly indicate that abyssal peridotites in the vicinity of hot spots have experienced the highest degree of partial melting, as already suggested by Dick et al. (1984) and Michael & Bonatti (1985). Thus, Figure 1.2 shows that the most depleted samples are derived from the Bouvet fracture zone near Bouvet Island, which is presumed to be the surface expression of a hotspot. Figure 1.2 also demonstrates that the changes in the trace element composition can be generally matched by a non-modal fractional melting equation as derived by the authors (variables are explained in Appendix A):

$$\frac{C_i^{CPX}}{C_i^{0,CPX}} = \left[1 - \frac{P\,F}{D_i^0}\right]^{\left(\frac{1}{P}-1\right)} \qquad \text{(Johnson et al. 1990; Eq. A4)}$$

The starting composition for the clinopyroxene was chosen to be the intersection of the fractionation trend with the C1-chondritic ratio Ti/Zr=140. In addition, Figure 1.2 points out that batch melting can not produce enough depletion for Ti and Zr to match the distribution trend.

Further, the Ti-Zr graph describes a fractionation trend with a relatively small degree of heterogeneity in the original mantle source rock as is suggested by the small dispersion of the data points about the fractional melting curve.

1.2 Purpose of Study

This thesis explores three topics in trace element modeling that are suggested by the work of Johnson et al. (1990):

① The mathematical model given by Johnson et al. (1990) to describe partial melting focuses on clinopyroxenes, because this is the primary mineral phase with the greatest abundances of incompatible elements in peridotites and therefore the one for which high quality in situ analyses are readily obtainable. Their results led to diagrams such as Figure 1.2, referred to hereafter as "two-element/one-phase" plots, suggesting a genetic relationship for the abyssal harzburgite suite. Simple mathematical recasting of the Johnson et al. (1990) melting model will be demonstrated which lead to "one element/two phase" plots. Such plots allow a similar approach for spinel lherzolite nodules in order to address parallel questions: Does the same simple model apply to partial melting of the mantle source region for spinel lherzolites sampled by alkaline volcanism on continents? This concept of an "one-element/two-phase" diagram is advantageous insofar as a single element must have experienced the same collective distribution during melting and any secondary alteration within the nodule mineral assemblage.

② The Ti-Zr "two-element/one-phase" plot of Figure 1.2 further indicates that the Ti/Zr ratio in the clinopyroxene of the source rock was presumably very similar for the complete harzburgite suite which covers a large geographic area. In order to broaden the

geographic perspective to this observation, it is planned to examine how trace element data for clinopyroxenes in spinel lherzolites nodules will correlate to data of abyssal peridotites. Such graphs ought to place constraints on the degree of chemical homogeneity for the source rock composition over a global scale. For this purpose an intensive literature survey has been done.

③ A third topic is the elaboration of changes in modal mineralogy of abyssal peridotites as a function of the degree of melting (F). In using the Johnson et al. (1990) melting equation a modal melting (MM) diagram has been developed that demonstrates how weight fractions of the mantle mineral assemblage changes as melting proceeds. Since the melting model is based on the partitioning behavior of trace elements, specifically Ti, this approach offers an independent alternative to experimental melting studies, and its stoichiometric reaction coefficients will be compared to those. Using this MM model, it is also possible to estimate the source rock composition prior to melting, and to calculate F for further samples. In addition, the sensitivity of input parameters will be discussed in order to predict modifications for the MM diagram due to possible improved observations in future work.

Each of these topics is discussed in Chapter 3, 4 and 5, respectively, following a description of the samples in Chapter 2.

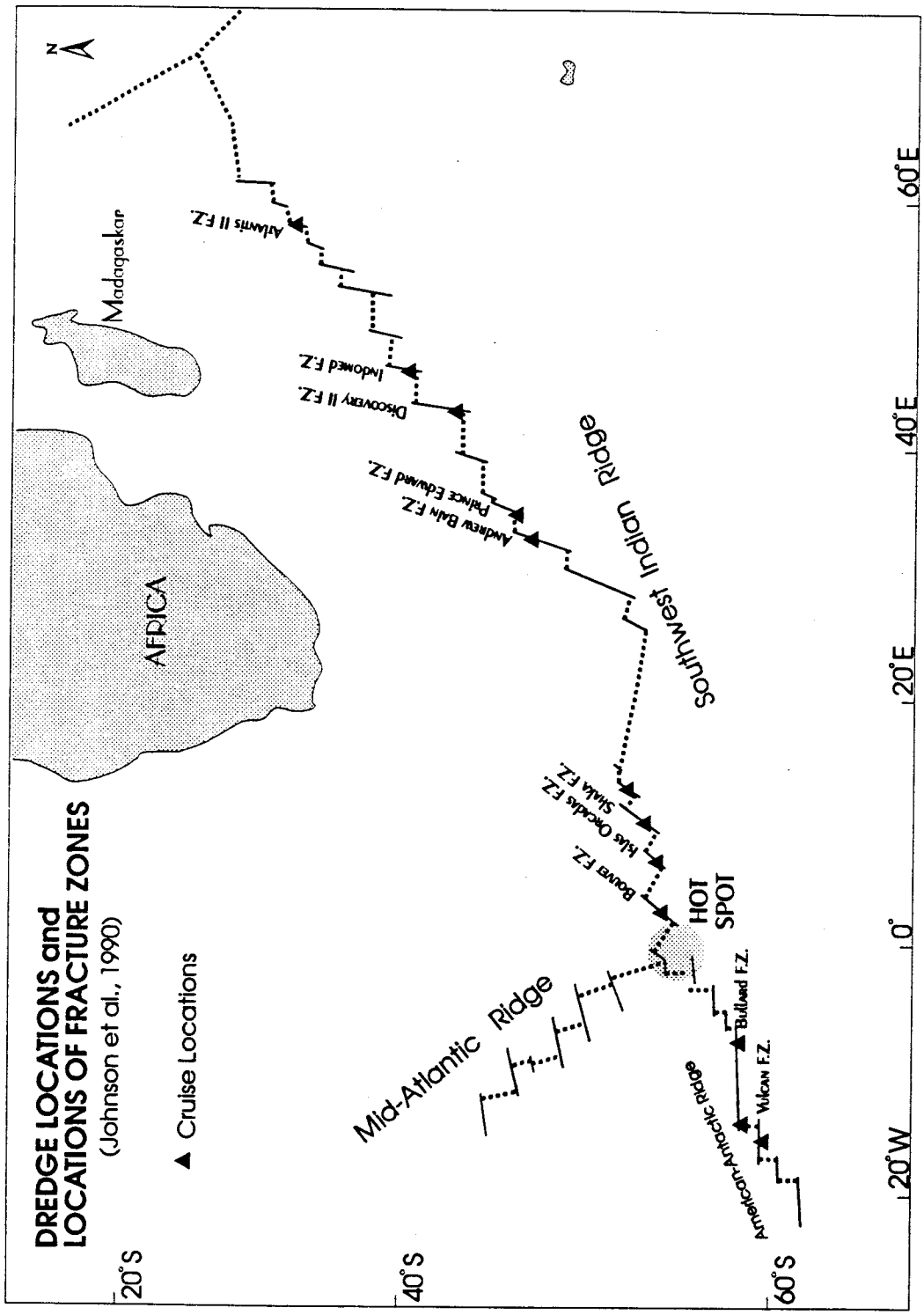

Figure 1.1 **Location map of American-Antarctic ridge and SW Indian ridge showing the location of fracture zones from which abyssal peridotites are derived. Note that the dashed area indicates the vicinity of a presumed hotspot. Map is redrawn from Johnson et al. (1990).**

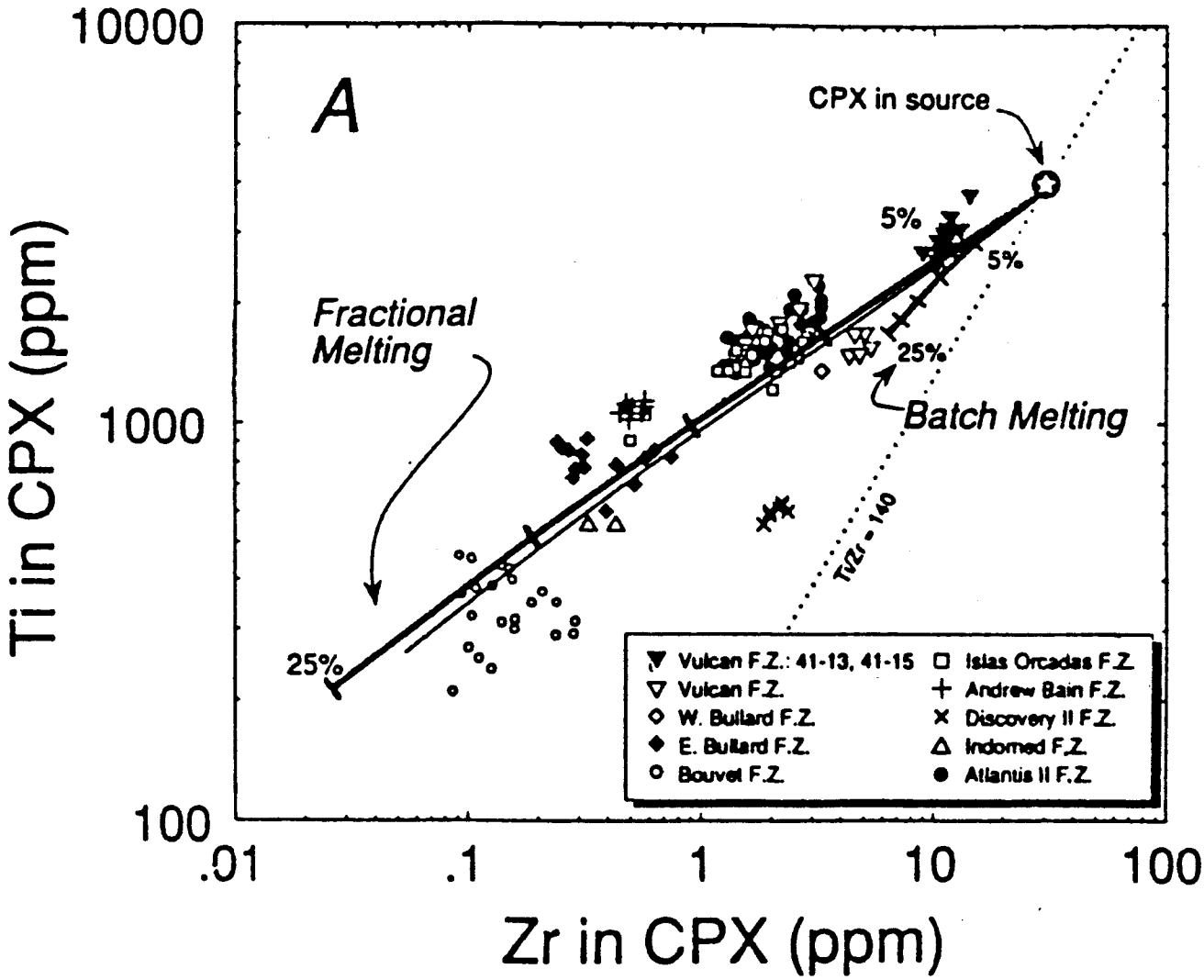

Figure 1.2: **Ti and Zr concentrations in diopsides of abyssal peridotites. Also shown are modal melting curves calculated for fractional and batch melting. The fine line describes a model for melting and segregation in 0.1% increments. Data points conform more closely to a fractionation trend for residues of non-modal near-fractional melting. Diagram is from Johnson et al. (1990).**

2. SAMPLE DESCRIPTION

Data on abyssal peridotites and spinel lherzolites important for this study are exclusively obtained from the literature.

2.1 Abyssal Peridotites

Data on abyssal peridotites are from two recent papers by Dick (1989) and Johnson et al. (1990). These samples represent the uppermost part of the mantle section that has been uplifted along the spreading plate boundaries. The abundance of peridotites and the scarcity of gabbro dredged at very slow slipping fracture zones of the SW Indian and American Antarctic ridge suggests that the crust is extremely thin (Dick 1989).

Abyssal peridotites show either equigranular, protoclastic or porphyroclastic textures which are interpreted to be the result of plastic deformation during and after melting. They are highly altered rocks with 20-100% serpentine replacing olivine and pyroxene (Dick et al. 1984). Olivine is often altered to clay. These structural and mineralogical changes in the constituents of abyssal peridotites defines them as metamorphic rocks. Because of high degree of alteration, abyssal peridotites have crustal seismic velocities (i.e., change from "mantle" to "crust" during serpentinization).

There is still an uncertainty in the petrogenesis of plagioclase in abyssal peridotites. Plagioclase is rarely a residual phase in these rocks, and its existence is interpreted to be caused by a late impregnation with basaltic liquid (Dick et al. 1984; Dick 1989). Therefore, only plagioclase-free samples are included in the data set. The modal analysis for an average abyssal peridotites contains 75% forsteritic olivine, 21% enstatite, 3.5% augite and 0.5% Cr-Al-spinel (Dick, 1989). Clinopyroxene exhibits some degree of exsolution, with generally less than 10% orthopyroxene. Apart from this inhomogeneity, the minerals appear to be unzoned. In spite of the high degree of alteration to serpentine and clay (70-80%, according to Dick et al. 1984), chemical analysis of relict primary minerals and very careful and detailed modal analysis can be made of original phase

abundances because alteration products form characteristic pseudomorphs after the primary phases.

2.2 Spinel Lherzolite Nodules

2.2.1 Classification of Spinel Lherzolites

Data on spinel lherzolite nodules collected for this study are from various papers and have a world-wide distribution. Several attempts have been made to classify the geochemistry (Frey & Green 1974; Wilshire & Shervais 1975; Frey & Prinz 1978; Dawson 1983) and textures (Mercier & Nicolas 1974; Harte 1976) of ultramafic nodules.

Frey & Green (1974) first came to the conclusion that the majority of Victoria, Australia, lherzolite inclusions were formed as partial melting residues. However, they recognized inconsistencies between LILE abundance trends and the abundance trends for major and compatible trace elements and proposed a model with two independent upper mantle components. Component A as the major volume component is residual and determines the major element composition. Component B forms only a small volume but can enrich the LIL and trace element abundance dramatically. In their opinion, this component originated as a melt of garnet peridotite that migrated upwards into the overlying spinel lherzolite field.

Another classification was suggested by Wilshire & Shervais (1975). They divided ultramafic xenoliths from the Western United States into Al-augite and Cr-diopside groups. The Al-augite group is characterized by Al, Ti-rich augites with Fe-rich olivines and orthopyroxenes, whereas the Cr-diopside group has Cr-rich clinopyroxenes and Mg-rich olivine and pyroxene. Both groups have subtypes, but the Cr-diopside group is presumed to have formed the country rock of the Al-augite series.

Frey & Prinz (1978) classified xenoliths from San Carlos, Arizona into group I and group II, which are generally similar to the Cr-diopside and Al-augite group of Wilshire &

Shervais (1975), respectively. In analogy with alpine massifs it is likely that the group 1 spinel lherzolite is volumetrically the most important lithology in their source region (Wilshire et al. 1988; Irving 1980).

Mercier & Nicolas (1974) identified three structural types of spinel lherzolites. In their opinion, the protogranular group shows the "oldest" texture and is mainly due to a crystallization process which took place during partial melting. This texture can grade by plastic flow under shear stress into the second group, called the porphyroclastic. The third group with an equigranular texture has been developed by a complete recrystallization of the porphyroclastic group. Again, all three groups are defined generally and exhibit transitional stages.

The terminology of Harte's study (1976) emphasizes descriptive rather than genetic elements, but the main textural types are very similar to Mercier & Nicolas' (1974) study. The protogranular texture is supposed to show the smallest effect of late-stage recrystallization and reequilibration associated with deformation and the formation of brittle-ductile shear zones accompanying shallow level emplacement of the peridotite.

All spinel lherzolites studied here belong to Group I of Frey & Prinz (1978) and have a protogranular texture as defined by Mercier & Nicolas (1974), unless identified otherwise.

2.1.2 Avoidance of Mantle Metasomatism in Spinel Lherzolite Xenoliths

Geochemical data for spinel lherzolites must be treated with caution in petrogenetic modelling, because such rocks are often affected by subsequent open system processes including extraction or impregnation with a silicate melt or contact with a volatile-rich fluid, now frequently called mantle metasomatism (e.g. Roden & Murthy 1985). Spinel lherzolites showing such secondary enrichment have to be avoided, because their chemical compositions may involve fundamental problems in mass balance calculations, especially for trace elements. According to Dawson (1984) metasomatic

effects in mantle derived ultramafics are of two types. They may show a "patent" metasomatic effect that introduces hydrous mineral phases such as amphibole and/or phlogopite; or a "cryptic" enrichment took place where only incompatible elements document this process. Direct evidence for cryptic metasomatism is often observed as LREE and incompatible element enrichment of nodules which are otherwise depleted in basaltic constituents (Ca, Al, Fe) due to partial melting (Frey & Prinz 1978; Wilshire 1984).

Mantle metasomatism is still an incompletely understood process, where both the extend of the metasomatic agent (melt or volatile) as well as its origin and composition are uncertain (Roden & Murthy 1985; Schneider & Eggler 1986). My selection of literature data restricts the collection to samples that are clearly and explicitly described as anhydrous, if not noted different.

3. ONE-ELEMENT / TWO-PHASE MODEL

3.1 Theoretical Framework

As discussed in 2.2.2, mass balance modeling with trace elements in upper mantle samples often involves uncertainties due to possible open-system (e.g., mantle metasomatism) and temperature-dependent partitioning. Therefore, it is a potential drawback of the approach of Johnson et al. (1990) that their Zr-Ti plot considers changes in two elements (see Figure 1.2) which may behave differently. In principle, the same mathematics applies to any phase, so that a similar equation can be derived for any one element of interest in two distinct phases (e.g. olivine and clinopyroxene). It is a truism that the state of a particular mantle nodule will be fixed and all of its constituents will have shared the same collective melting history. Therefore, it is both algebraically and geologically simpler to look at one-element/two-phase diagrams. For this approach some recasting of the mathematics is necessary.

The basic melting equations for trace element variation in melt and whole-rock residue derived by Gast (1968) and Shaw (1970) were modified by Johnson and coworkers (1990) to describe the change in concentration of two trace elements in clinopyroxene. In this chapter, those equations are further modified to derive an expression that describes the behavior of one trace element in two mineral phases (after S.E.DeLong, pers.comm.). Variables are explained in Appendix A.

The starting mass balance equation for Johnson et al. (1990) was:

$$(1) \qquad \frac{C_i^{Solid}}{C_i^{O}} = \frac{X_i^{Ol} C_i^{Ol} + X_i^{Opx} C_i^{Opx} + X_i^{Cpx} C_i^{Cpx} + X_i^{Sp} C_i^{Sp}}{X_i^{O,Ol} C_i^{O,Ol} + X_i^{O,Opx} C_i^{O,Opx} + X_i^{O,Cpx} C_i^{O,Opx} + X_i^{O,Sp} C_i^{O,Sp}}$$

which can be re-written as:

(2)

$$\frac{C_i^{Solid}}{C_i^{O}} = \frac{\left(\frac{C_i^{Cpx} C_i^{Liquid}}{C_i^{Cpx}}\right)\left(X^{Ol}\frac{C_i^{Ol}}{C_i^{L}} + X^{Opx}\frac{C_i^{Opx}}{C_i^{L}} + X^{Cpx}\frac{C_i^{Cpx}}{C_i^{L}} + X^{Sp}\frac{C_i^{Sp}}{C_i^{L}}\right)}{\left(\frac{C_i^{O,Cpx} C_i^{O,Liquid}}{C_i^{O,Cpx}}\right)\left(X^{O,Ol}\frac{C_i^{O,Ol}}{C_i^{O,L}} + X^{O,Opx}\frac{C_i^{O,Opx}}{C_i^{O,L}} + X^{O,Cpx}\frac{C_i^{O,Cpx}}{C_i^{O,L}} + X^{O,Sp}\frac{C_i^{O,Sp}}{C_i^{O,L}}\right)}$$

This leads to:

$$(3) \qquad \frac{C_i^{Solid}}{C_i^{O}} = \frac{C_i^{Cpx}}{C_i^{O,Cpx}} \frac{\left(C_i^{Liquid}/C_i^{Cpx}\right)}{\left(C_i^{O,Liquid}/C_i^{O,Cpx}\right)} \frac{D_i}{D_i^{O}}$$

Assuming constant $D_i^{Cpx/Liquid}$, that is,

$$(4) \qquad D_i^{Cpx/Liquid} = \frac{C_i^{Cpx}}{C_i^{Liquid}} = \frac{C_i^{O,Cpx}}{C_i^{O,Liquid}} = const.,$$

then:

$$(5) \qquad \frac{C_i^{Solid}}{C_i^{O}} = \frac{C_i^{Cpx}}{C_i^{O,Cpx}} \frac{D_i}{D_i^{O}}$$

The same recasting can be done for any phase, so that:

$$(6) \qquad \frac{C_i^{Solid}}{C_i^O} = \frac{C_i^{Ol}}{C_i^{O,Ol}}\frac{D_i}{D_i^O} = \frac{C_i^{Opx}}{C_i^{O,Opx}}\frac{D_i}{D_i^O} = \frac{C_i^{Cpx}}{C_i^{O,Cpx}}\frac{D_i}{D_i^O} = \frac{C_i^{Sp}}{C_i^{O,Sp}}\frac{D_i}{D_i^O}$$

Because the state (original concentrations, melting history, etc.) of a particular portion of the mantle will be the same regardless of which pair of phases one looks at, then, for example:

$$(7) \qquad \frac{C_i^{Cpx}}{C_i^{O,Cpx}}\frac{D_i}{D_i^O} = \frac{C_i^{Ol}}{C_i^{O,Ol}}\frac{D_i}{D_i^O} \qquad \text{or} \qquad C_i^{Cpx} = \left(\frac{C_i^{O,Cpx}}{C_i^{O,Ol}}\right)C_i^{Ol}$$

Eq. (7) describes a line whose slope is positive and equal to the ratio of the abundances of element *i* in *Cpx* and *Ol* in the source and whose intercept is the origin for a suite of nodules from a source that was homogeneous in $\left(C_i^{O,Cpx}/C_i^{O,Ol}\right)$. This suggests the use of diagrams to provide simple tests for geochemical heterogeneity of the mantle source region from which the nodules were extracted. More specifically, the one-element/two-phase equation predicts that a plot of C_i^{PhaseA} versus C_i^{PhaseB} should be linear with slope $\left(C_i^{O,PhaseA}/C_i^{O,PhaseB}\right)$ and pass through the origin for a suite of nodules from a source that was homogeneous in $\left(C_i^{O,PhaseA}/C_i^{O,PhaseB}\right)$ (see Figure 3.1). The plot is parametric in F, so that one can map out the individual C_i^{PhaseA} and C_i^{PhaseB} variation from the fractional melting equation (Johnson et al. 1990; Eq. A4):

$$C_i^{PhaseA} = C_i^{O,PhaseA}\left(1-\frac{PF}{D_i^0}\right)^{\left(\frac{1}{P}-1\right)}$$

$$C_i^{PhaseB} = C_i^{O,PhaseB}\left(1-\frac{PF}{D_i^0}\right)^{\left(\frac{1}{P}-1\right)}$$

(Equation (7) could have been derived simply by dividing one of these equations by the other, thereby canceling the parenthetic terms of F. The derivation given above running from Equation (1) to (7) has the advantage, however, of making it clear that the concentration change of element i in each phase, expressed by the ratio $(C_i^{Phase}/C_i^{O,Phase})$, depends on the same constant ratio of the bulk $D's(D_i/D_i^0)$.)

For particular values of D_i^O, F will change systematically along the curve. Changes in D_i^O and P (weighted fraction of melt) can compress or extend the tick marks in F, but will not change the position or slope of the line. Therefore, a petrogenetically related suite of nodules will be linear if the source was homogeneous in $\left(C_i^{O,PhaseA}/C_i^{O,PhaseB}\right)$, even if the extraction of melt varied.

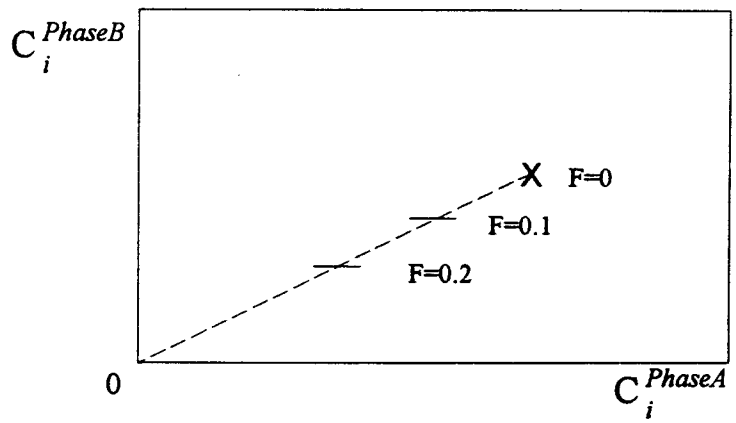

Figure 3.1: **Schematic one-element/two-phase diagram assuming that the starting composition was homogeneous for element *i*.**

A simple graphical test of "local" heterogeneity in the starting upper mantle composition would be to analyze many nodules from a single locality.

Theoretically, there are two extreme possibilities (Figures 3.2, 3.3).

①

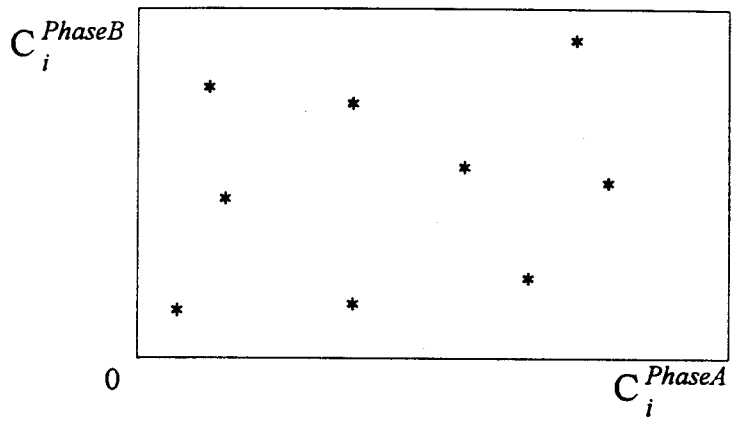

Figure 3.2: **Heterogeneous trace element abundance for element *i* in the source rock composition of a xenolith population.**

②

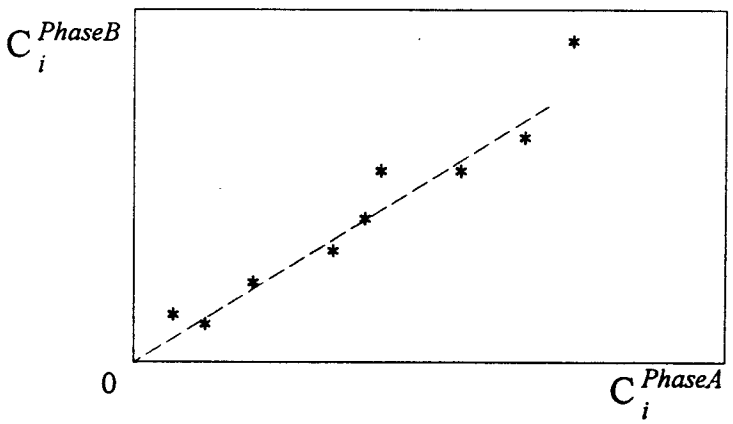

Figure 3.3: **Homogeneous trace element abundance element *i* in the source rock composition of a xenolith population.**

Consequently, in an ideal field situation, where many contemporaneous xenolith-bearing flows are distributed over a linear distance, as in for example the Basin and Range Province (Wilshire et al. 1988), it may be possible to begin to constrain the length of scale of such chemical heterogeneity.

3.2 Application to Spinel Lherzolites

The only useful trace-element data that I have found for testing this model are for spinel lherzolite nodules from three localities: the Dreiser Weiher, Germany; San Luis Potosi, Mexico; and Western Victoria, Australia. Although data were also published for spinel, I have omitted these data due to both the extreme low modal abundance and the generally low REE concentrations of this phase.

It is important to point out that the pyroxene geothermometry (e.g. Sachtleben & Seck 1981) not necessarily give actual melting temperatures but temperatures for the last re-equilibration. Subsolidus phenomena (e.g. intergrown regions, exsolution lamellae) can affect the distribution of elements, so that concentrations may not reflect concentrations during the melting event. However, effects on the distribution behavior for post-melting re-equilibration are yet not well constrained.

3.2.1 Spinel Lherzolites from Dreiser Weiher, Germany

The Dreiser Weiher in the Westeifel, Germany, is a late Quaternary maar-type volcano and is well known for the great variety of ultramafic nodules occurring within the surrounding scoria fans. Its volcanic activity was related to recent uplift of the Rhenish Shield (Frechen, 1963).

Spinel lherzolites from this location are representative members of the anhydrous lherzolite to harzburgite suite and are typical of spinel lherzolites world-wide (e.g. Irving 1980). They show a variable abundance of clinopyroxene which is widely recognized as reflecting their refractory character (Frey & Green 1974). Their equilibration temperatures fall into a narrow and distinct range of about 1140-1165°C (Sachtleben & Seck 1980), and Sm-Nd isotopes give evidence that these lherzolites have not been affected by partial melting events or metasomatic enrichment processes since roughly 0.5×10^9 years (Stosch & Seck 1980). All samples used for this study exhibit a protogranular texture (Mercier & Nicolas 1974), show no exsolution lamellae, and contain no amphibole or patches of

secondary melt. In Table 3.1 REE data for separate, acid-leached mineral phases have been tabulated from Stosch & Seck (1980) and Stosch (1982). REE data were determined by radiochemical neutron activation analyses as described by Stosch & Seck (1980). The precision (1σ-errors) of the analyses as indicated by the error bars shows a dependence on the REE abundance: ± 5% for La, Ce, Sm, Eu, Yb, and Lu; ± 5-10% for Nd, Ho, and Tm; ± 10-15% for Dy.

3.2.2 Spinel Lherzolites from Xalapasco de La Joya, Mexico

The Xalapasco de La Joya maar is believed to be of Quaternary age and belongs to the Ventura group of maars. The Ventura group of maars lies to the north of the active chain of andesitic volcanoes that make up the Trans-Mexican Volcanic Belt (Liang & Elthon 1990).

The overall characteristics of these spinel lherzolites are very similar to those from Dreiser Weiher. The samples are characterized by protogranular textures and show a wide range of modal compositions. Variation diagrams for bulk rock major and minor oxides as a function of bulk rock MgO show an expected correlation with the best fit line from the average spinel lherzolite suggested by Maaloe & Aoki (1977). The geothermometer of Sachtleben & Seck (1981) gives a temperature range of 860-1060°C. Although olivine and orthopyroxene are compositionally homogeneous, some clinopyroxenes display thin reaction coronas (Liang & Elthon 1990). Instrumental neutron activation analysis for all three mineral phases gave concentrations with an estimated precision of 2-5% for Eu and La, and 5-10% for Lu and Yb, and < 2% for Cr (Liang & Elthon 1990). Data are tabulated in Table 3.1 and 3.2.

3.2.3 Spinel Lherzolites from Western Victoria, Australia

Minerals from composite as well as modal-metasomatised spinel lherzolites from western Victoria, Australia, were analyzed for trace elements by O'Reilly et al. (1991). Composite xenoliths show geochemical gradients from vein contacts on a cm scale, while metasomatised samples exhibit volatile-bearing mineral phases such as apatite, amphibole, mica and carbonate. However, only Ni was analyzed for all phases (see Table 3.2). The "dry" samples are homogeneous in mineral composition and have a microstructure ranging from equigranular to mylonitic, suggesting that processes such as deformation, recrystallization and reequilibration have occurred. These samples are included in this chapter in order to explore if this model is also applicable to secondarily-enriched samples.

3.3 Results

REE, Cr and Ni concentrations of olivine, orthopyroxene and clinopyroxene (Table 3.1) for samples described above were applied to the one-element/two-phase model and are shown in Figures 3.4-3.19.

The first striking result is that samples from Xalapasco de La Joya show - in contrast to the Dreiser Weiher samples - no evidence suggesting a homogeneous starting composition, and all data points for La, Eu and Lu in Figures 3.15, 3.16 and 3.17 seem to be distributed randomly as illustrated in Figure 3.2. Inadequate sample preparation has to be rejected as a possible cause for this result, because the preparation procedure described by Liang & Elthon (1990) is identical to that of Stosch (1982). However, possible controlling factor for the scatter of data could be the broad range of re-equilibration temperatures (200°C difference between the lowest and highest values). Additionally, reaction coronas of the clinopyroxenes indicate disequilibrium. Therefore, it is difficult to judge if the original source rock composition was uniform.

Diagrams for REE in the Dreiser Weiher samples, however, indicate some degree of systematic behavior as a function of REE atomic number (see Figures 3.4-3.14). For the first four diagrams (La→Sm) data show no order, except for Sm and Nd in orthopyroxene and clinopyroxene. With increasing atomic number, however, data points seem to describe a trend with a remarkably good fit (e.g. Tb and Ho). Interestingly, in some graphs an outlier deviates from the general ratio (e.g. Dy in olivine). In most of the cases this outlier is the particular nodule Ib/3. According to Stosch (1982) no modal metasomatism is recognized in the Ib/3 nodule. Nevertheless, this inclusion might reflect some "cryptic" metasomatism, because it shows a high LREE abundance for its low clinopyroxene modal abundance (Stosch 1982). For some graphs, the REE abundance of Ib/3 is so high, that it compresses all other data points drastically (e.g. Ce).

Apart from this particular nodule, MREE and HREE are compatible with a relatively uniform composition in the lithospheric mantle underneath the Dreiser Weiher for this spinel lherzolite suite. The small scatter in several graphs near the origin may be related to analytical uncertainties. Although the actual starting abundance of the source rock is not directly determinable, it must lie at some point along the upward extension line of the trend, assuming applicability of the model in 3.1.

In principle, the same theory applies also to compatible trace elements such as Cr and Ni which are shown in Figure 3.18 and 3.19, respectively.

Cr data from the Xalapasco de la Joya locality (Liang & Elthon, 1990) show a reasonably coherent trend while their REE, as discussed above, do not. Several possibilities might be responsible for this observation: First, the reaction coronas of the clinopyroxene phase cause disequilibria for REE concentrations but not for the Cr. Second, a selective cryptic metasomatic event spared Cr concentrations. Third, the starting composition was not uniform for REEs but perhaps was for Cr.

Ni concentrations from Western Victoria, Australia, of both the anhydrous and hydrous group give no evidence to postulate a collective source rock composition. This is

not surprising insofar as secondary enrichment processes obviously have modified the mineral compositions as indicated by hydrous mineral phases and veins.

The good fit of the data for MREE and HREE in samples from the Dreiser Weiher is consistent with the potential of this kind of diagram in providing a potential test of mantle heterogeneity for a given element. It would now be instructive to use this approach for multiple spinel lherzolite suites that have been brought up over an extended geographical area. Unfortunately, insufficient data are available in the literature.

3.4 Summary

This chapter derives algebraically a "one-element/two-phase" model based on the mathematics given by Johnson et al. (1990), and applies it to trace element concentration in spinel lherzolites from following localities: Dreiser Weiher, Germany; San Luis, Potosi; Mexico and Western Victoria, Australia. An application of this model ought to constrain the degree of heterogeneity in the source rock composition for a given element.

REE concentrations of spinel lherzolite from Dreiser Weiher indicate a uniform starting composition in the source rock with a function of atomic order. Thus , MREE and HREE are distributed systematically, while LREE are not. No correlations between La, Eu, Lu and Ni exist for spinel lherzolites from Western Victoria and San Luis Potosi with the exception of Cr from the latter locality. The trace element distribution of these samples might reflect heterogeneous starting compositions within the lithospheric mantle but can be also influenced by secondary enrichment. This is especially likely for the Western Victoria samples, because here spinel lherzolites exhibit veins and hydrous mineral phases.

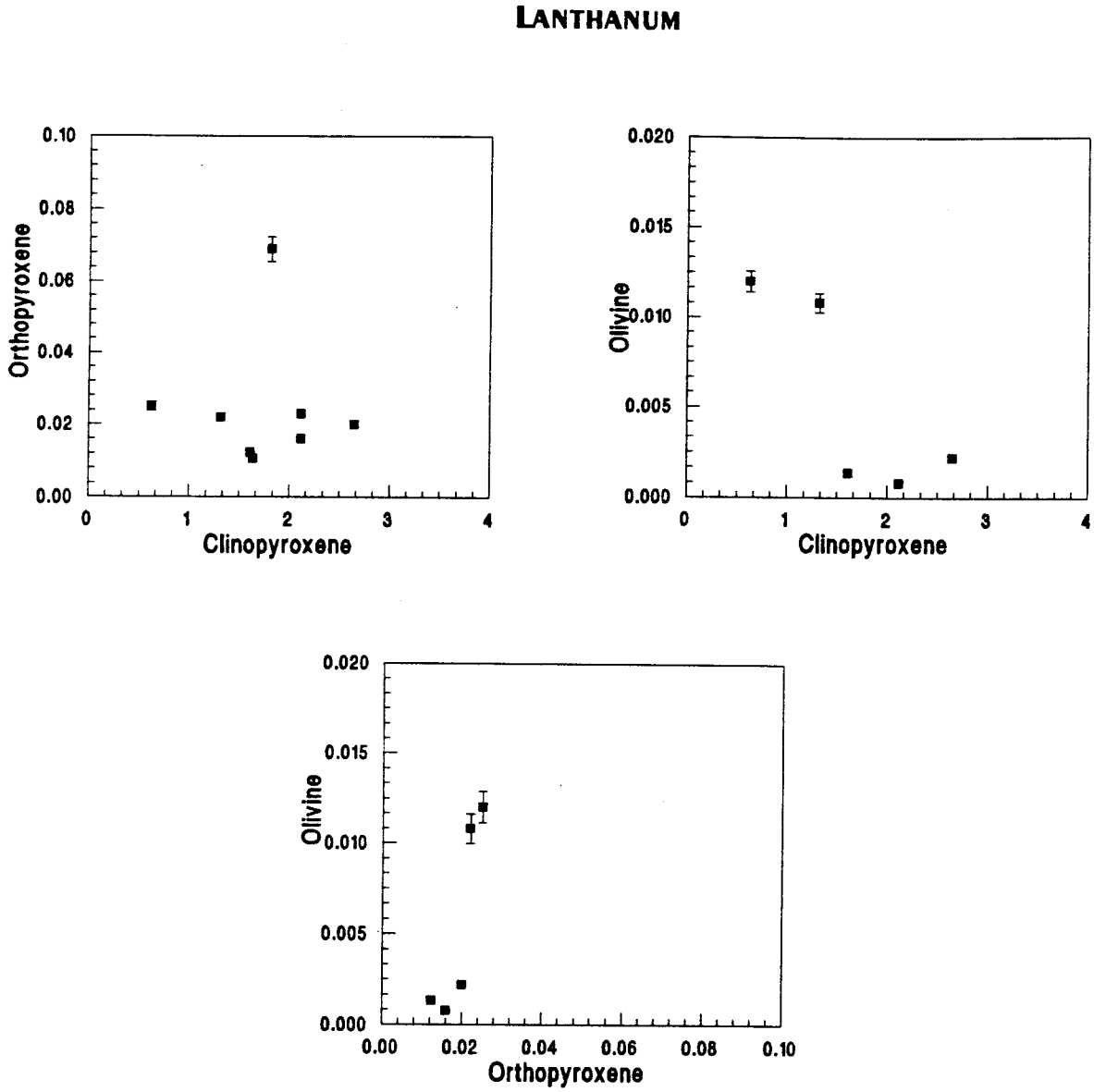

Figure 3.4: **One-element/two-phase diagrams of Lanthanum. Spinel lherzolite nodules are from Dreiser Weiher, Germany. Concentrations are in ppm and are from Stosch & Seck (1980) and Stosch (1982).**

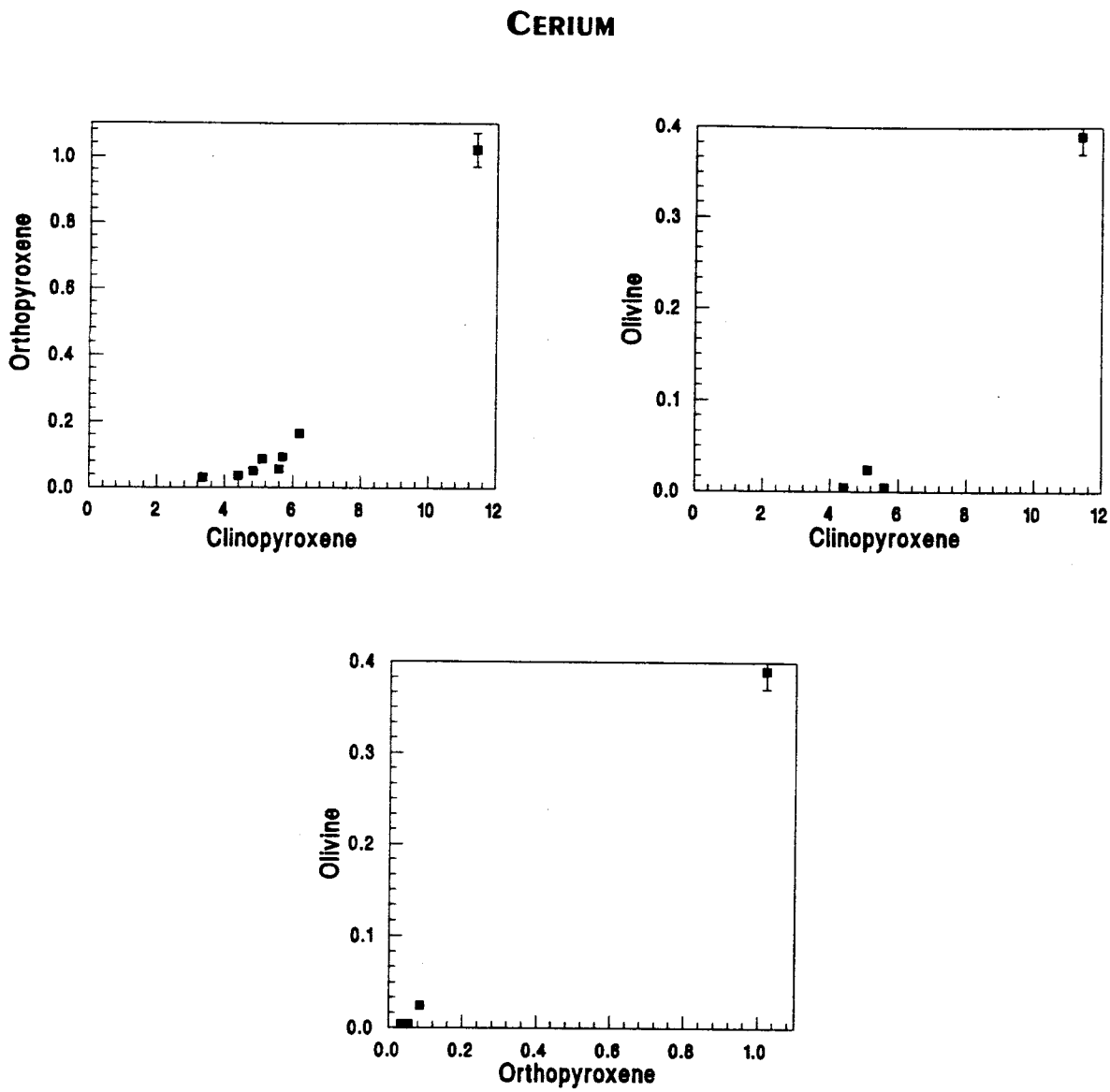

Figure 3.5: **One-element/two-phase diagrams of Cerium. Spinel lherzolite nodules are from Dreiser Weiher, Germany. Concentrations are in ppm and are from Stosch & Seck (1980) and Stosch (1982).**

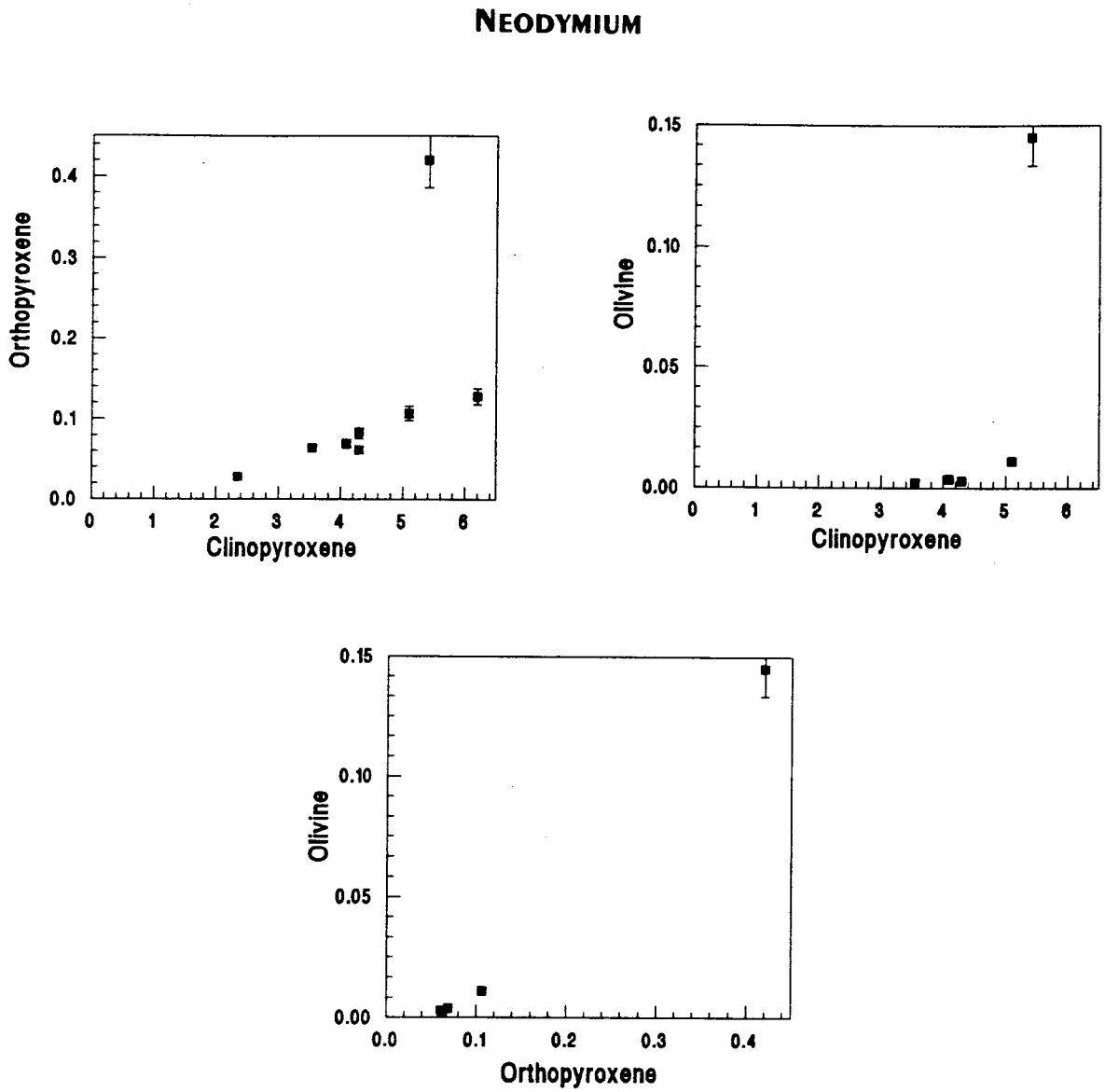

Figure 3.6: **One-element/two-phase diagrams of Neodymium. Spinel lherzolite nodules are from Dreiser Weiher, Germany. Concentrations are in ppm and are from Stosch & Seck (1980) and Stosch (1982).**

SAMARIUM

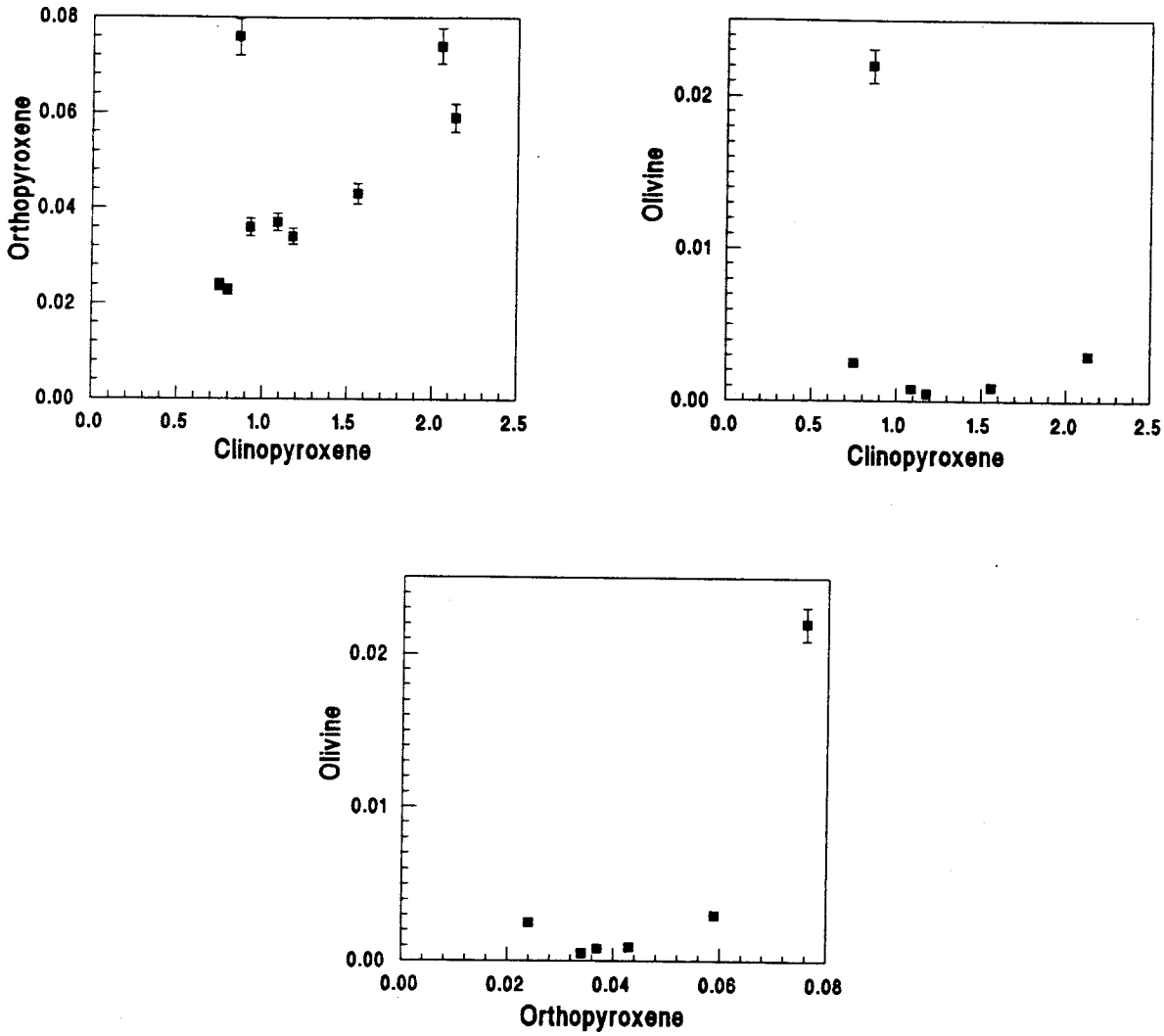

Figure 3.7: **One-element/two-phase diagrams of Samarium. Spinel lherzolite nodules are from Dreiser Weiher, Germany. Concentrations are in ppm and are from Stosch & Seck (1980) and Stosch (1982).**

EUROPIUM

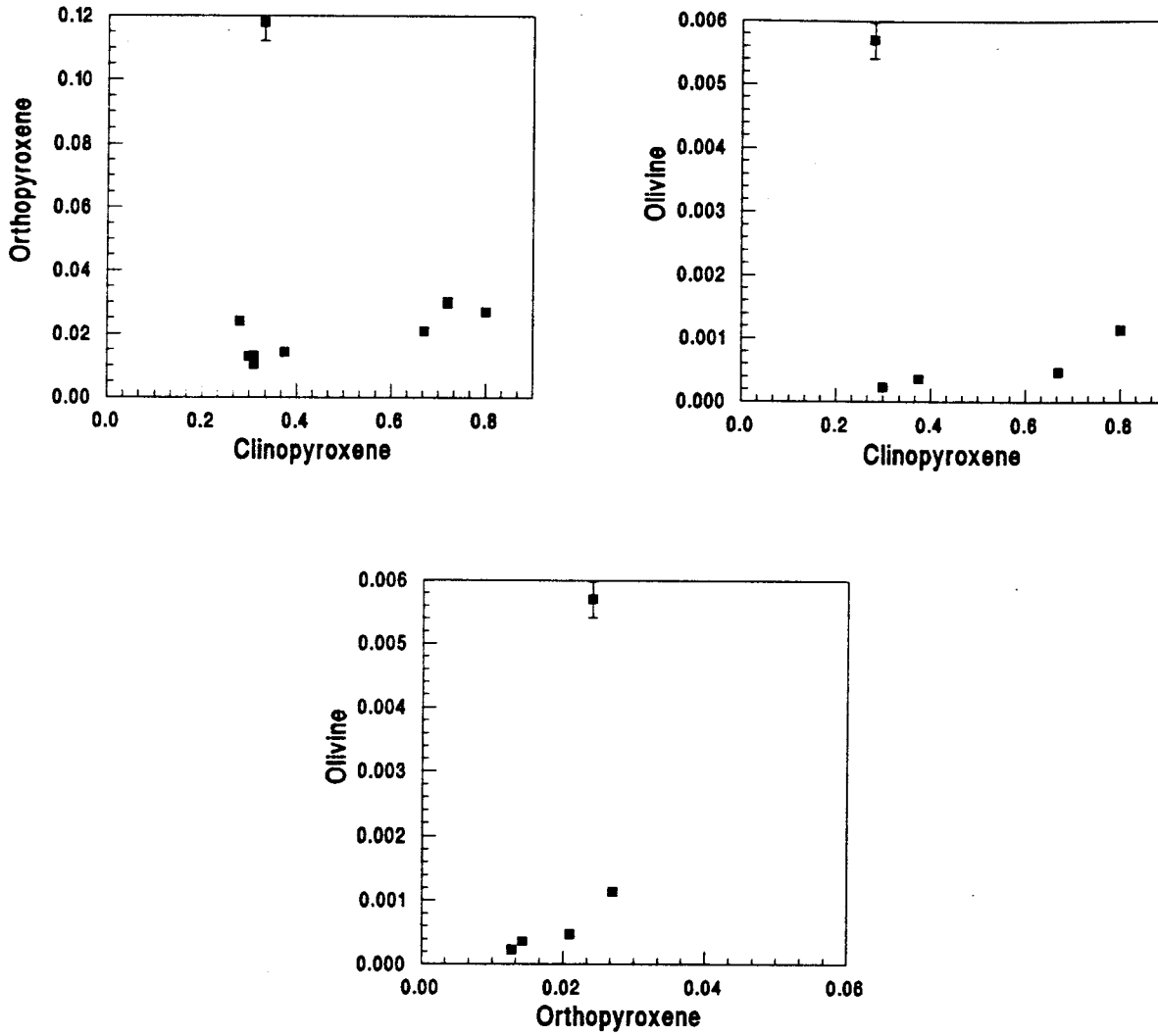

Figure 3.8: **One-element/two-phase diagrams of Europium. Spinel lherzolite nodules are from Dreiser Weiher, Germany. Concentrations are in ppm and are from Stosch & Seck (1980) and Stosch (1982).**

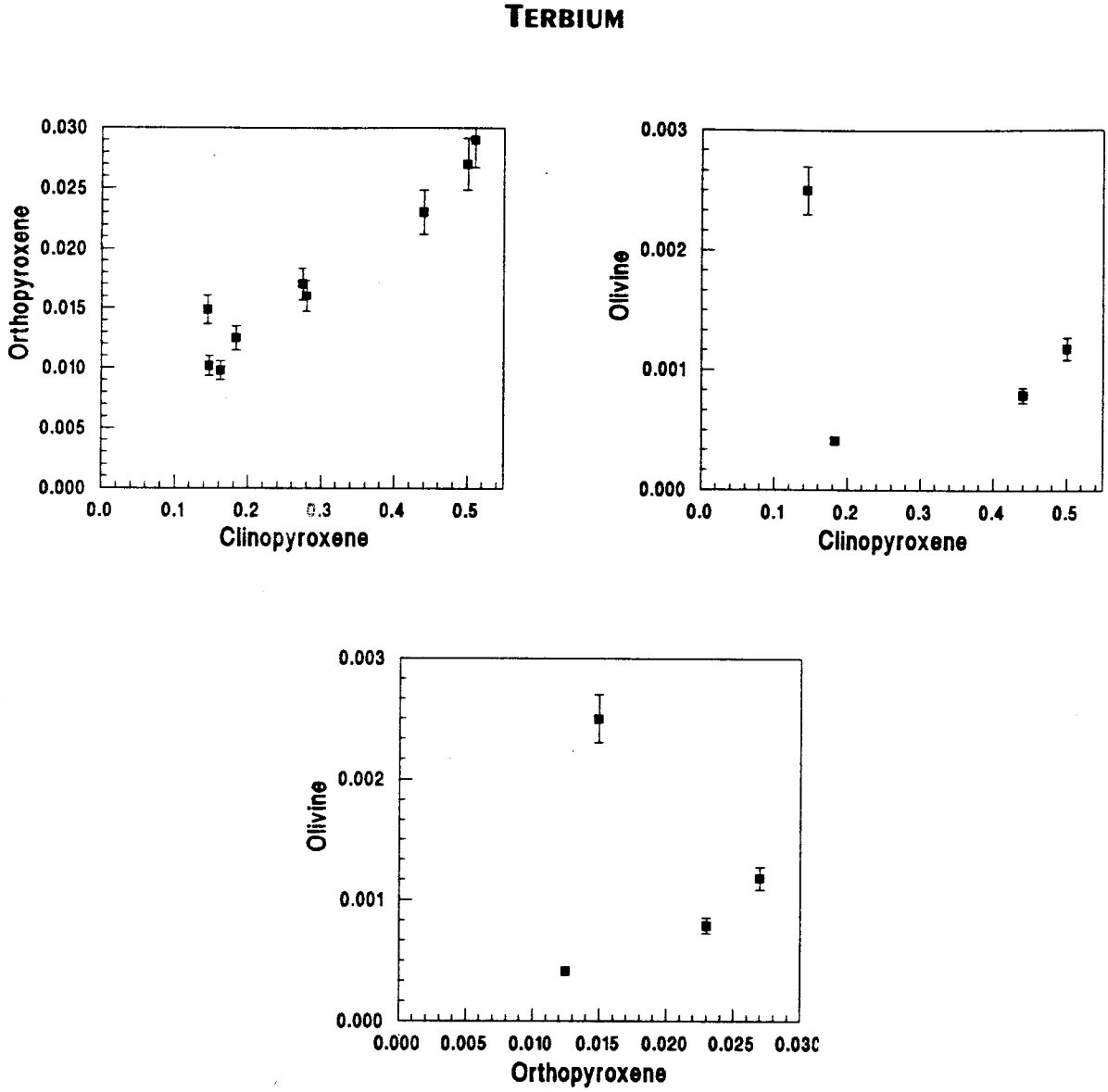

Figure 3.9: **One-element/two-phase diagrams of Terbium. Spinel lherzolite nodules are from Dreiser Weiher, Germany. Concentrations are in ppm and are from Stosch & Seck (1980) and Stosch (1982).**

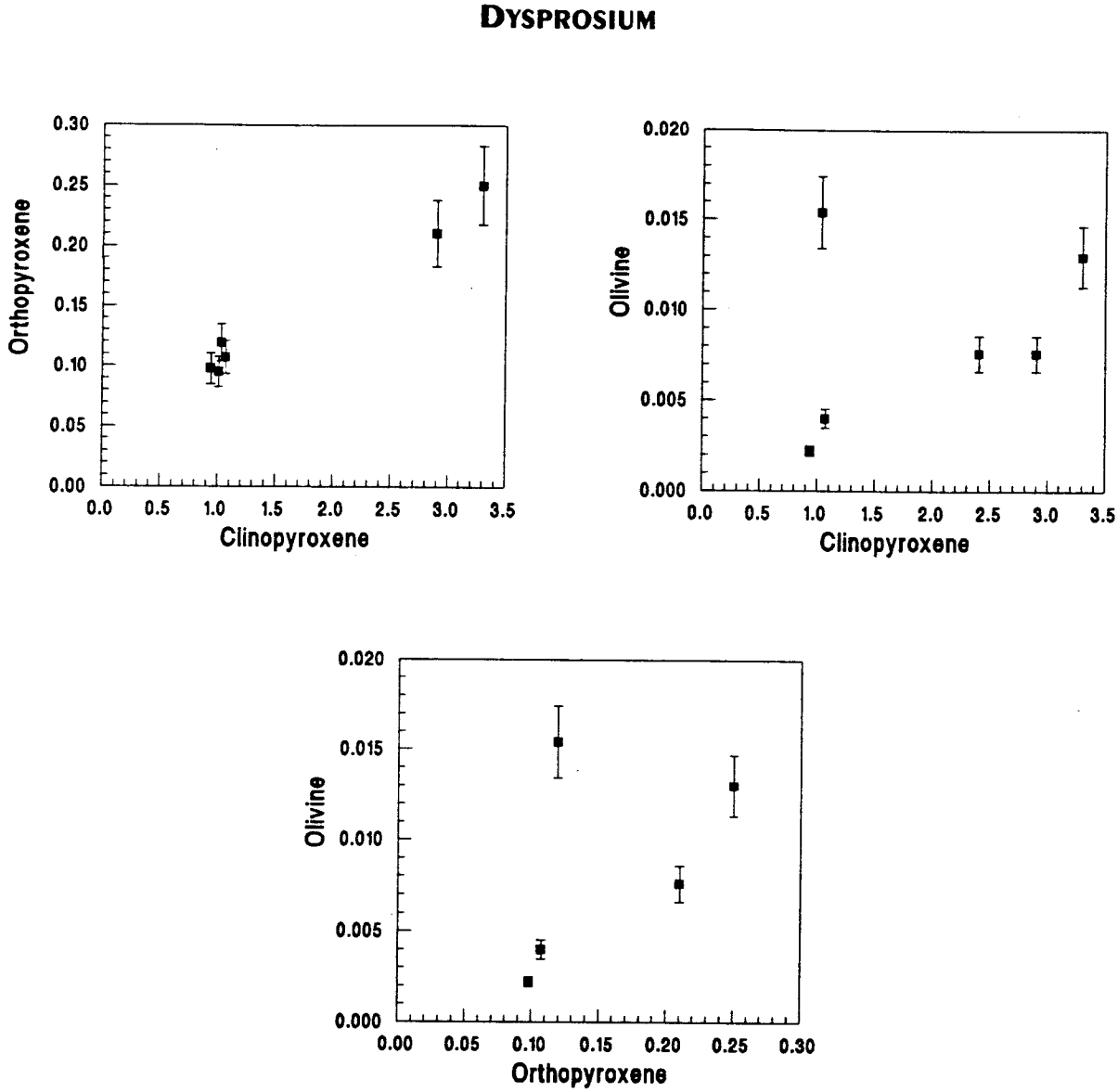

Figure 3.10: **One-element/two-phase diagrams of Dysprosium. Spinel lherzolite nodules are from Dreiser Weiher, Germany. Concentrations are in ppm and are from Stosch & Seck (1980) and Stosch (1982).**

HOLMIUM

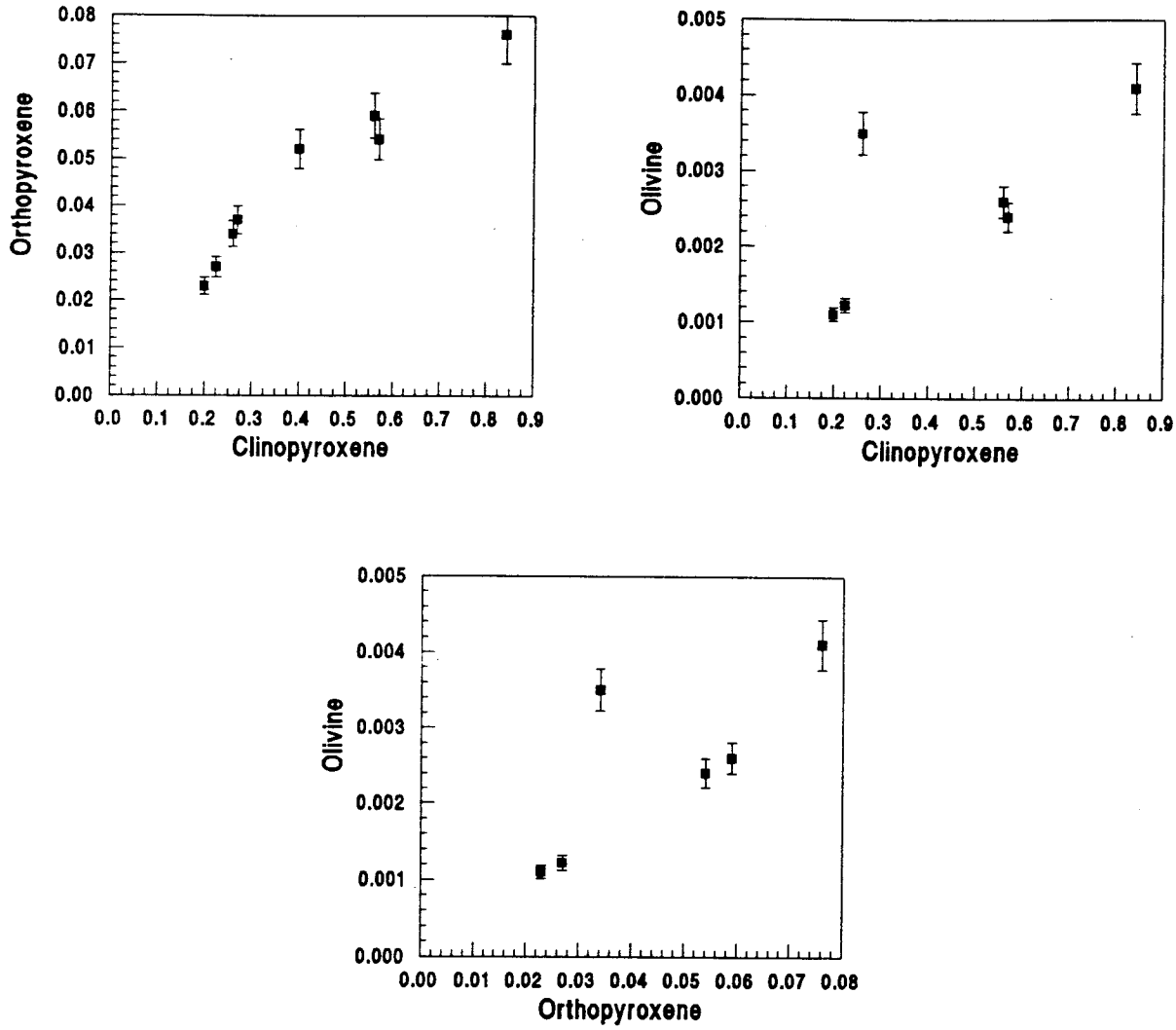

Figure 3.11: **One-element/two-phase diagrams of Holmium. Spinel lherzolite nodules are from Dreiser Weiher, Germany. Concentrations are in ppm and are from Stosch & Seck (1980) and Stosch (1982).**

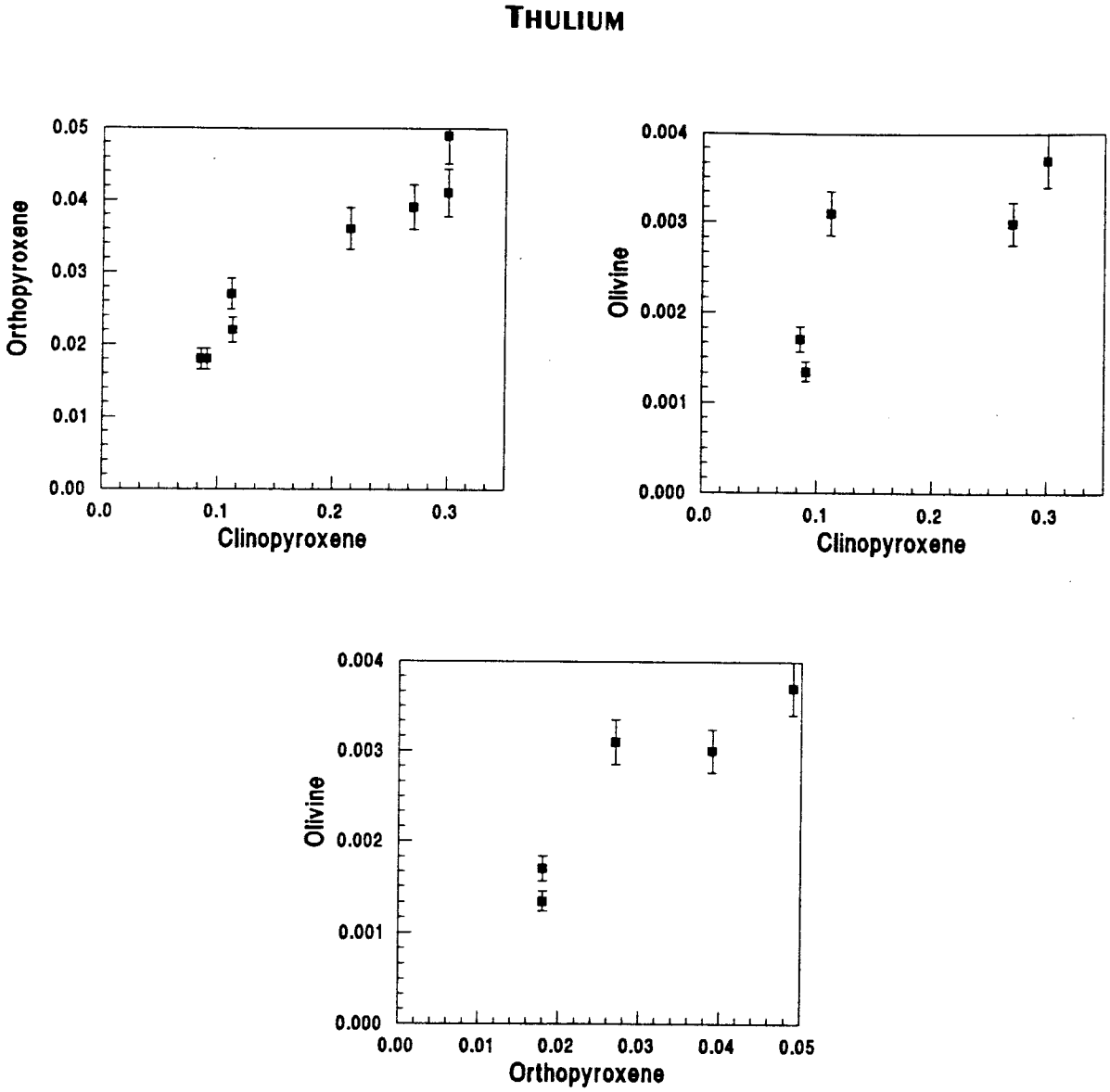

Figure 3.12: **One-element/two-phase diagrams of Thulium. Spinel lherzolite nodules are from Dreiser Weiher, Germany. Concentrations are in ppm and are from Stosch & Seck (1980) and Stosch (1982).**

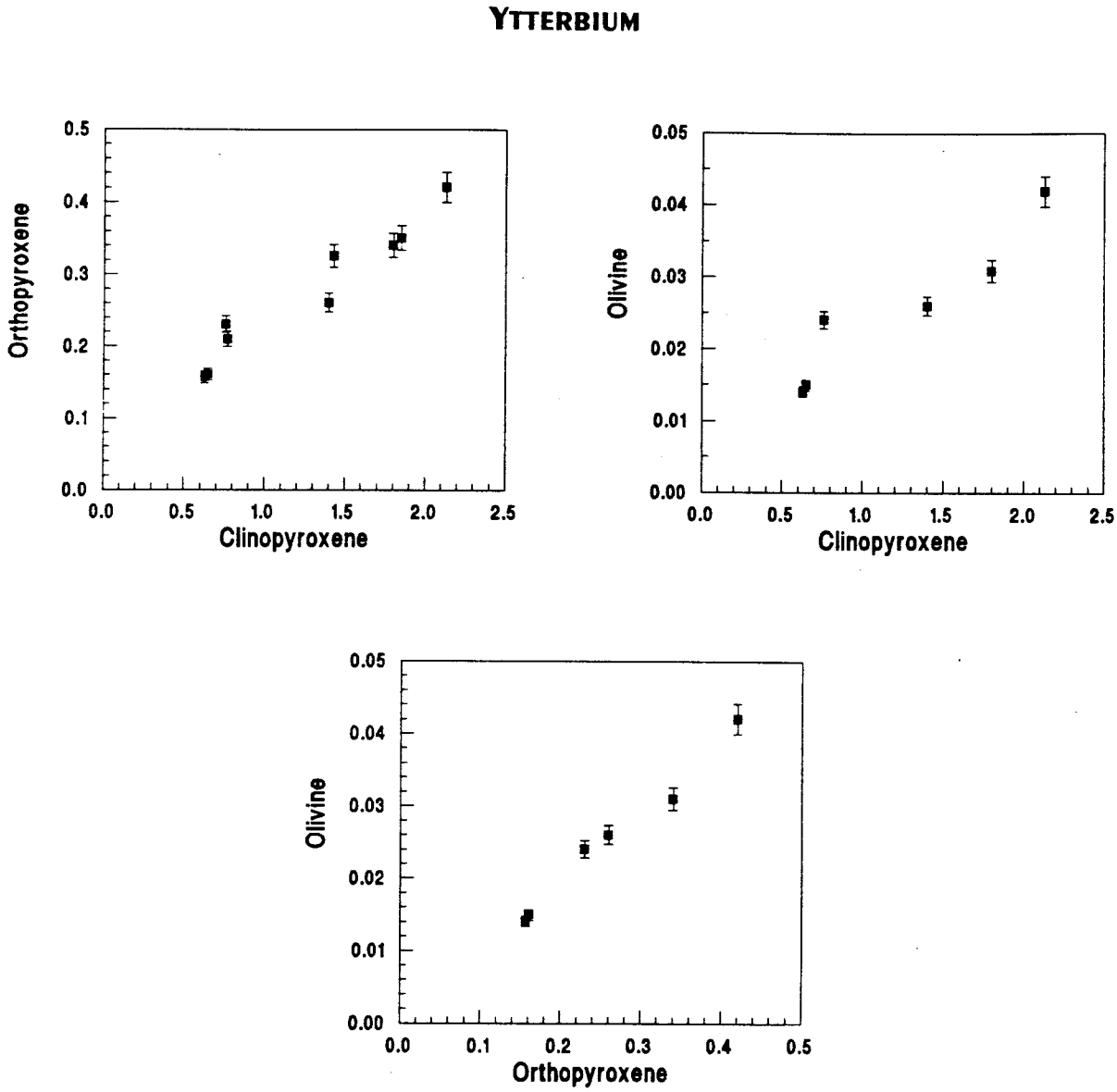

Figure 3.13: **One-element/two-phase diagrams of Ytterbium. Spinel lherzolite nodules are from Dreiser Weiher, Germany. Concentrations are in ppm and are from Stosch & Seck (1980) and Stosch (1982).**

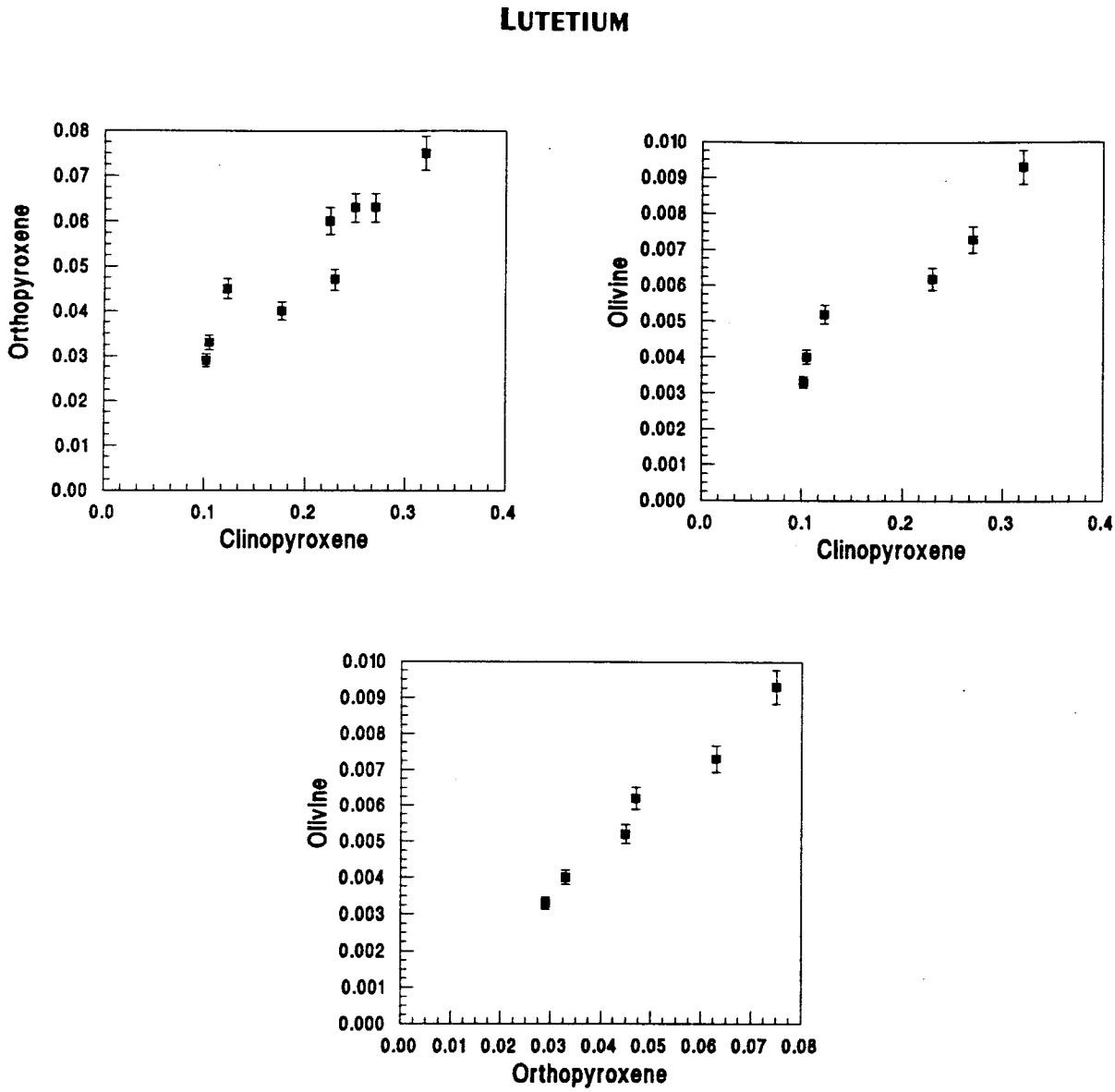

Figure 3.14: **One-element/two-phase diagrams of Lutetium. Spinel lherzolite nodules are from Dreiser Weiher, Germany. Concentrations are in ppm and are from Stosch & Seck (1980) and Stosch (1982).**

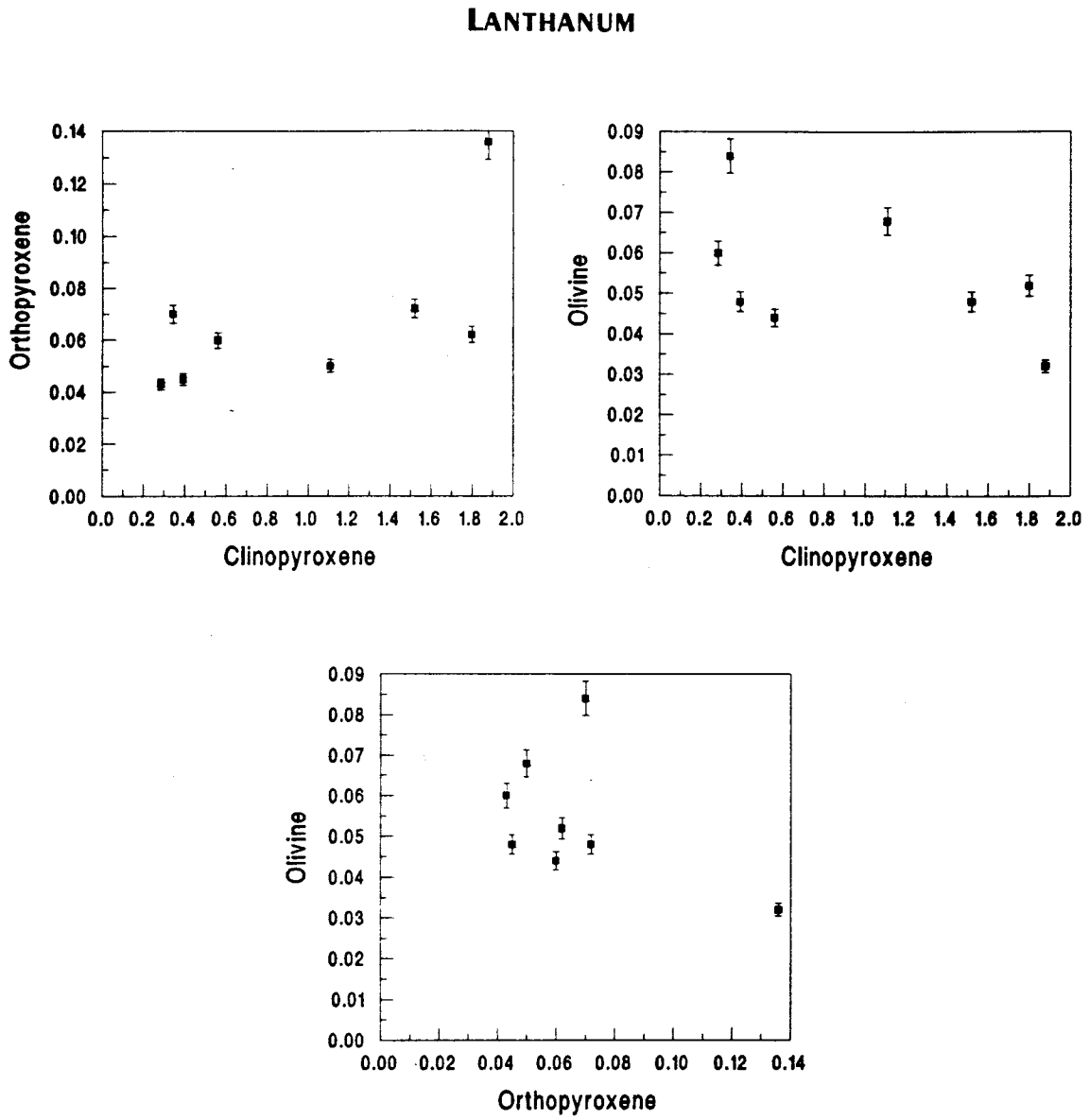

Figure 3.15: **One-element/two-phase diagrams of Lanthanum. Spinel lherzolite nodules are from Xalapasco de La Joya, Mexico. Concentrations are in ppm and are from Liang & Elthon (1990).**

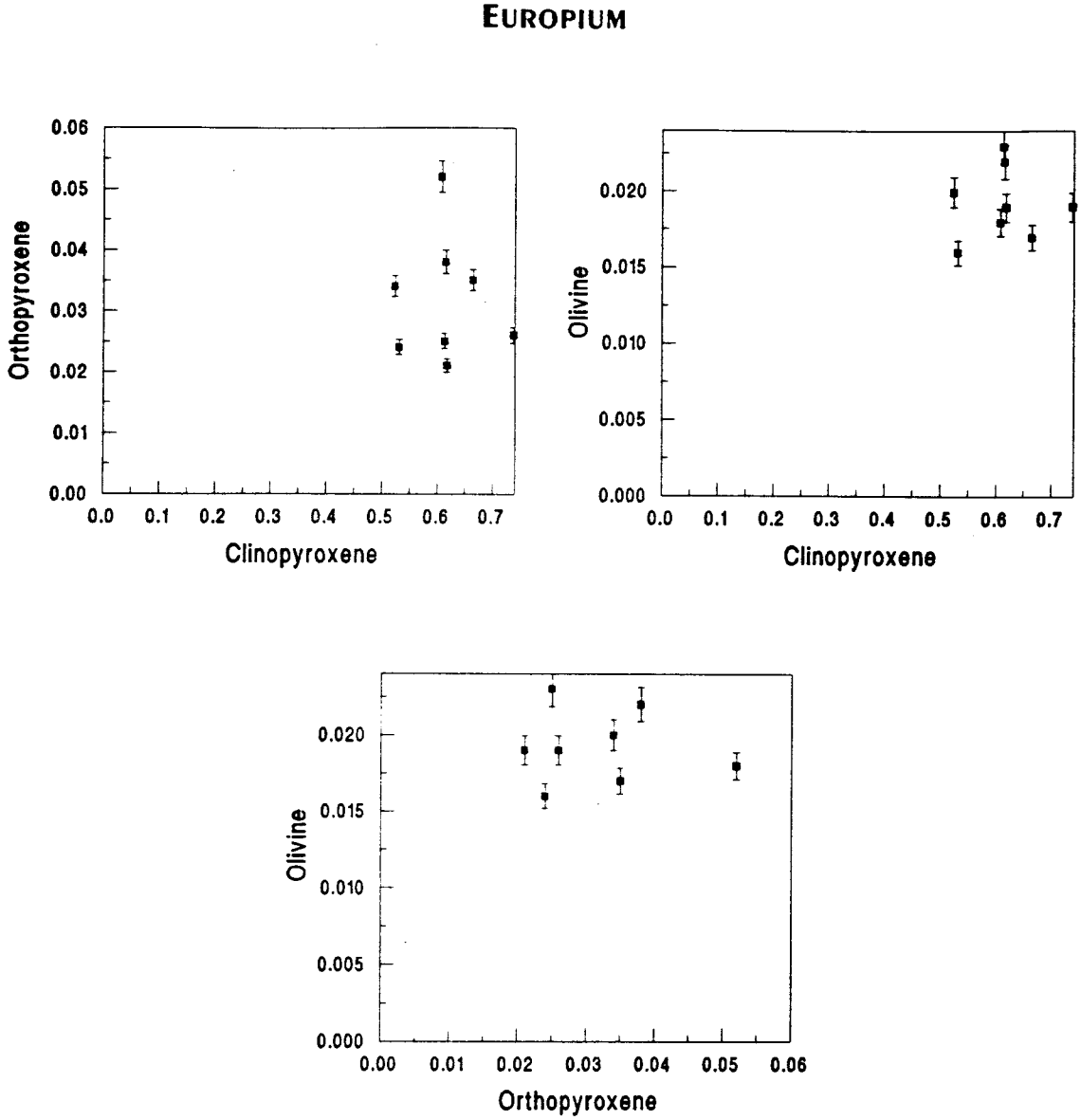

Figure 3.16: **One-element/two-phase diagrams of Eutropium. Spinel lherzolite nodules are from Xalapasco de La Joya, Mexico. Concentrations are in ppm and are from Liang & Elthon (1990).**

LUTETIUM

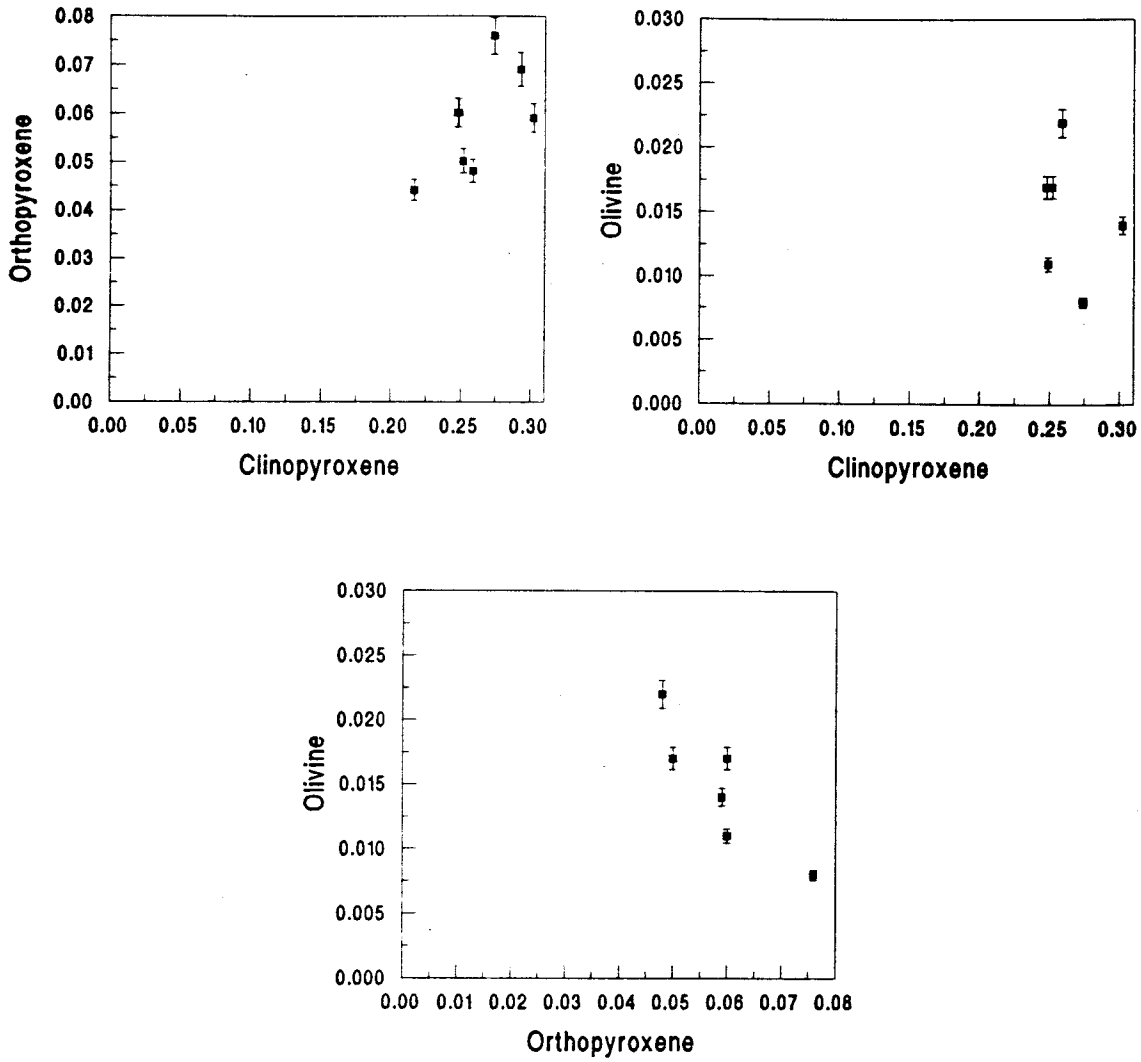

Figure 3.17: **One-element/two-phase diagrams of Lutetium. Spinel lherzolite nodules are from Xalapasco de La Joya, Mexico. Concentrations are in ppm and are from Liang & Elthon (1990).**

CHROMIUM

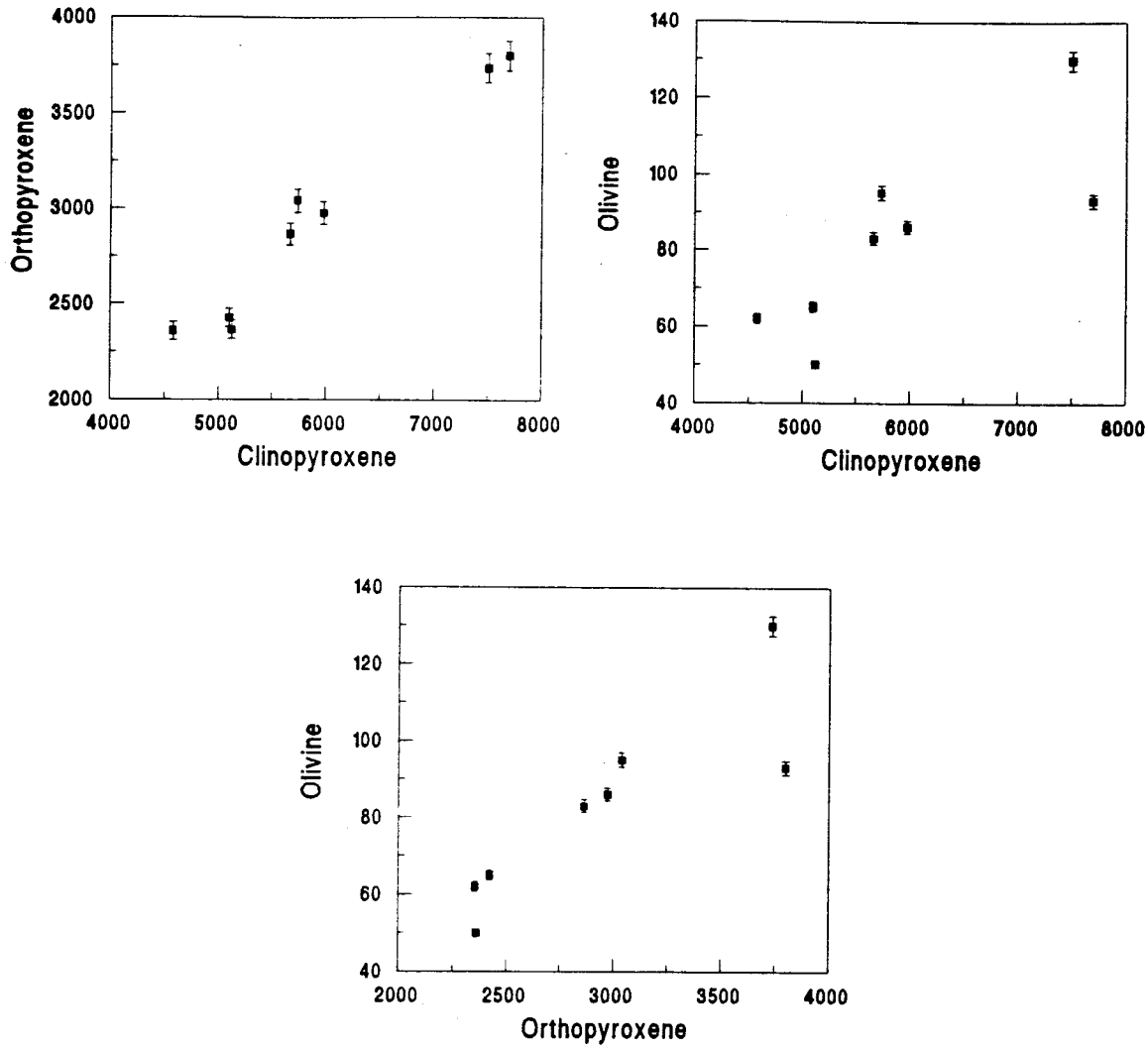

Figure 3.18: **One-element/two-phase diagrams of Chromium. Spinel lherzolite nodules are from Xalapasco de La Joya, Mexico. Concentrations are in ppm and are from Liang & Elthon (1990).**

NICKEL

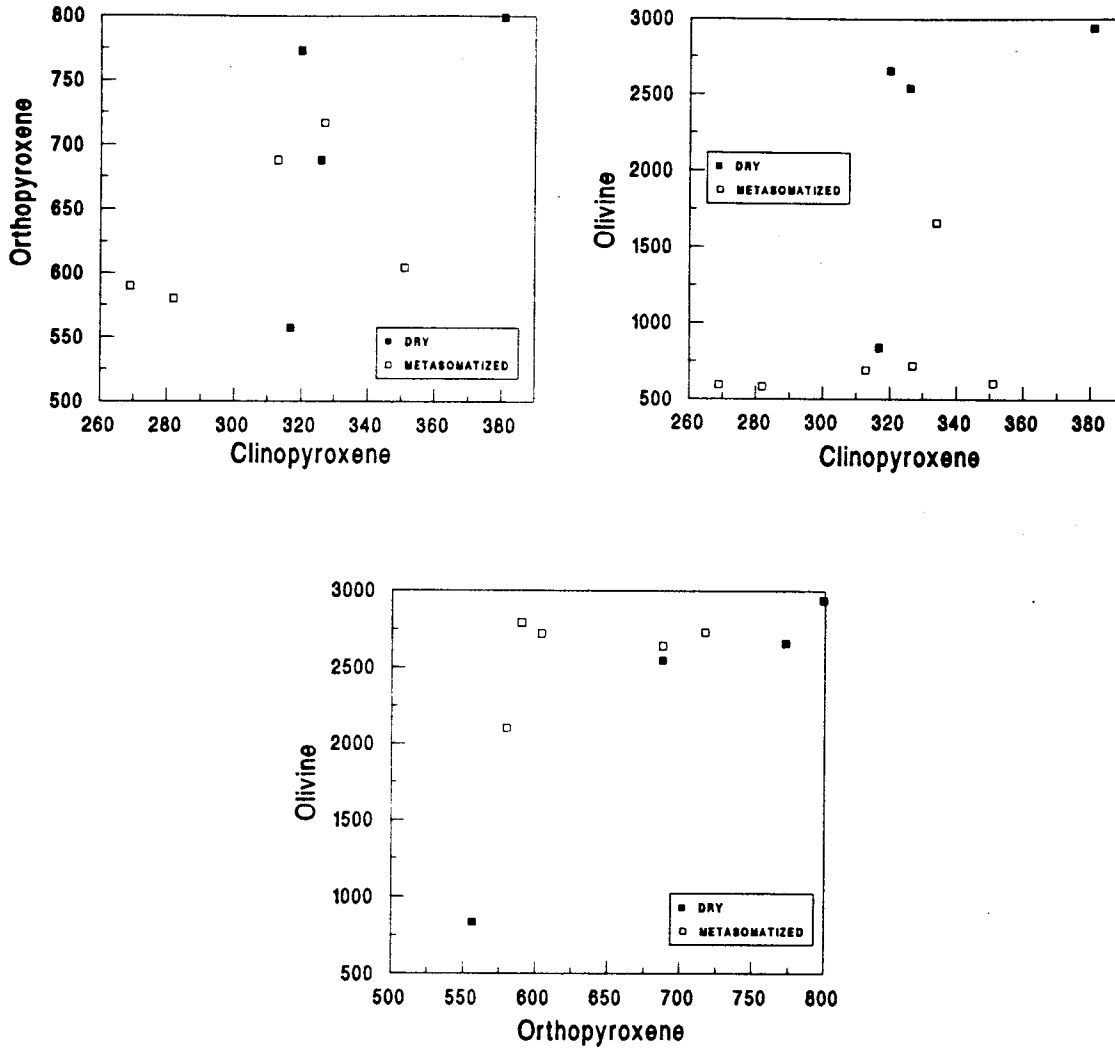

Figure 3.19: **One-element/two-phase diagrams of Nickel. Spinel lherzolite nodules are from Western Victoria, Australia. Concentrations are in ppm and are from O'Reilly et al. (1991).**

Table 3.1: **REE analyses for separate minerals in spinel lherzolite nodules. Data are from Stosch & Seck (1980), Stosch (1982), and Liang & Elthon (1990).**

SAMPLE	LA	CE	ND	SM	EU	TB	DY	HO	TM	YB	LU
CLINOPYROXENE (CONCENTRATIONS IN PPM):											
Ib/3	4.6	11.4	5.4	0.86	0.28	0.145	1.03	0.26	0.112	0.76	0.123
Ib/5	0.63	2.2		0.75	0.31	0.28	2.4	0.57		1.4	0.23
Ib/8	1.81	6.2	6.2	2.05	0.72	0.51			0.3	1.85	0.25
Ib/24	2.12	5.7	4.3	0.93	0.31	0.163	1.01	0.27	0.113	0.77	0.177
Ib/K1	1.32	5.1	5.1	2.13	0.8	0.5	3.3	0.84	0.3	2.13	0.32
D-42	2.12	4.85	3.55	1.18	0.3	0.147	0.94	0.2	0.086	0.65	0.105
D-45	1.64	3.35	2.35	0.8	0.33	0.275		0.4	0.215	1.43	0.225
D-50	2.65	5.6	4.1	1.09	0.375	0.184	1.07	0.225	0.091	0.63	0.102
D-58	1.61	4.4	4.3	1.56	0.67	0.44	2.9	0.56	0.27	1.8	0.27
XDJ-1	1.80	6.10		1.53	0.608	0.459				1.67	0.249
XDJ-2	1.88	5.12		1.67	0.665	0.467				1.74	0.252
XDJ-4	1.11	7.31		1.76	0.738	0.443				1.39	0.217
XDJ-5	1.52	4.76		1.62	0.616	0.448				1.76	0.248
XDJ-7	0.287	3.40		1.50	0.618	0.550				1.87	0.302
XDJ-10	0.344	3.36		1.34	0.524	0.479				1.82	0.293
XDJ-11	0.562	3.08		1.31	0.614	0.407				1.53	0.259
XDJ-13	0.393	3.22		1.27	0.532	0.514				1.80	0.274
ORTHOPYROXENE (CONCENTRATIONS IN PPM):											
Ib/3	0.51	1.02	0.42	0.076	0.024	0.015	0.119	0.034	0.027	0.23	0.045
Ib/5	0.025			0.024	0.010	0.016		0.054		0.26	0.047
Ib/8	0.069	0.163	0.128	0.074	0.03	0.029	0.25	0.067	0.041	0.35	0.063
Ib/24	0.023	0.092	0.082	0.036	0.013	0.0098	0.095	0.037	0.022	0.21	0.04
Ib/K1	0.022	0.086	0.107	0.059	0.027	0.027	0.25	0.076	0.049	0.42	0.075
D-42	0.016	0.049	0.063	0.034	0.0128	0.0102	0.098	0.023	0.018	0.161	0.033
D-45	0.0106	0.03	0.0275	0.023	0.0118	0.017	0.17	0.052	0.036	0.325	0.06
D-50	0.02	0.055	0.069	0.037	0.0143	0.0125	0.107	0.027	0.018	0.157	0.029
D-58	1.34	3.7	2.8	0.94	0.47	0.79	7.6	2.6	3	31	7.3
XDJ-1	0.062			0.046	0.052					0.437	0.060
XDJ-2	0.136			0.040	0.035					0.350	0.050
XDJ-4	0.050			0.029	0.026					0.357	0.044
XDJ-5	0.072			0.054	0.038					0.384	0.060
XDJ-7	0.043			0.027	0.021					0.472	0.059
XDJ-10	0.070			0.043	0.034					0.416	0.069
XDJ-11	0.060			0.033	0.025					0.403	0.048
XDJ-13	0.045				0.024					0.405	0.076

Table 3.1: (continued)

SAMPLE	LA	CE	ND	SM	EU	TB	DY	HO	TM	YB	LU
OLIVINE (CONCENTRATIONS IN PPB):											
Ib/3	230	390	145	22	5.7	2.5	15.4	3.5	3.1	24	5.2
Ib/5	21			2.5			7.6	2.4		26	6.2
Ib/K1	10.8	240	11	3	1.14	1.18	13	4.1	3.7	42	9.3
D-42	0.78		2.1	0.51	0.23		2.2	1.1	1.7	14.9	4.
D-50	2.2	4.3	3.7	0.79	0.36	0.41	4	1.22	1.34	14	3.3
D-58	1.34	3.7	2.8	0.94	0.47	0.79	7.6	2.6	3	31	7.3
XDJ-1	52				18						11
XDJ-2	32				17					58	17
XDJ-4	68				19					59	
XDJ-5	48				22						17
XDJ-7	60				19						14
XDJ-10	84				20					136	
XDJ-11	44				23						22
XDJ-13	48				16						8

Table 3.2: **Ni and Cr analyses for separate minerals in spinel lherzolite nodules. Data are from Liang & Elthon (1990) and O'Reilly et al. (1991). Concentrations in ppm.**

	CLINOPYROXENE:		ORTHOPYROXENE:		OLIVINE:	
SAMPLE	CR	NI	CR	NI	CR	NI
XDJ-1	5735		3039		95	
XDJ-2	5978		2974		86	
XDJ-4	7697		3800		93	
XDJ-5	7501		3735		130	
XDJ-7	4586		2358		62	
XDJ-10	5128		2364		50	
XDJ-11	5665		2864		83	
XDJ-13	5107		2426		65	
9894		320		773		2660
WGBM12		326		688		2548
GN23		317		557		836
LE16B		381		799		2940
WGBM5		327		717		2730
WGBM15		313		688		2640
BM630		334		1660		2950
BM901		282		580		2100
BM650		211				2630
BM655		351		604		2720
BM632		245				2480

4. A COMPARATIVE STUDY FOR MINOR- AND TRACE- ELEMENTS OF CLINOPYROXENES IN ABYSSAL PERIDOTITES AND SPINEL LHERZOLITE NODULES

4.1 Introduction

The fact that oceanic peridotites retain primary diopside (Dick & Fisher 1984) and that their Ti/Zr ratio of Figure 1.2 suggests a rather homogeneous starting composition over a large scale (Johnson et al. 1990). This raises the question of how well similar data of spinel lherzolite nodules correspond to this observation. Such a comparison may be instructive in highlighting similarities and differences in the trace-element character of the oceanic and continental lithospheric mantle. It has been argued that the oceanic lithosphere might be more depleted and homogeneous than the continental lithospheric mantle (e.g. Roden & Murthy 1987; Menzies & Hawkesworth 1987), and that constraints on the continental lithospheric mantle might be more difficult to outline due to its more complex evolution (McDonough 1990).

As in abyssal harzburgites clinopyroxene represents the dominant host for trace elements in a typical spinel lherzolite mineral assemblage (Stosch 1982). Its trace element abundance can thus be used to characterize signatures in the starting composition, because the trace element pattern will be similar for the bulk rock although the bulk rock will show lower concentrations. For this purpose, data from oceanic and continental settings have been collected and will be compared in order to detect if differences exist over an extended geographical scale.

4.2 Choice of Elements

The first step for this comparative study was to determine which trace elements in clinopyroxenes of the abyssal peridotites suite show a reasonable correlation, meaning that they obey a similar compatibility during melting events. In addition, such correlation should exclude elements possibly affected by secondary enrichment or depletion.

Another limiting factor is the availability of literature data on multiple elements in clinopyroxenes from spinel lherzolite nodules. Unfortunately few data, to my knowledge, exist for Zr in such samples. Therefore, an attempt has been made to find a "surrogate" minor element. A good correlation exists for Ti versus Na_2O in abyssal harzburgites. Thus, Na_2O is treated as a moderately incompatible element that concentrates into the melt similar to Ti as melting proceeds, and the observed ratio of Ti/Na_2O should be close to the ratio in the clinopyroxene in the phase source.

Similarly good to reasonably good correlations also exist for Ti versus Nd, Sm, Eu, Dy, Er, and Yb in abyssal harzburgites. Figures 4.1 to 4.9 illustrate Ti correlated to Zr, Na_2O, Ce, Nd, Sm, Eu, Dy, Er, and Yb.

4.3 Results

As a first result, data for the abyssal peridotites are in general more depleted than the spinel lherzolites. Second, graphs for Na_2O, Dy, Er and Yb show extensive overlap of the two fields. While the majority of spinel lherzolite data consistently plot at the upper end of the abyssal peridotite trend, some spinel lherzolite data for Zr, Ce, Nd and Eu with lower Ti abundance shift to higher y-values and fall off the trend. This observation might divide the graphs into two different kinds: one, where data for both sets overlap; and another, where some data points deviates from the general distribution trend. This observation might suggest that elements have originated from the same starting composition, but different melting histories and/or other processes led to a different distribution.

Interestingly, the three spinel lherzolite samples deviating away from the abyssal peridotite field are derived from the Lunar Crater locality (Roden & Shimizu 1993) of the Basin and Range Province. Although these samples are classified as Group I (anhydrous), they show a LREE enrichment indicating a possible "cryptic" metasomatic influence. The Lunar Crater Volcanic field within this Province exposes a highly heterogeneous suite of

spinel peridotites including amphibole-bearing pyroxenites. Although only anhydrous peridotites have been studied there is a good probability that these samples have experienced a "cryptic" metasomatic event. This consideration is supported by the LREE over HREE enrichment (Roden & Shimizu 1993) as shown in Figures 4.3 to 4.9.

Apart from the Lunar Crater samples, a comparison of REEs, Zr and Na_2O versus Ti of clinopyroxenes in abyssal and continental spinel peridotites of world-wide distribution suggests that their original mantle compositions and melting are broadly similar as indicated by the overlapping fields of these two data sets. However, the majority of the continental spinel lherzolites are generally more enriched in trace-and minor-elements, especially Zr, Na_2O, Ce, Nd, Sm, and Eu. This observation might imply that abyssal peridotites have undergone somewhat higher degrees of melting or that their source rock composition was more depleted prior to melting. The ratios evident on the graphs suggest a generally similar starting composition for clinopyroxenes in both oceanic and continental and oceanic upper lithospheric mantle, albeit the continental samples are overall slightly more enriched.

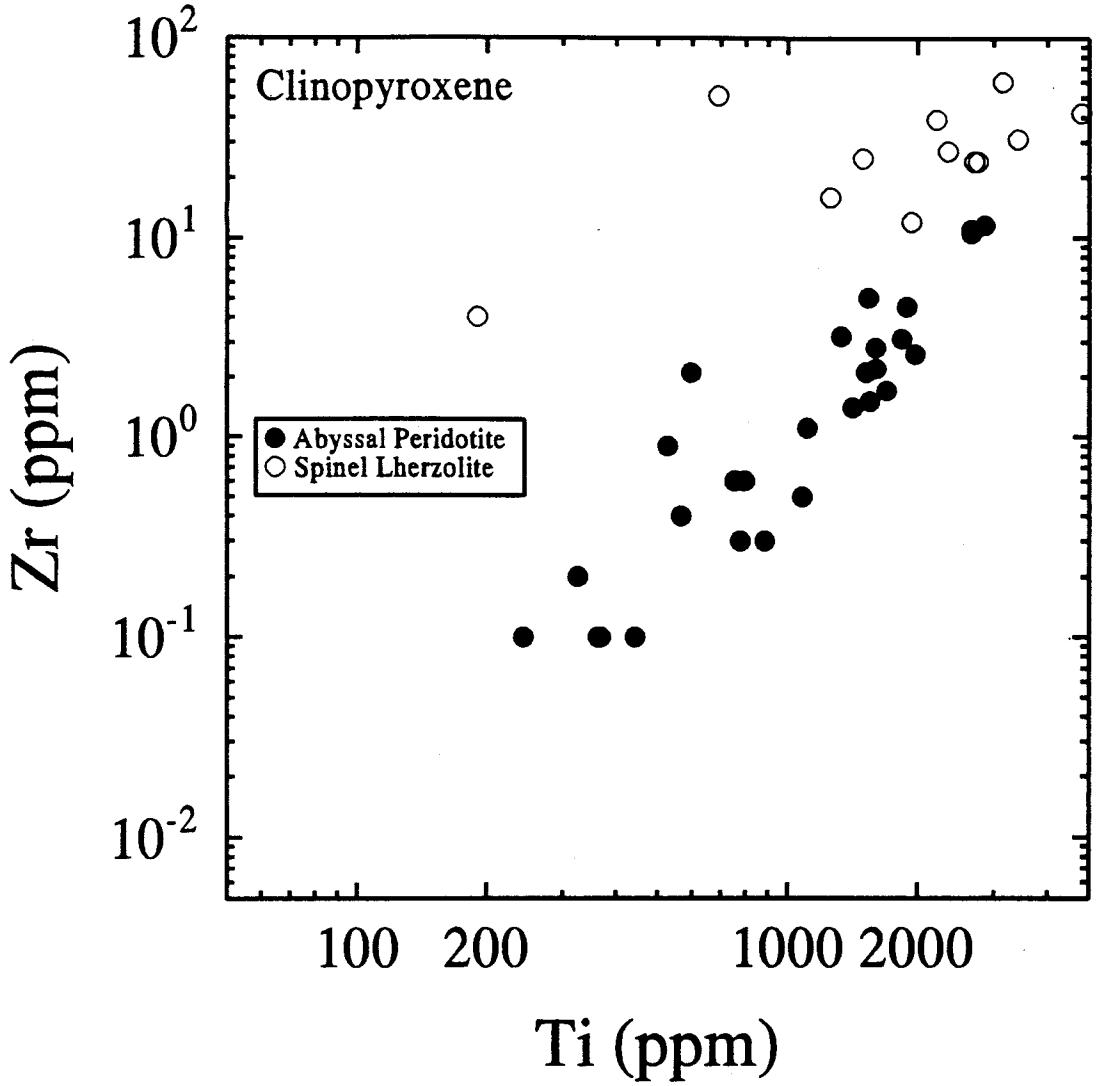

Figure 4.1: **Ti versus Zr in clinopyroxenes of abyssal peridotites and spinel lherzolites. Data are from: Johnson et al. (1990) (solid circles), O'Reilly et al. (1991), and Roden & Shimizu (1993) (open circles).**

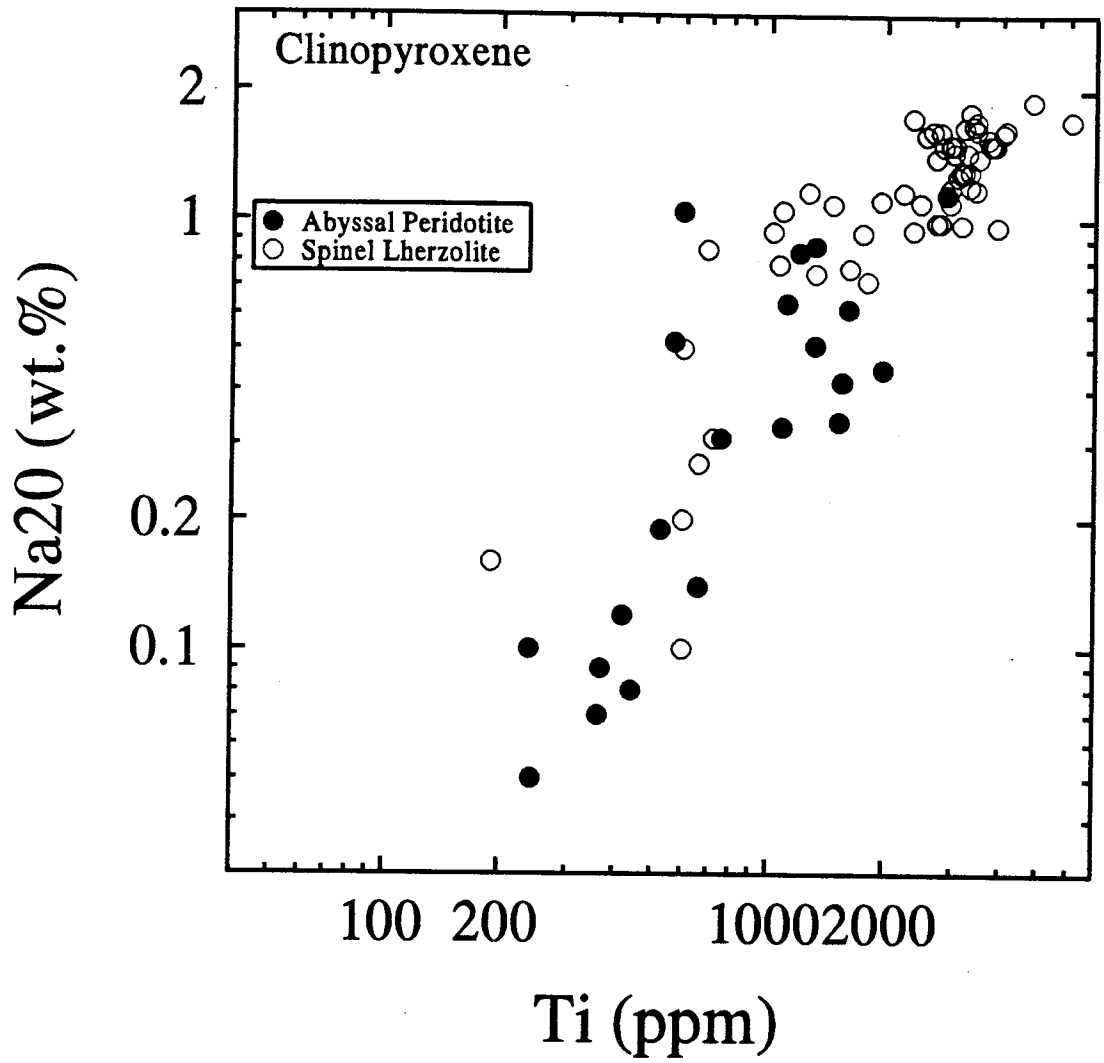

Figure 4.2: **Ti versus Na_2O in clinopyroxenes of abyssal peridotites and spinel lherzolites. Data are from: Johnson et al. (1990) (solid circles), Wilshire et al. (1988), Frey & Prinz (1978), Galer & O'Nions (1988), Best (1974), Baldridge (1979), Stormer (1975), O'Reilly et al. (1991), Frey & Green (1974), Stosch & Seck (1980), Cimmino et al. (1976), Roden & Shimizu (1993) (open circles).**

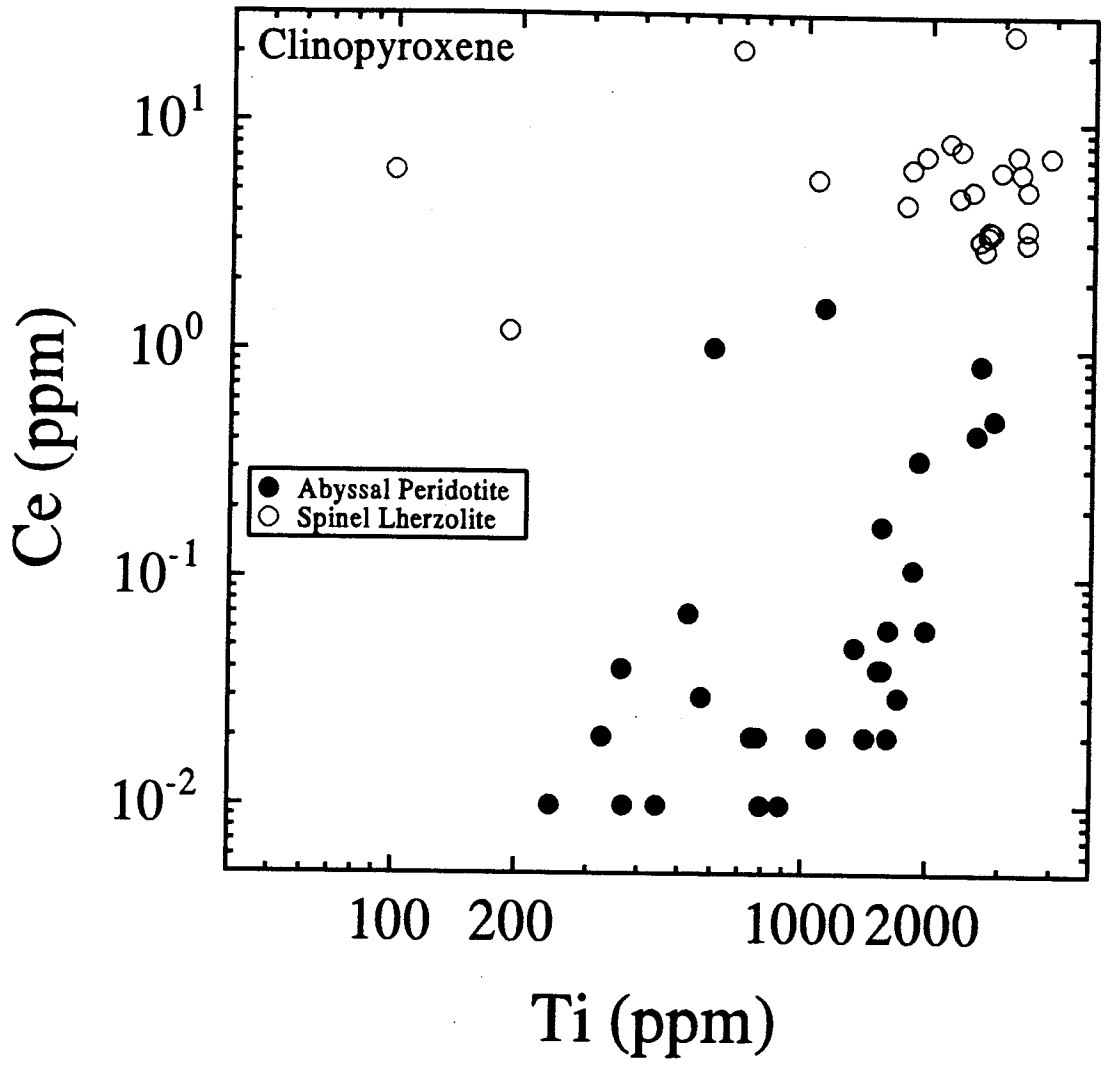

Figure 4.3: **Ti versus Ce in clinopyroxenes of abyssal peridotites and spinel lherzolites. Data are from: Johnson et al. (1990) (solid circles), Liang & Elthon (1990), Stosch (1982) and Roden & Shimizu (1993) (open circles).**

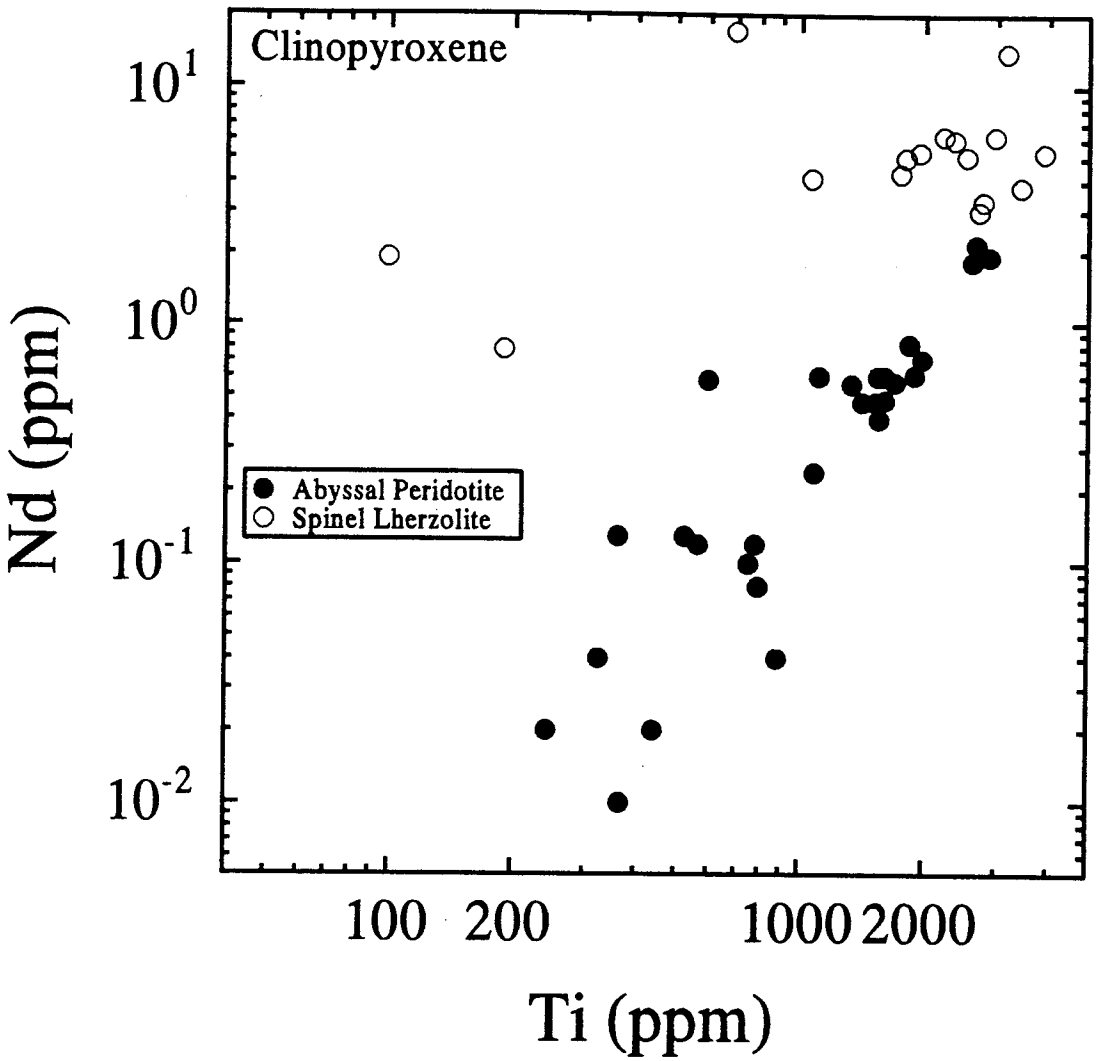

Figure 4.4: **Ti versus Nd in clinopyroxenes of abyssal peridotites and spinel lherzolites. Data are from: Johnson et al. (1990) (solid circles), Stosch (1982) and Roden & Shimizu (1993) (open circles).**

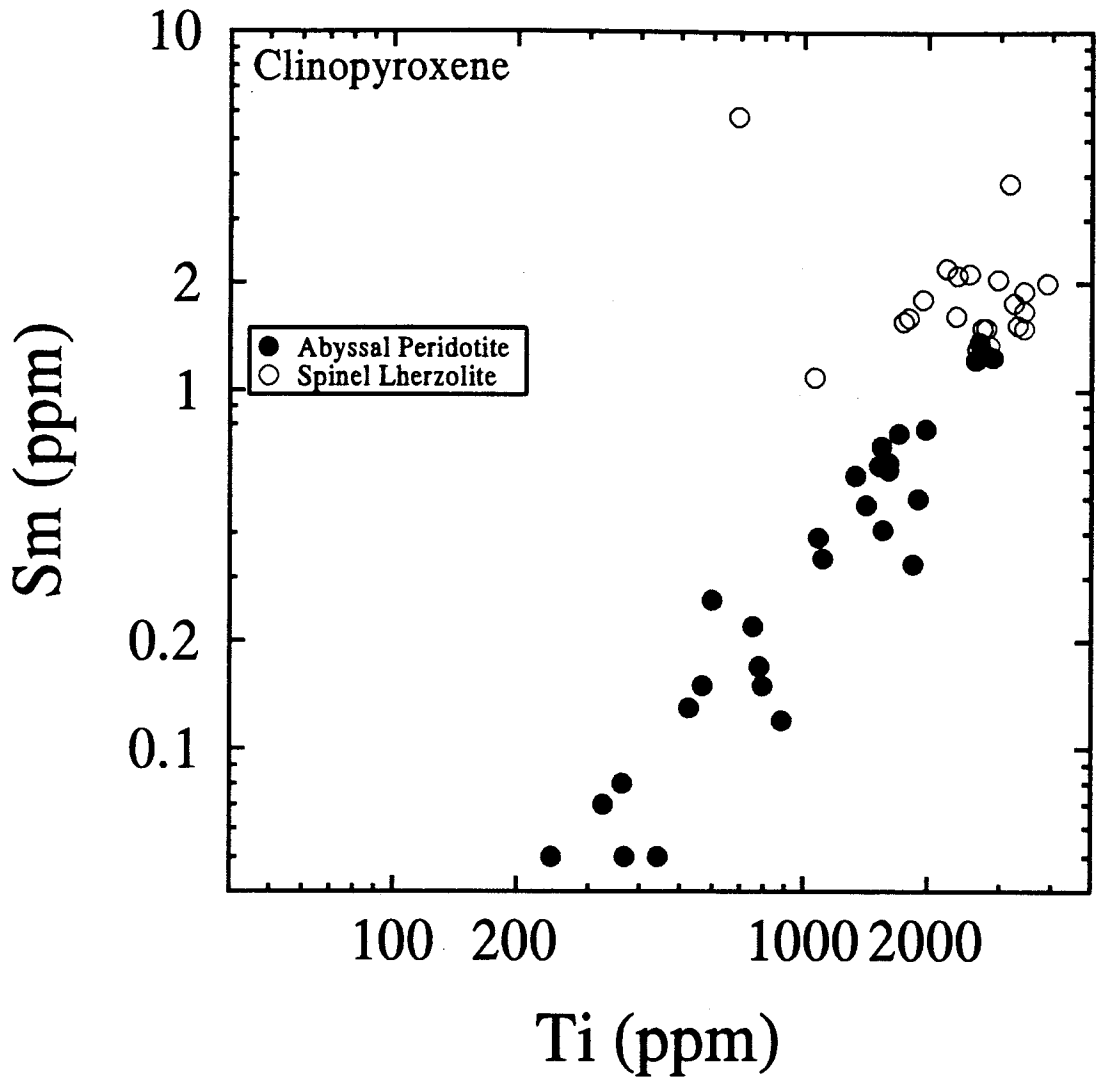

Figure 4.5: **Ti versus Sm in clinopyroxenes of abyssal peridotites and spinel lherzolites. Data are from: Johnson et al. (1990) (solid circles), Liang & Elthon (1990), Stosch (1982) and Roden & Shimizu (1993) (open circles).**

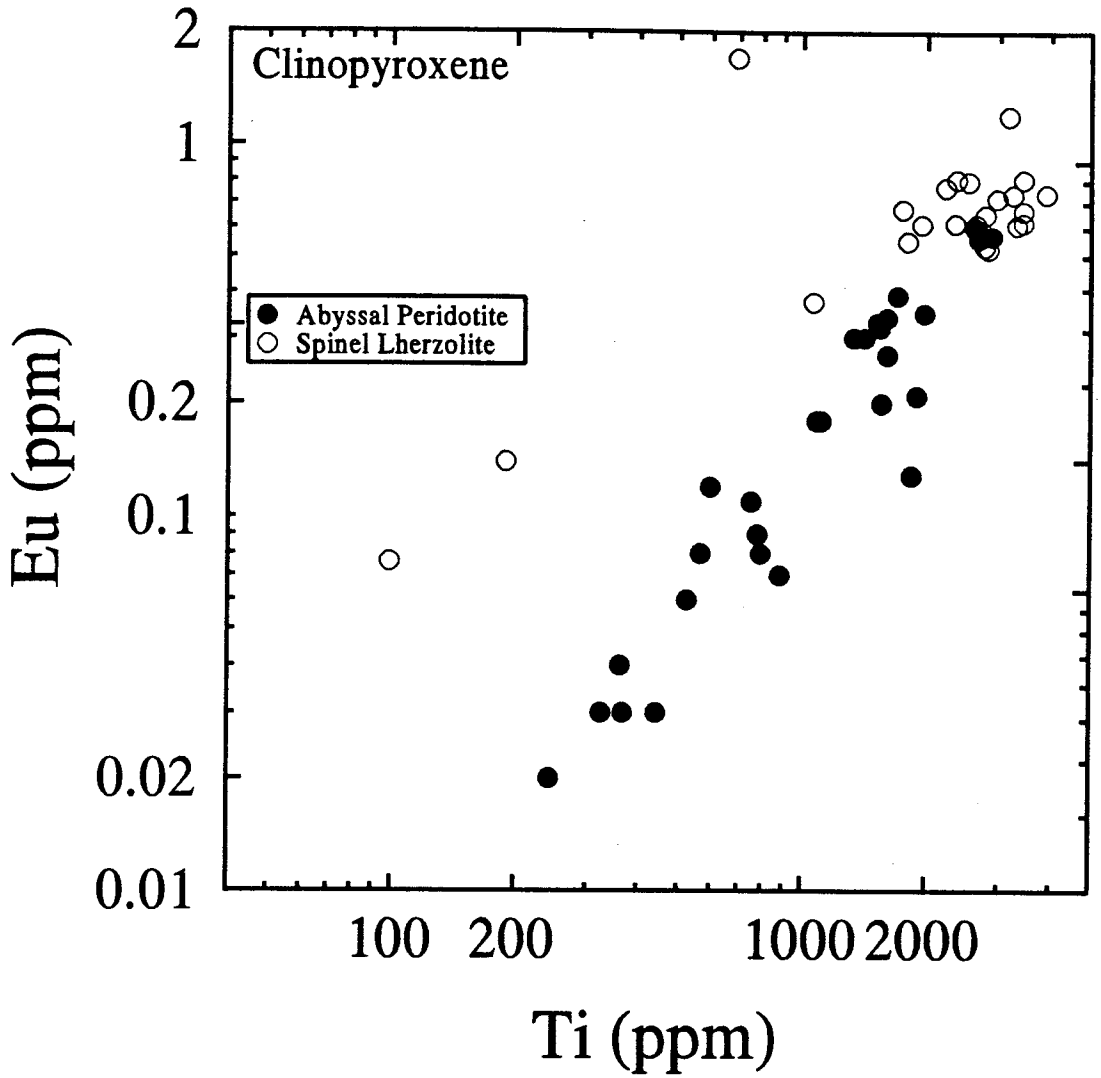

Figure 4.6: **Ti versus Eu in clinopyroxenes of abyssal peridotites and spinel lherzolites. Data are from: Johnson et al. (1990) (solid circles), Liang & Elthon (1990), Stosch (1982) and Roden & Shimizu (1993) (open circles).**

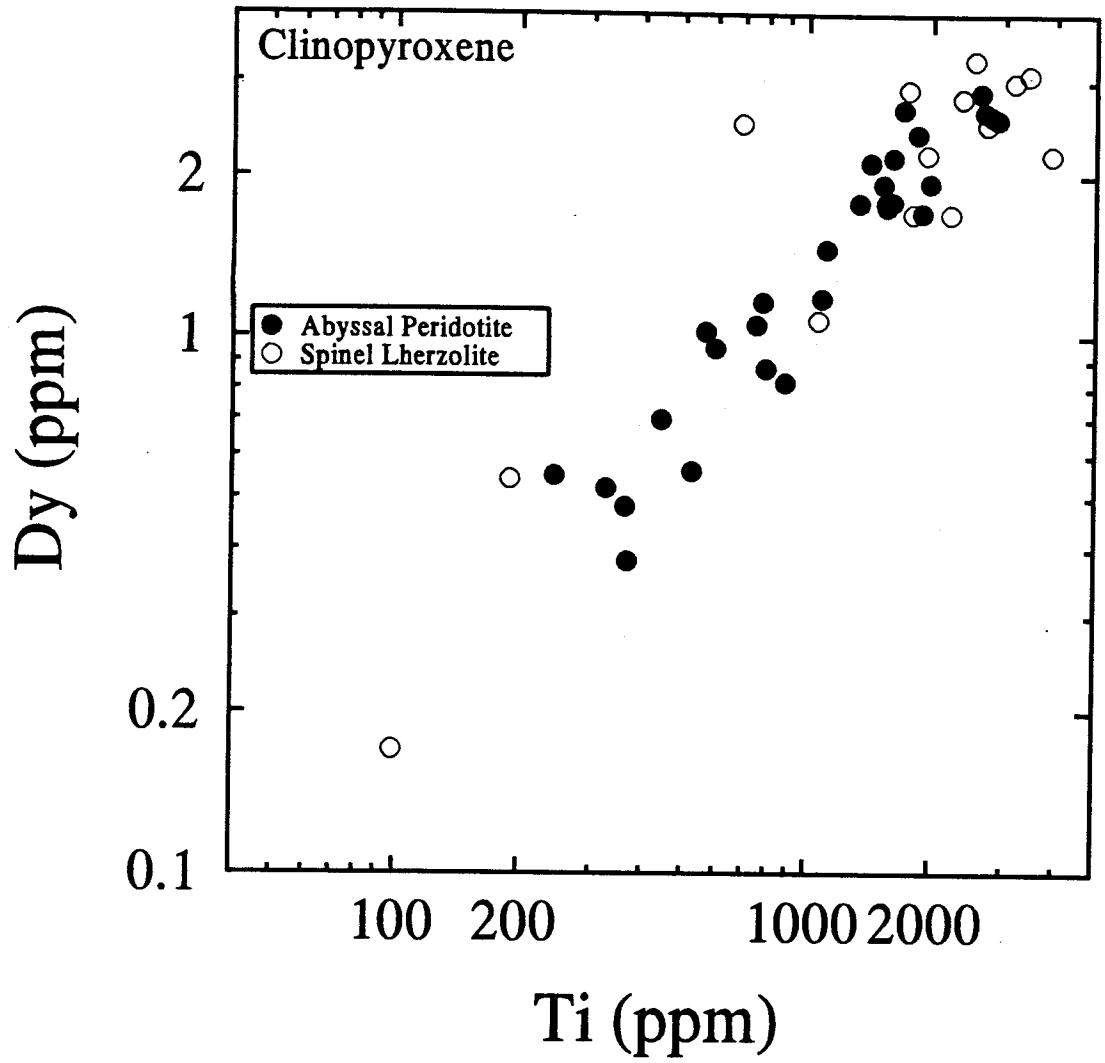

Figure 4.7: **Ti versus Dy in clinopyroxenes of abyssal peridotites and spinel lherzolites. Data are from: Johnson et al. (1990) (solid circles), Stosch (1982) and Roden & Shimizu (1993) (open circles).**

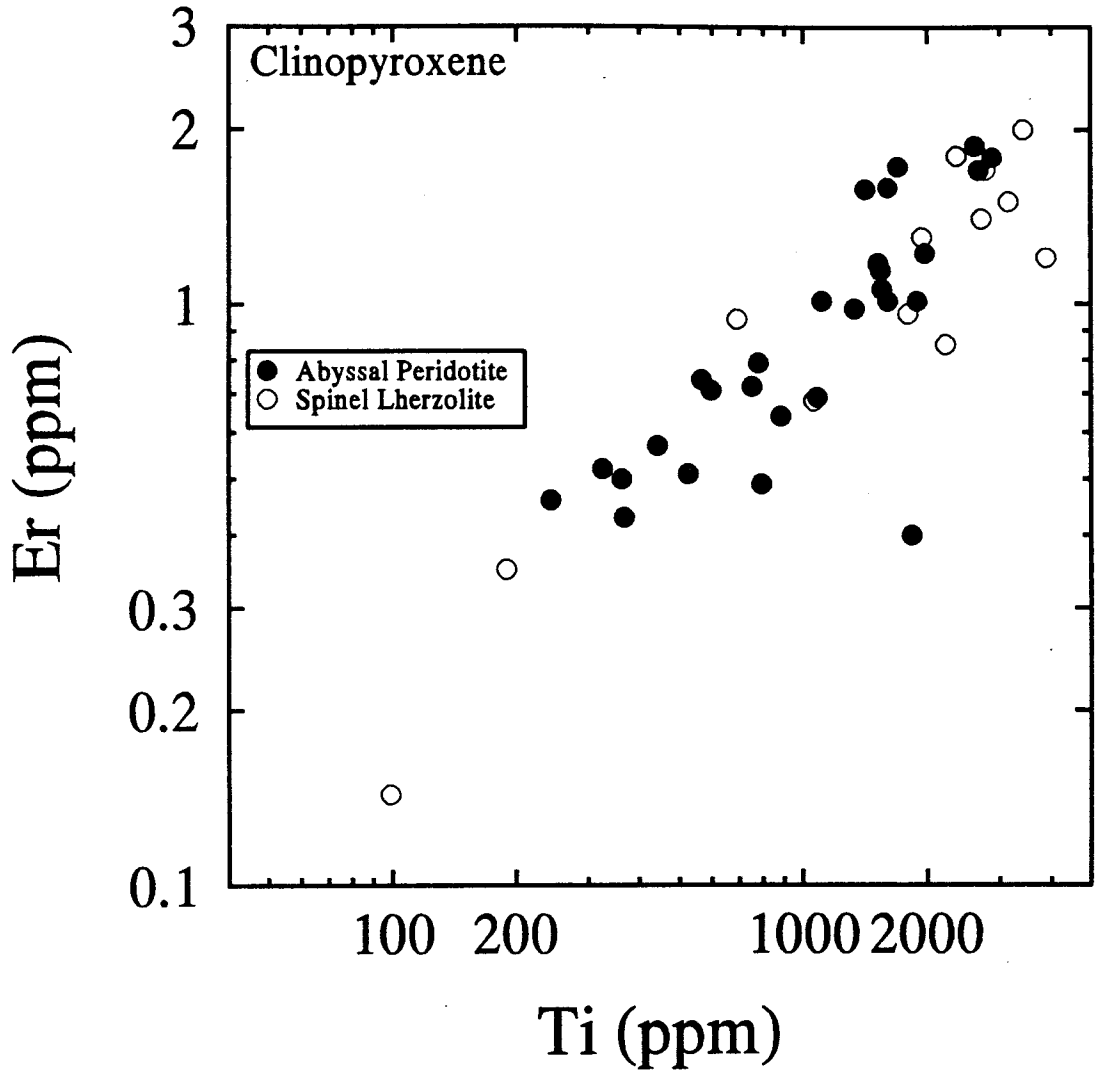

Figure 4.8: **Ti versus Er in clinopyroxenes of abyssal peridotites and spinel lherzolites. Data are from: Johnson et al. (1990) (solid circles), Stosch (1982) and Roden & Shimizu (1993) (open circles).**

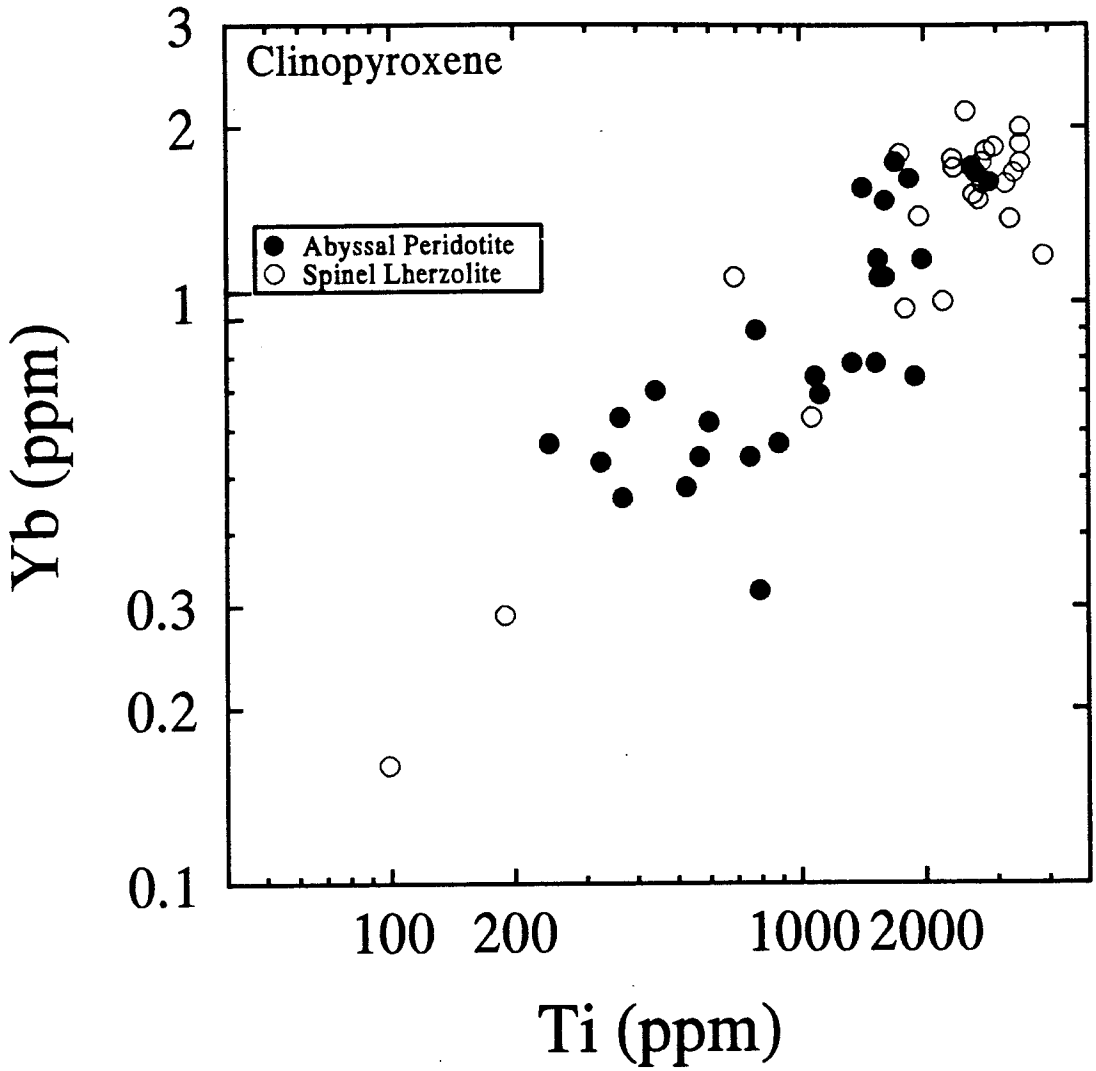

Figure 4.9: **Ti versus Yb in clinopyroxenes of abyssal peridotites and spinel lherzolites. Data are from: Johnson et al. (1990) (solid circles), Liang & Elthon (1991), Stosch (1982) and Roden & Shimizu (1993) (open circles).**

Table 4.1: **Trace and minor elements in clinopyroxene of abyssal peridotites and spinel lherzolites. Ti and Zr values are in ppm; Na_2O in weight percent.**

REFERENCE	LOCALITY	SAMPLE	Ti	Zr	Na_2O
Johnson et al., 1990	Vulcan FZ	Vulc5:41-13	2615	10.6	
		Vulc5:41-15	2879	11.5	1.15
		Vulc5:41-30	1979	2.6	0.45
		Vulc5:41-33	1547	5.0	0.42
		Vulc5:41-45	1554	1.5	0.42
		Vulc5:34-56	796	0.6	
	Bullard FZ	Vulc5:35-1	754	0.6	0.31
		Vulc5:35-19	1893	4.5	
		Vulc5:35-22	886	0.3	
		Vulc5:35-30	779	0.3	
		Vulc5:37-3	1335	3.2	
	Bouvet FZ	All107:40-6	244	0.1	0.05
		All107:40-8	363	0.1	0.07
		All107:40-11	443	0.1	0.08
		All107:40-13	368	0.1	0.09
		All107:40-27	326	0.2	
	Islas Orcadas FZ	IO11/76:56-57	1608	2.2	0.62
		IO11/76:56-10	1420	1.4	
		IO11/76:56-54	1606	2.8	
		IO11/76:58-34	1113	1.1	0.64
	East of Shaka FZ	PS86:6-37	2674	11.0	
	Andrew Bain FZ	Prot5:15-90	1083	0.5	0.33
	Prince Edward FZ	Prot5:15-90	598	2.1	1.04
	Discovery FZ	Prot5:29-26	527	0.9	0.19
	Indomed FZ	Prot5:38-1	567	0.4	0.52
	Atlantis FZ	RC27:9-6-3	1525	2.1	0.34
		RC27:9-6-8	1702	1.7	
		RC27:9-25-142	1843	3.1	
Wilshire et al., 1988	Hill 1933, Dish Hill	35-4-1	3016		1.5
	California, USA	35-4-2	3836		1.5
		35-4-3	4016		1.6
		36-12-1	3177		1.3
		36-12-2	3296		1.3
		36-12-4	3117		1.3
		36-18-1	3776		1.5
		36-18-2	3716		1.5
		36-18-3	3476		1.4
Frey & Prinz, 1978	San Carlos, Peridot Mesa	PA-15A	3656		1.55
Galer & O'Nions, 1988	Arizona, USA	PM-251A	2937		1.1
		PM-330	2997		1.44
		PM-228J	3177		1.65
		PM-320A	2937		1.19
		PM-232A	1618		0.77
		PM-314A	3057		1.27
		PM-326B	3297		1.2
		PM-326A	1259		1.16
		PM-179A	2697		1.4
		PM-16A	2937		1.5
		PM-334	1457		1.09
		PM-1B30A	1079		1.05

Table 4.1 continued:

REFERENCE	LOCALITY	SAMPLE	Ti	Zr	Na_2O
Best, 1974	Western Grand Canyon	E36	600		0.5
	Arizona, USA	V86	600		0.2
Baldridge, 1979	Elephant Butte,	A245	3357		1.67
	New Mexico, USA				
Liang & Elthon, 1990	San Luis Potosi,	XDJ-1	3297		
	Mexico	XDJ-2	3417		
		XDJ-4	3237		
		XDJ-5	2338		
		XDJ-7	3416		
		XDJ-10	2817		
		XDJ-11	2637		
		XDJ-13	2757		
Stormer et al., 1975	Ascunion,Paraguay	-------	600		0.1
O'Reilly et al., 1991	Western Victoria,	9894-D	4795	42	1.9
	Australia	WGBM 12d	6054	95	1.71
Frey & Green, 1974		2669	2459		1.1
		2728	4076		1.63
Stosch & Seck, 1980	Dreiser Weiher, Germany	IB/5	1019		0.94
Cimmino et al., 1976	Assab Region, Afar	2493	1800		0.72
	Ethiopia	2490	1320		0.75
Roden & Shimizu, 1993	Lunar Crater, USA	LC-16	690	51	0.85
		LC-25	190	4	0.16
		LC-47	2360	27	0.95
	Black Canyon, USA	HD-10B	2220	39	1.16
		HD-13	3420	31	1.18
		HD-15	3150	60	0.98
		HD-16	1940	12	1.11
		HD-17	2710	24	0.99
		HD-18	2770	24	0.99

Table 4.2.: **Ti and REE concentrations in clinopyroxene of abyssal peridotites and spinel lherzolites. All values are in ppm. For localities compare with Table 4.1.**

REFERENCE	SAMPLE	TI	CE	ND	SM	EU	DY	ER	YB
JOHNSON ET AL., 1990	Vulc5:41-13	2615	0.43	1.83	1.22	0.60	2.87	1.87	1.71
	Vulc5:41-15	2879	0.50	1.92	1.24	0.57	2.56	1.79	1.61
	Vulc5:41-30	1979	0.06	0.71	0.78	0.35	1.94	1.22	1.18
	Vulc5:41-33	1547	0.17	0.60	0.70	0.32	1.78	1.14	1.18
	Vulc5:41-45	1554	0.04	0.40	0.41	0.20	1.75	1.06	1.10
	Vulc5:34-56	796	0.01	0.08	0.15	0.08	0.87	0.49	0.32
	Vulc5:35-1	754	0.02	0.10	0.22	0.11	1.05	0.72	0.54
	Vulc5:35-19	1893	0.33	0.61	0.50	0.21	1.71	1.01	0.74
	Vulc5:35-22	886	0.01	0.04	0.12	0.07	0.82	0.64	0.57
	Vulc5:35-30	779	0.02	0.12	0.17	0.09	1.16	0.79	0.89
	Vulc5:37-2	1335	0.05	0.56	0.58	0.30	1.78	0.98	0.78
	AII107:40-6	244	0.01	0.02	0.05	0.02	0.55	0.46	0.57
	AII107:40-8	363	0.04	0.13	0.08	0.04	0.48	0.50	0.63
	AII107:40-11	443	0.01	0.02	0.05	0.03	0.70	0.57	0.70
	AII107:40-13	368	0.01	0.01	0.05	0.03	0.38	0.43	0.46
	AII107:40-27	326	0.02	0.04	0.07	0.03	0.52	0.52	0.53
	IO11/76:56-57	1608	0.02	0.48	0.60	0.27	1.79	1.01	1.10
	IO11/76:56-10	1420	0.02	0.47	0.48	0.30	2.12	1.57	1.57
	IO11/76:56-54	1606	0.06	0.60	0.63	0.34	2.17	1.58	1.49
	IO11/76:58-34	1113	1.55	0.60	0.34	0.18	1.46	1.01	0.69
	PS86:6-37	2674	0.87	2.16	1.37	0.56	2.65	1.70	1.67
	PROT5:15-90	1083	0.02	0.24	0.38	0.18	1.18	0.69	0.74
	PROT5:19-2	598	1.02	0.58	0.26	0.12	0.95	0.71	0.62
	PROT5:29-26	527	0.07	0.13	0.13	0.06	0.56	0.51	0.48
	PROT5:38-1	567	0.03	0.12	0.15	0.08	1.02	0.74	0.54
	RC27:9-6-3	1525	0.04	0.47	0.62	0.33	1.93	1.17	0.78
	RC27:9-6-8	1702	0.03	0.57	0.76	0.39	2.67	1.72	1.74
	RC27:9-25-142	1843	0.11	0.91	0.92	0.47	2.40	1.50	1.63
LIANG & ELTHON, 1990	XDJ-1	3297	6.1		1.53	0.61			1.67
	XDJ-2	3417	5.12		1.67	0.67			1.74
	XDJ-4	3237	7.31		1.76	0.74			1.39
	XDJ-5	2338	4.76		1.62	0.62			1.76
	XDJ-7	3416	3.43		1.50	0.62			1.87
	XDJ-10	2817	3.36		1.34	0.52			1.82
	XDJ-11	2637	3.08		1.31	0.61			1.53
	XDJ-13	2757	3.22		1.27	0.53			1.74
RODEN & SHIMIZU, 1993	LC-1	99	6.1	1.9	0.35	0.08	0.17	0.14	0.16
	LC-16	690	21	17	5.8	1.7	2.5	0.94	1.1
	LC-25	190	1.2	0.78	0.39	0.14	0.54	0.35	0.29
	LC-47	2360	7.7	6.0	2.1	0.81	2.8	1.8	1.7
	HD-10	2220	8.3	6.2	2.2	0.77	1.7	0.85	1.0
	HD-11	1798	6.3	5.0	1.6	0.55	1.7	0.96	0.97
	HD-12	3896	7.2	5.3	2.0	0.74	2.2	1.2	1.2
	HD-13	3420	3.0	3.8	1.9	0.81	3.1	2.0	2.0
	HD-15	3150	25	14	3.8	1.2	3.0	1.5	1.6
	HD-16	1940	7.2	5.3	1.8	0.61	2.2	1.3	1.4
	HD-17	2710	2.8	3.0	1.5	0.59	2.5	1.4	1.5
	HD-18	2770	3.4	3.3	1.5	0.65	2.6	1.7	1.6
STOSCH, 1982	IB/8	2949	6.2	6.2	2.05	0.72			1.85
	K-1	2524	5.1	5.1	2.13	0.8	3.3		2.13
	D-50	1061	5.6	4.1	1.09	0.38	1.07	0.68	1.43
	D-58	1744	4.4	4.3	1.56	0.67	2.9		1.8

5. MELTING IN ABYSSAL PERIDOTITES

The focus of this chapter is the development and use of a hypothetical modal melting diagram (MM-diagram, hereafter) for abyssal peridotites.

5.1 Modal Melting Model

5.1.1 Historical Precedent: The MC-Diagram

Marsh (1982) elaborated the basis and utility of a modal crystallization (MC) diagram, which was first suggested by Schmincke (1967) and Swanson (1967). This approach establishes quantitatively the sequence of crystallization in basaltic samples and is based solely on phenomenological observations in thin sections of basalt. For simplicity, basalts can be imagined as mixtures of "relict" liquid (glass or groundmass) and phenocrysts of olivine, plagioclase feldspar, and pyroxene. Since at the liquidus there are no crystals but 100% melt and at the solidus there is no liquid but 100% crystals, surficial lavas that belong to a single extrusive event with varying phenocryst/matrix proportions should reveal the sequence of crystallization. Every sample shows a different phenocryst/matrix ratio according to its degree of crystallization. Thus, a plot of mode fraction of melt versus the mode fraction of plagioclase or clinopyroxene phenocrysts results in a proportional dependence (Schmincke 1967; Swanson 1967).

Marsh (1982) used modal analyses for the complete phenocryst assemblage in lavas from the Atka volcanic center and correlated it to the amount of melt (see Figure 5.1), assuming that the modal amount of melt plus the modal amount of phenocryst should add up to 100%. Of course, due to fast cooling the whole range of crystallization is not represented, but the geometry of this diagram allows an extrapolation to higher as well as lower degrees of crystallization.

Marsh (1982) suggested that the data may be dispersed because of insufficient point counting and inclusion of unrepresentative thin sections. Thus, some samples may

not reflect the "real" phenocryst/matrix ratio for that degree of crystallization, because physical processes in the flowing lava have accumulated or segregated phenocrysts. It is therefore possible that thin sections give the impression that the modal amount of mineral phases is higher or lower than it is on a large scale due to such selective processes.

In order to understand his argument, I have conducted a thought experiment that includes these situations. Assume an "artificial" magma composition which crystallizes for simplicity only two phases, plagioclase and pyroxene. This approach is instructive in outlining the effect of unrepresentative mineral/matrix ratios as they might appear in small scales of thin sections. An assumed sequence of crystallization ought to reflect the representative crystal/melt ratio and serves therefore as a reference line. This situation is illustrated in the upper left diagram in Figure 5.2, where the sequence of crystallization is indicated by the dashed line. The next step was to model combinations of gain and/or loss of one or both phase(s). Loss and gain of the phase(s) is modeled in 0.1 wt.% steps which were then required to achieve mass balance. Eight combinations consider all possibilities for gain and/or loss and are shown in Figure 5.2.

The points on the resulting MC-diagrams have been overlaid with the reference line in Figure 5.3 and are responsible for the data dispersion about it. The most striking result, in contradiction of Marsh's (1982) suggestion, is that scatter occurs both above and below the assumed sequence of crystallization. In addition, it can be seen that horizontal variations shorten as well as extend the sequence of crystallization. Therefore, if physical processes influence the crystal/melt ratio, the best approximation for the sequence of crystallization is likely to be within the scatter rather than above it. This observation is helpful to understand similar features for the inverted process of a modal melting diagram as introduced in the next paragraph.

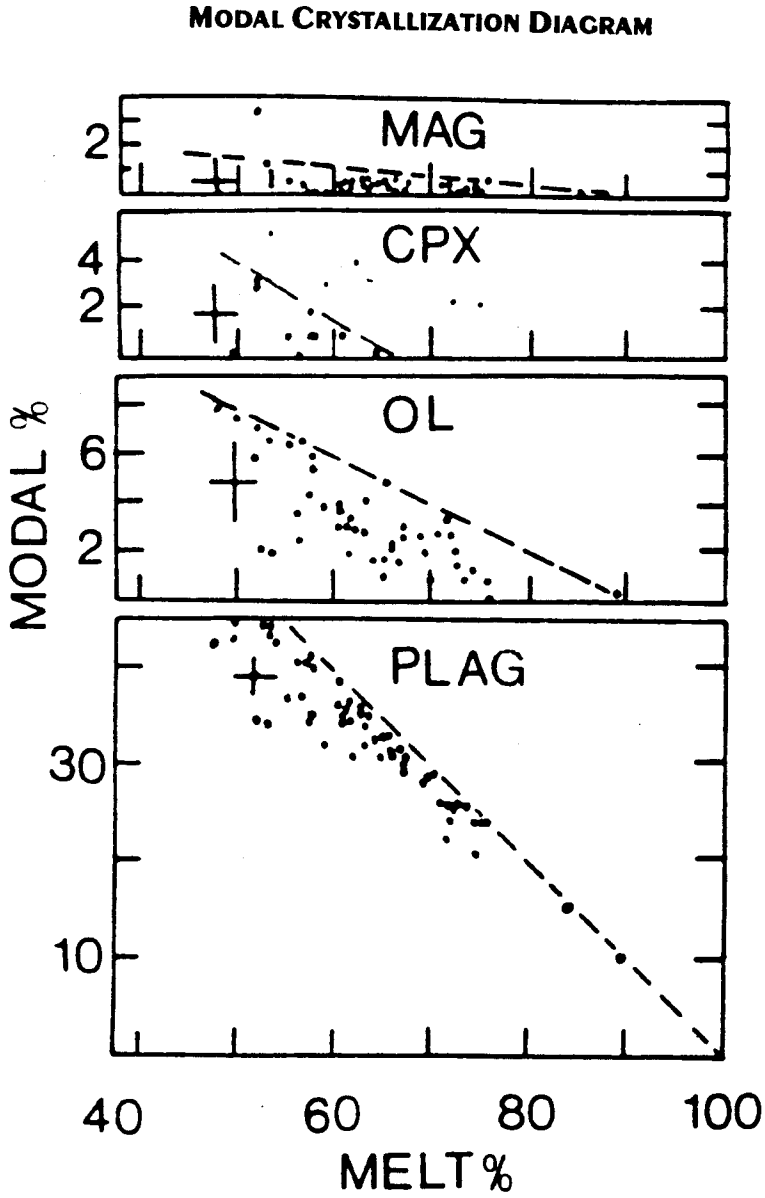

Figure 5.1: **MC-diagram for lava from Atka volcanic center, Aleutian Islands, Alaska. Error bars indicate the uncertainty in the mode due to insufficient point counting. Note that the well defined upper limit is assumed to represent the actual sequence of crystallization (after Marsh 1982).**

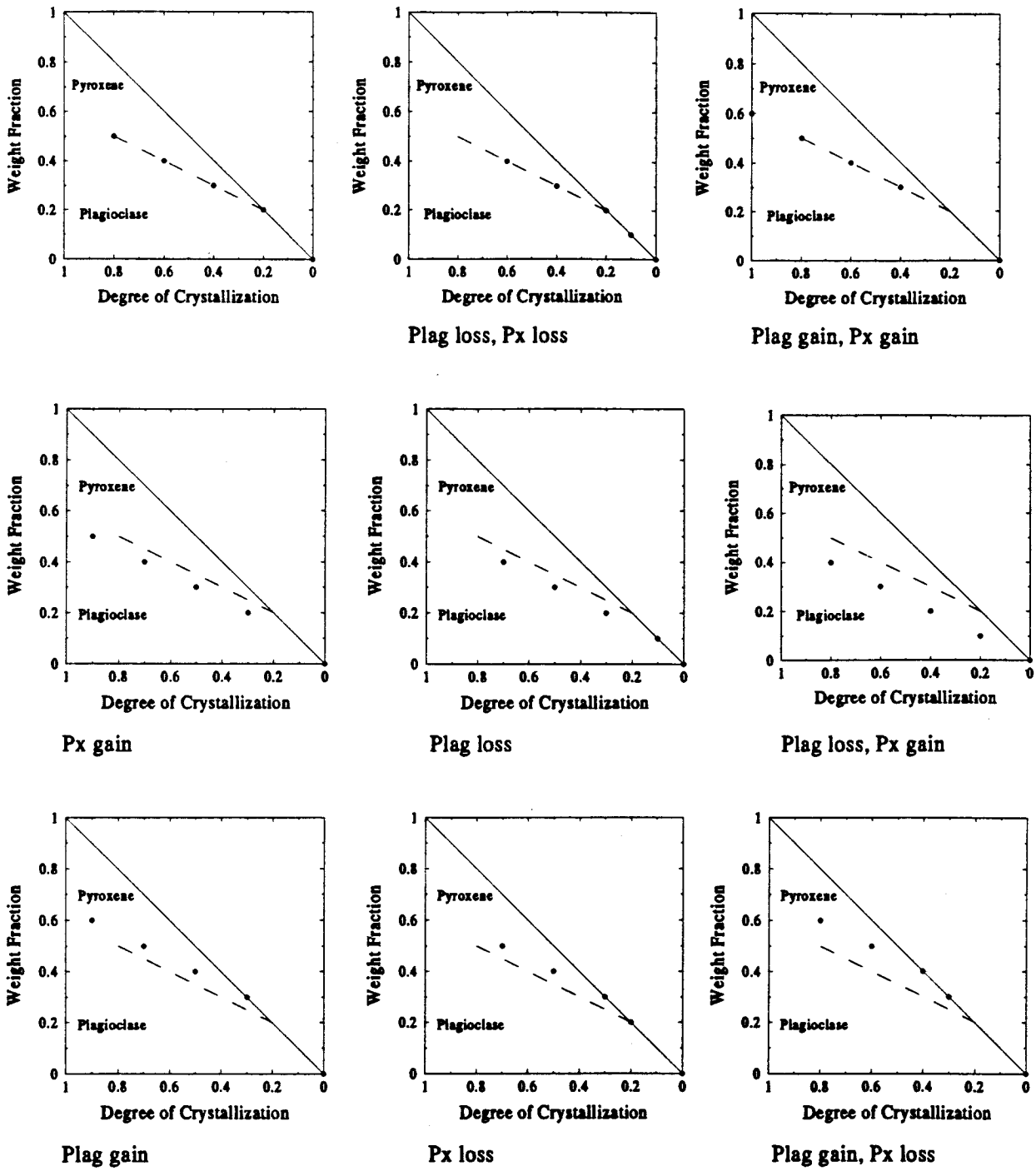

Figure 5.2: **Diagrams show eight possible situations for gain and/or loss of one or both phase(s) during the crystallization together with the assumed sequence of crystallization (dashed line) from the upper left diagram.**

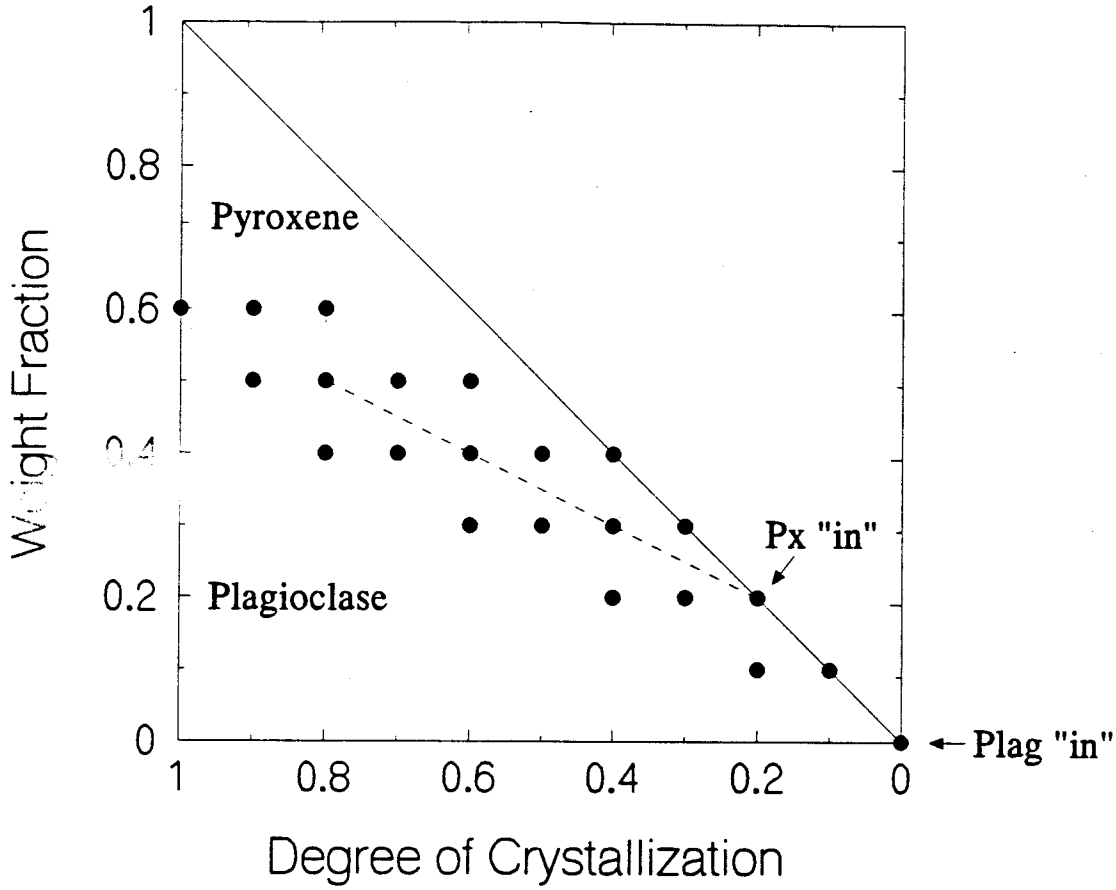

Figure 5.3: **Plot shows the overlay for diagrams of Figure 5.2. Scatter about the dashed line indicates unrepresentative crystal/melt ratios.**

5.1.2 Construction of the MM-Diagram

The amount of melt which has been extracted from an abyssal peridotite is calculated by solving the Johnson et al. (1990) fractional melting equation for F (variables are explained in Appendix A):

$$F = \frac{D_i^0}{P}\left[1-\left(\frac{C_i^{cpx}}{C^{0,cpx}}\right)^{\left(\frac{P}{1-P}\right)}\right]$$

The concentration of Ti in the original clinopyroxene is estimated to be 4000 ppm. The starting mode (in weight fraction) is assumed to be 0.55 for olivine, 0.25 for orthopyroxene, 0.18 for clinopyroxene and 0.02 for spinel. Although these values were specified as "vol.%" by Johnson et al. (1990, Table A2, p.2676), they would change very slightly by density normalization; hence I have used them directly as given here. These modes are consistent with a LREE-depleted lherzolite (Johnson et al. 1990, reference therein). The proportions of mineral phases entering the liquid are the peritectic melt in a four phase mineral assemblage of a spinel lherzolite. Thus, the melting mode is assumed to be (Johnson et al. 1990, reference therein): 0.10 for olivine, 0.20 for orthopyroxene, 0.68 for clinopyroxene and 0.02 for spinel (the same "vol.%" comment applies as above). Importantly, all modeling calculations are reported in terms of Ti abundance in the clinopyroxene of the residues. The concentration abundance for Ti in the clinopyroxene varies between 244 ppm for the most depleted to 2879 ppm for the least depleted sample (Johnson et al. 1990).

Figure 5.4 illustrates how the modal composition changes as a function of F. Modal compositions for the abyssal peridotites have been converted into weight percent assuming an average density of 3.3 g/cm^3 for olivine, 3.3 g/cm^3 for orthopyroxene, 3.0 g/cm^3 for clinopyroxene and 4.1 g/cm^3 for spinel. Since the abundance of Ti in the

clinopyroxene specifies the degree of melting (see equation above), the sample with the highest Ti concentration yields the lowest degree of melting and vice versa. The range of melting for the samples lies roughly between 0.05 and 0.27.

The modal composition of every sample is defined by three different symbols (see legend in Figure 5.4). The y-axis gives the modal composition in terms of weight fraction normalized to the calculated value of F. For example, the sample with the lowest degree of melting (F~0.05) has weight fractions of 0.64 Ol, 0.23 Opx, 0.113 Cpx and 0.017 Sp. Since mass balance requires that

$$x^{OL} + x^{OPX} + x^{CPX} + x^{SP} + F = 1,$$

the weight fractions of the mineral phases have to be normalized to 0.95 (=1-F or =1-0.05). This normalization led to following weight fractions:

0.608 Ol,	■	
0.219 Opx	▲	(0.827[Ol+Opx]-0.608[Ol]=0.219[Opx]),
0.107 Cpx	◇	(0.934[Ol+Opx+Cpx]-0.827[Ol+Opx]=0.107[Cpx])
0.016 Sp	1:1 line	(0.95[Ol+Opx+Cpx+Sp]-0.934[Ol+Opx+Cpx])=0.016[Sp])

Therefore, the field above the 1:1 line in the MM-diagram describes the weight fraction of melt extracted from a given sample according to its degree of melting.

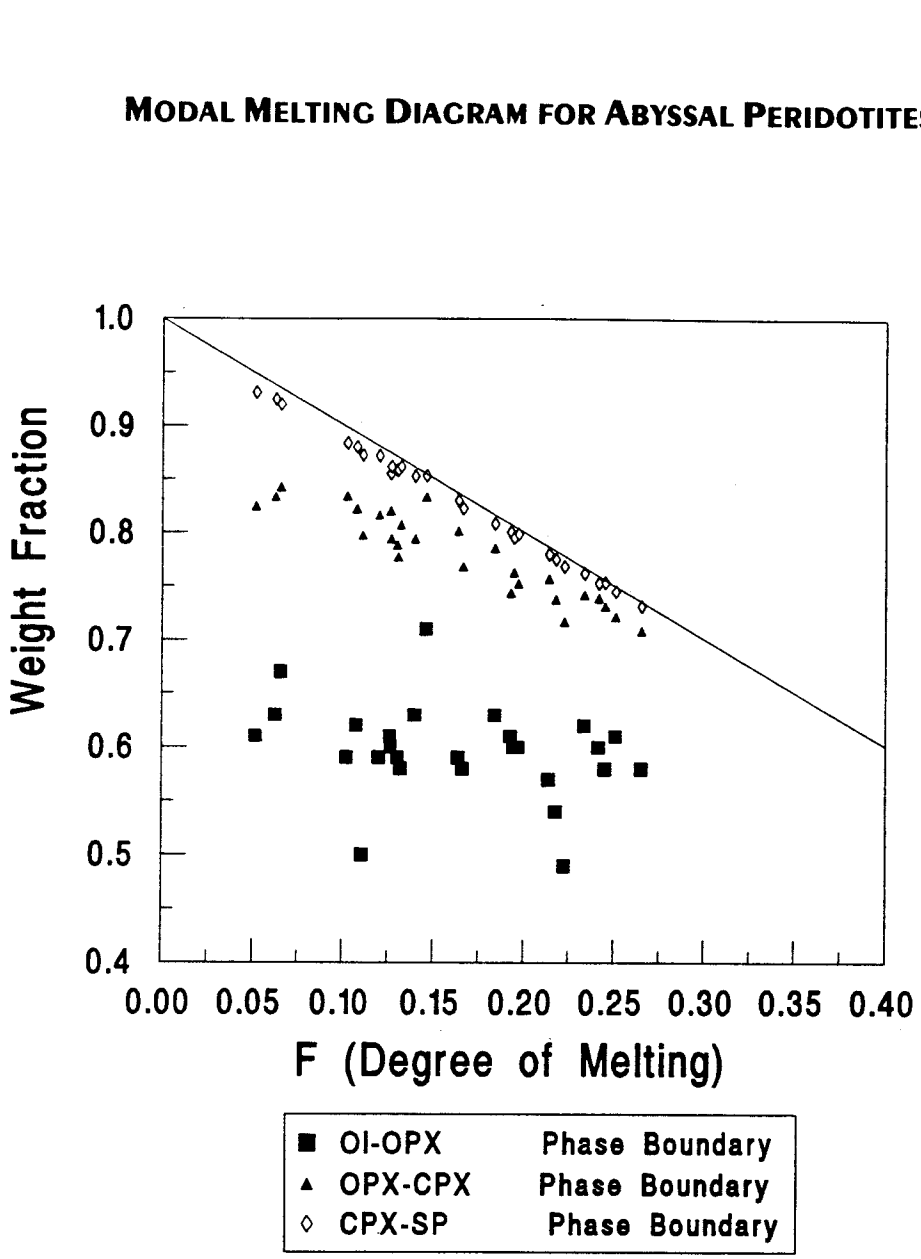

Figure 5.4: **MM-diagram for abyssal peridotites. Corresponding modal data of the samples are listed in Table 5.3. The degree of melting is calculated with the Ti concentration in clinopyroxenes presented in Table 4.1. Different symbols indicate the phase boundaries in terms of weight fraction for the spinel lherzolite assemblage. The field above the 1:1 line corresponds to the melt fraction (i.e., F).**

5.2 Implications for the MM-Diagram

5.2.1 Calculation of F

The empirical MM-Diagram is in agreement with the experimental observation that with continuous melting clinopyroxene and spinel are the first mineral phases to vanish, leaving an increasingly harzburgitic composition behind (e.g. Mysen & Kushiro 1977; Jaques & Green 1980). As discussed in the previous section, a generalized sequence of melting can be estimated from natural samples by calculating regression lines for the three phase boundaries, leading to a least-squares MM-model as shown in Figure 5.5. Extrapolation of these lines to higher F gives intersections with the 1:1 line where each mineral phase is exhausted. The intersections with the y-axis, however, define the initial modal composition at F=0.

These best-fit lines provide an empirical "calibration" between degree of partial melting and residual modal composition. The obvious question then arises: how can this scheme be inverted to calculate F for a sample in which only the modal abundances are known? Certainly, it is unlikely that the modal composition of a given spinel lherzolite will fit exactly on the regression lines at a particular F, even though it is possible. Therefore, it is necessary to find the best-fit of a given sample to all three regression lines at a certain F where the deviations are at a minimum. (Conceptually and graphically, this approach is analogous to the use of seismic travel-time curves to estimate distance to the epicenter.)

For a given sample we know the mass fractions of the four mineral phases :

$$\overset{OL}{X}_{Sample},\quad \overset{OPX}{X}_{Sample},\quad \overset{CPX}{X}_{Sample},\quad and\ \overset{SP}{X}_{Sample},$$

but F is unknown. We know further, as shown schematically in Figure 5.6, the numerical values for the regression line equations as well as their intersections with the y-axis and the 1:1 line.

Mass balance requires:

$$x^{OL}_{Sample} + x^{OPX}_{Sample} + x^{CPX}_{Sample} + x^{SP}_{Sample} = 1 - F$$

$$x^{OL}_{Initial} + x^{OPX}_{Initial} + x^{CPX}_{Initial} + x^{SP}_{Initial} = 1$$

The slope (a) of a regression line through two points can be expressed as:

$$\frac{y - y'}{x - x'} = \frac{y' - y''}{x' - x''} = a$$

which for the case of the Ol-Opx phase boundary becomes:

$$\frac{x^{OL}_{Initial} - x^{OL}_{Sample}}{0 - F} = \frac{x^{OL}_{Sample} - x^{OPX}_{0}}{F - F^{OPX}_{0}}$$

All values except F are known from the regression line parameters or sample mode, so that this equation can be simplified to:

$$aF = b$$

Similar equations can be derived for the Opx-Cpx and Cpx-Sp regression lines, so that:

$$cF = d$$
$$eF = g$$

The best-fit value of F for a given sample can then be derived from these three linear equations by using matrix algebra,

$$\begin{aligned} aF &= b \\ cF &= d \\ eF &= g \end{aligned} \Rightarrow \begin{bmatrix} a \\ b \\ c \end{bmatrix} F = \begin{bmatrix} b \\ d \\ g \end{bmatrix} \Rightarrow AF = B$$

where A and B are column vectors.

This equation can be solved for F. Multiplying both sides by the transpose of A gives:

$$A^T A F = A^T B$$

And then multiplying both sides by the inverse of $A^T A$ gives:

$$\left[A^T A\right]^{-1} A^T A F = \left[A^T A\right]^{-1} A^T B$$

which in effect isolates F on the left-hand side:

$$F = \left[A^T A\right]^{-1} A^T B$$

In Appendix B, F has been calculated for another population of abyssal peridotites according to this method. The modal abundances of these samples were taken from Johnson & Dick (1992) and the calculations have been performed with the Program "Mathcad".

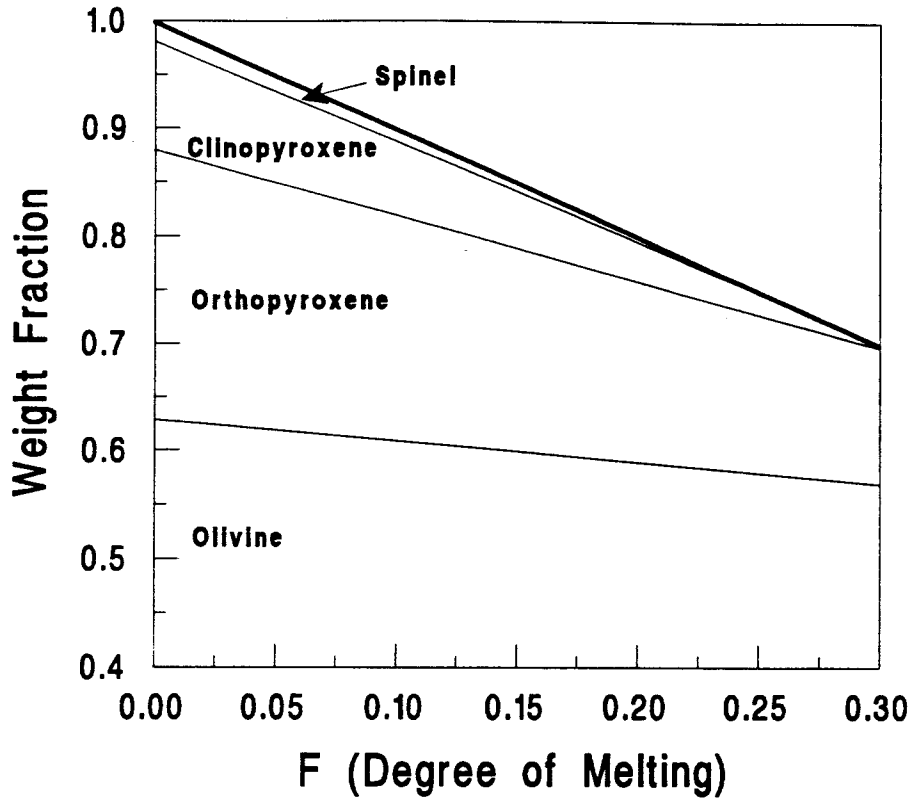

Regression Lines:

Ol-OPX	Phase Boundary:	→	y = 0.63 - 0.20x	r^2 = 0.08
OPX-CPX	Phase Boundary:	→	y = 0.88 - 0.61x	r^2 = 0.85
CPX-SP	Phase Boundary:	→	y = 0.98 - 0.94x	r^2 = 1.00

Figure 5.5: **Least-squares MM-model.**

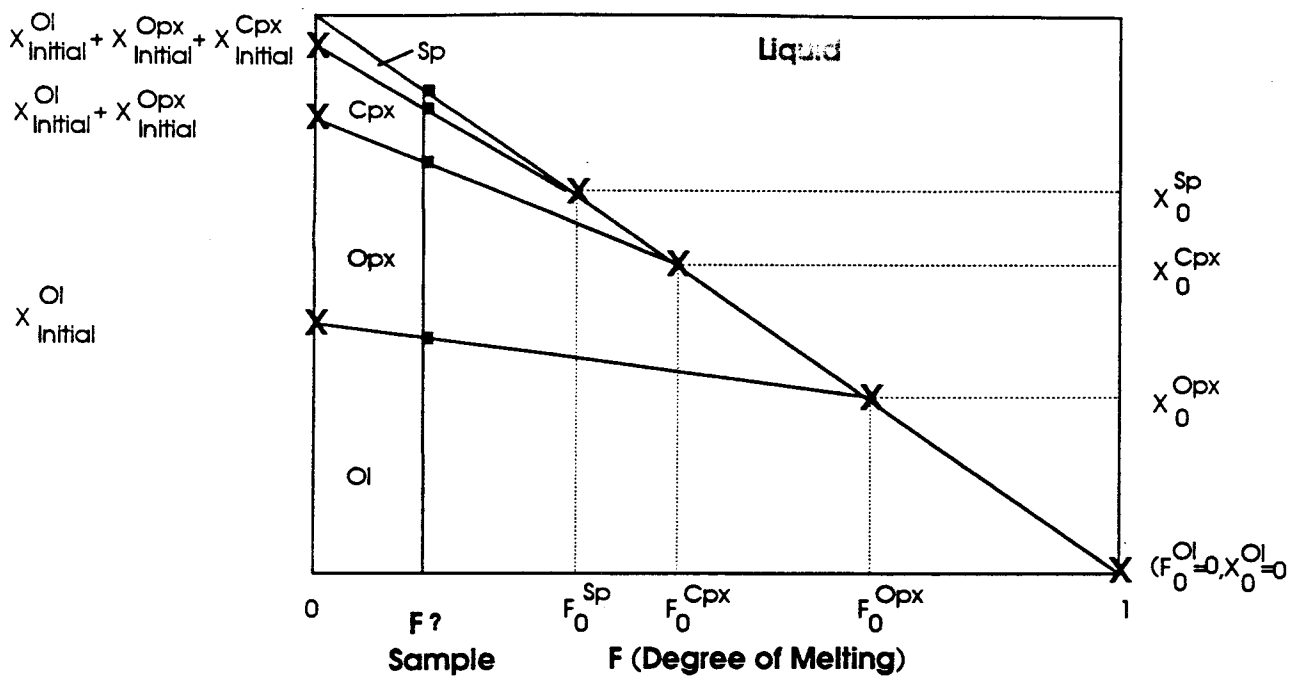

Figure 5.6: **Schematic MM-Model showing notation used to relate the numerical parameter of the regression lines to the least-squares formulation for calculation of F in an unknown sample.**

5.2.2 Calculation of the Starting Composition

Another possibility that arises from the geometry of the MM-diagram as described in 5.1.2 is the calculation of the starting composition of the upper lithospheric mantle at F=0. The weight fractions of the four phases in the starting composition are given by the intersections of the regression lines with the y-axis as shown in Figure 5.5. Here, the weight fractions are 0.63 for olivine, 0.25 for orthopyroxene, 0.1 for clinopyroxene and 0.02 for spinel. In order to calculate the composition of *this starting assemblage*, the initial compositions of the *individual phases* must first be estimated. This is done in Figures 5.7-5.10 by plotting the microprobe analyses (Johnson et al. 1990) versus the degree of melting. Again, intersections of these regression lines deliver the weight concentrations of the elements at F=0.

Results are listed in Table 5.1 together with other estimated primitive mantle compositions. Also listed is the upper mantle composition at F=0 for "Operation ⑥" (see Table 5.2 and paragraph 5.4.1), which gives values for the calibrated MM-model.

SiO_2 and MgO contents of the upper mantle compositions as derived from the MM-diagrams show, compared to others, a slight mismatch where the SiO_2 and MgO contents are a few percent lower and higher, respectively. Also, the Na_2O and TiO_2 contents are much lower compared to other suggested compositions. Otherwise, the starting compositions of this study are in good agreement with other suggested primitive mantle compositions as shown in Table 5.1.

5.2.3 Calculation of the Melt Composition

Regression line equations for the microprobe analyses of all for phases (Figures 5.16, 5.17, 5.18, 5.19) as well as weight fractions obtainable from the least-squares MM-model (Figure 5.5) at certain degrees of melting allow calculations for the melt composition. In Appendix C, whole rock compositions for "averaged" residuals and melt compositions of defined increments are listed.

Table 5.1: **Upper mantle starting compositions.**

	*	**	H&Z	K&G	B&S	R	M&A
SiO_2	43.47	43.72	45.96	46.32	45.5	45.1	44.71
TiO_2	0.08	0.08	0.18	0.17	0.11	0.2	0.16
Al_2O_3	3.82	3.97	4.06	3.94	3.98	3.3	2.46
FeO †	8.65	8.56	7.54	7.65	7.18	8.0	8.15
MnO	0.19	0.18	0.13		0.13	0.15	0.18
MgO	40.88	40.35	37.78	38.44	38.3	38.1	41.00
CaO	2.28	2.49	3.21	3.19	3.57	3.1	2.42
Na_2O	0.10	0.11	0.33	0.28	0.31	0.4	0.29
K_2O			0.03	0.01		0.03	0.09
Cr_2O_3	0.32	0.34	0.47		0.68	0.4	0.42
NiO	0.21	0.2	0.28		0.23	0.2	0.26
SUM	100	100	99.97	99.91	99.99	98.98	100.14

Abbreviations:

† = all iron is reported as Fe^{2+}
* = this study, MM diagram (Figures 5.5, 5.7, 5.8, 5.9, 5.10)
** = this study, "Operation 6" of Table 5.2, p.5-36 (Figures 5.20, 5.7, 5.8, 5.9, 5.10)
H & Z = Hart & Zindler (1986)
K & G = Kinzler & Grove (1992b)
B & S = Baker & Stolper (1993)
R = Ringwood (1979)
M & A = Maaloe & Aoki (1977)

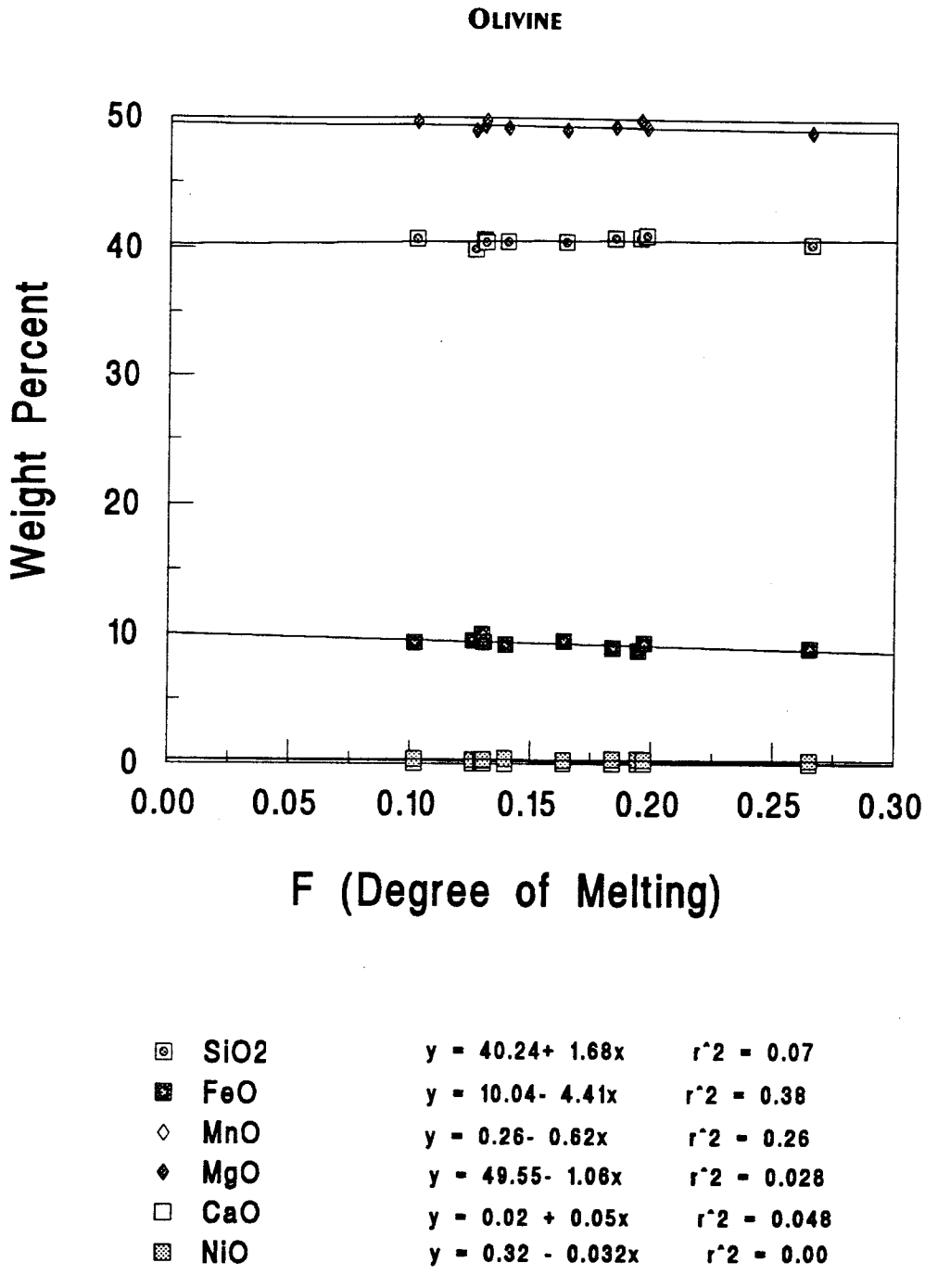

Figure 5.7 : **Major and minor oxide concentration (see Table 5.4) of olivine as a function of F. Intersections of regression lines with the y-axis give estimates for initial concentrations. Note that the MnO symbols are overlaid by others.**

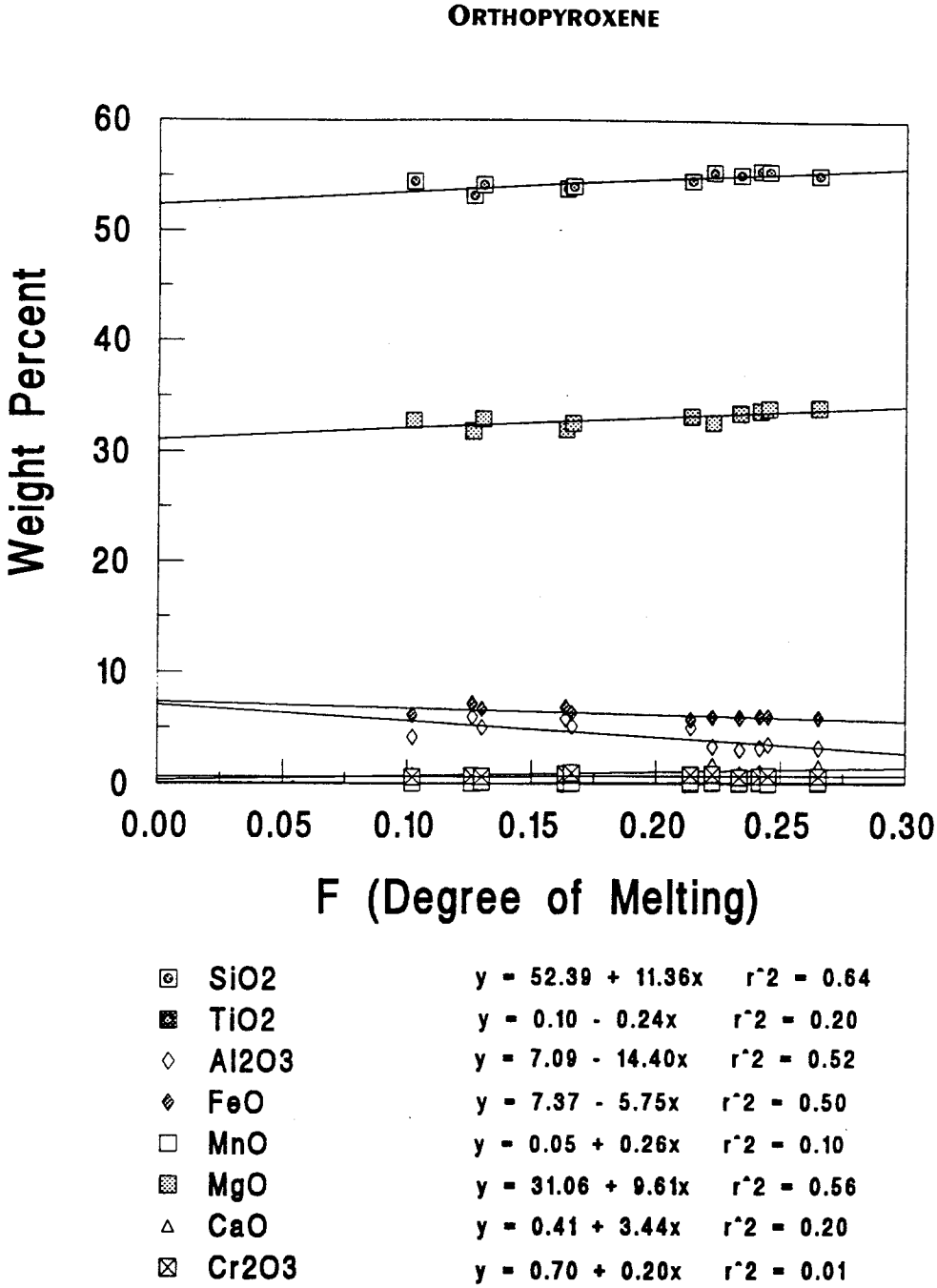

Figure 5.8: **Major and minor oxide concentrations (see Table 5.4) of orthopyroxene as a function of F. Intersections of regression lines with the y-axis give estimates of the initial concentrations. Note that TiO_2 and MnO symbols are overlaid by others.**

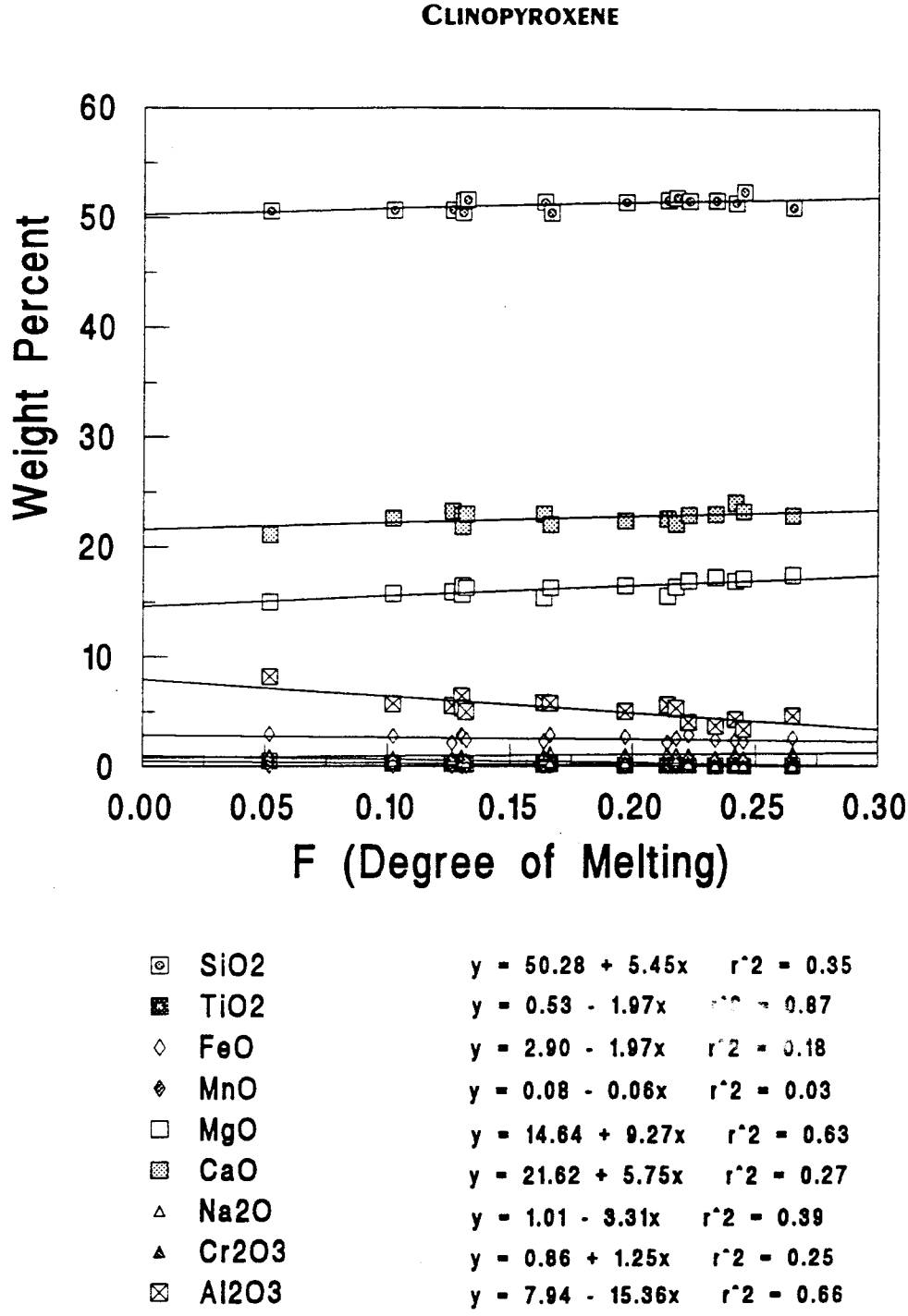

Figure 5.9: **Major and minor oxide concentration (see Table 5.4) of clinopyroxene as a function of F. Intersections of regression lines with the y-axis give estimates of initial concentrations.**

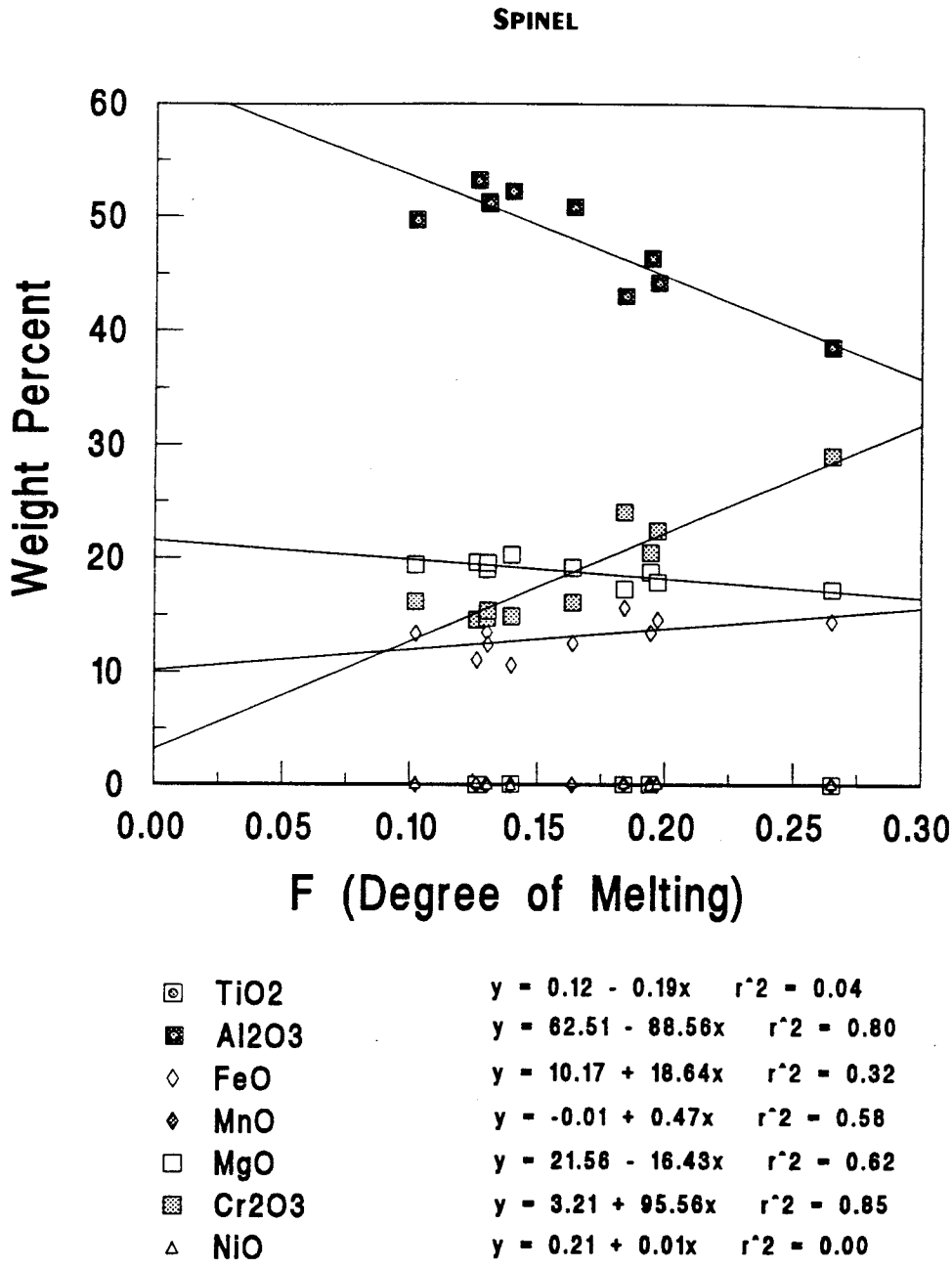

Figure 5.10: **Major and minor oxide concentrations (see Table 5.4) of spinel as a function of F. Intersections of regression lines with the y-axis give estimates of initial concentrations.**

5.3 Sensitivity of the MM-Diagram to Model Parameters

Both the concept and the application of the MM-diagram are highly model-dependent because of the central place of the fractional melting equation in its formulation. Thus, the basic assumptions behind *any* use of this equation also underlie the MM-diagram:

① initial Ti in Cpx;

② constant $D_{Ti}^{Cpx/Liquid}$;

③ constant melting proportions;

④ starting mode reflects mantle;

⑤ equilibrium is maintained among all phases; and

⑥ melt continuously removed (i.e., pure fractional melting)

The following sections examine the sensitivity of the MM-diagram, as "calibrated" by the abyssal harzburgite modal and Cpx-Ti data, to changes in the first four of these model parameters.

5.3.1 Ti Concentration in Initial Clinopyroxene

Section 5.1 assumes a Ti concentration of 4000 ppm as an initial concentration of the clinopyroxene in the source rock. The effect of this assumption was tested by introducing changes of ±10% in the starting abundance. Therefore, three samples with a low, medium and high degree of melting have been recalculated assuming that $C_{Initial}^{Cpx}$ is 4400 ppm and 3600 ppm.

Figure 5.11 shows the following results: First, a variation in the initial Ti concentration will largely shift the data along the boundaries between the phase values. Thus, a different starting composition will have little influence on the regression lines for the entire population, but will shift the calculated melt fraction F for a given sample to higher and lower values for a lower and higher starting abundance, respectively. Second, this effect becomes smaller with increasing degree of melting.

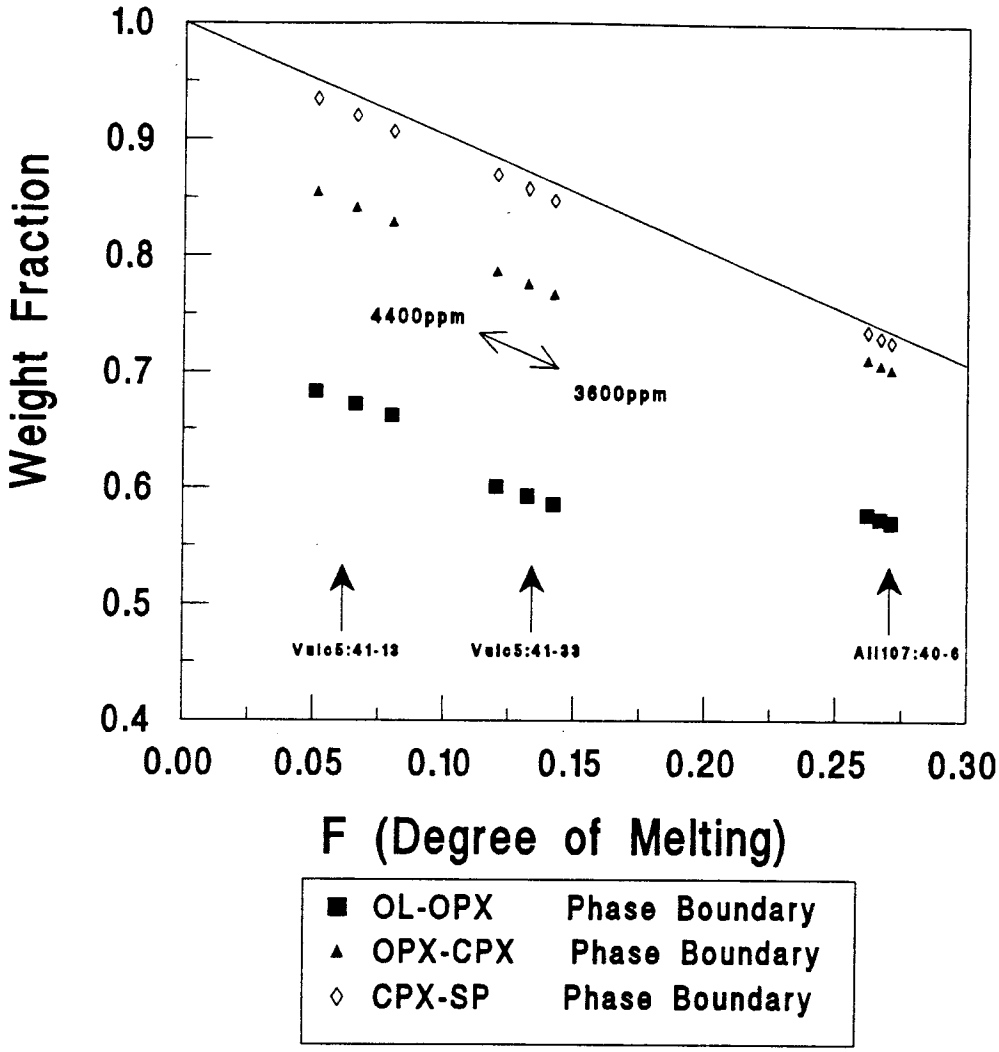

Figure 5.11: **MM-Diagram shows the effect on calculated F for three representative abyssal harzburgites for ±10% change of the Ti concentrations in the source rock clinopyroxene. Note that the spread increases with decreasing degree of melting.**

5.3.2 Cpx/Liquid Distribution Coefficient for Ti

Partitioning of major and minor elements between crystalline phases and melt is controlled by temperature, pressure and composition of the phases. Although abyssal peridotites have in all probability shared a generally common melting history (Dick et al. 1984), the detailed temperature-pressure conditions remains unresolved. At a minimum, however, it is clear that Cpx bulk composition changes during melting (Johnson et al. 1990; and Figures 5.7-5.10). A constant distribution coefficient might therefore be questioned. Since the model is strongly dependent on the partitioning between pyroxene and liquid, an examination of the pyroxenitic major components is appropriate.

The cpx/liquid distribution coefficient for Ti is assumed to be 0.44 for the whole range of melting. This value was averaged from melting experiment studies on glassy rims from ocean-floor basalt pillow lavas from the East Pacific Rise and the Mid-Atlantic ridge and existing literature data (Johnson 1990, and references therein). Two more extreme (but still constant) values of $D_{Ti}^{Cpx/Liquid}$, 0.2 and 0.6, have been used to outline the effect of this variable in Figure 5.12 a and b. Evidently, as $D_{Ti}^{Cpx/Liquid}$ becomes smaller, the resulting range and degree of melting also becomes smaller.

Alternatively, $D_{Ti}^{Cpx/Liquid}$ may change as a function of clinopyroxene bulk composition. Effects of composition and temperature on the partitioning of trace elements at 1 atmosphere between high Ca-pyroxene and natural mafic to intermediate lavas have been extensively studied by Nielsen et al. (1992) and Gallahan & Nielsen (1992). They found a strong positive correlation of $D_{Ti}^{Cpx/Liquid}$ with $D_{REEs}^{Cpx/Liquid}$ for samples with increasing wollastonite content in the clinopyroxene. Further, they were able to show a positive non-linear correlation between the Al content of the melt and $D_{Ti}^{Cpx/Liquid}$.

Figures 5.13 a and b show the change of Al_2O_3 and CaO in clinopyroxenes analyzed by Johnson et al. (1990) as a function of F calculated assuming $D_{Ti}^{Cpx/Liquid}$=0.44. It is clear that Al_2O_3 decreases significantly and CaO increases with increasing F. Combined with the results of Nielsen et al. (1992) and Gallahan & Nielsen (1992), this

suggests that a more sophisticated model in which $D_{Ti}^{Cpx/Liquid}$ increases slightly with decreasing F might be appropriate.

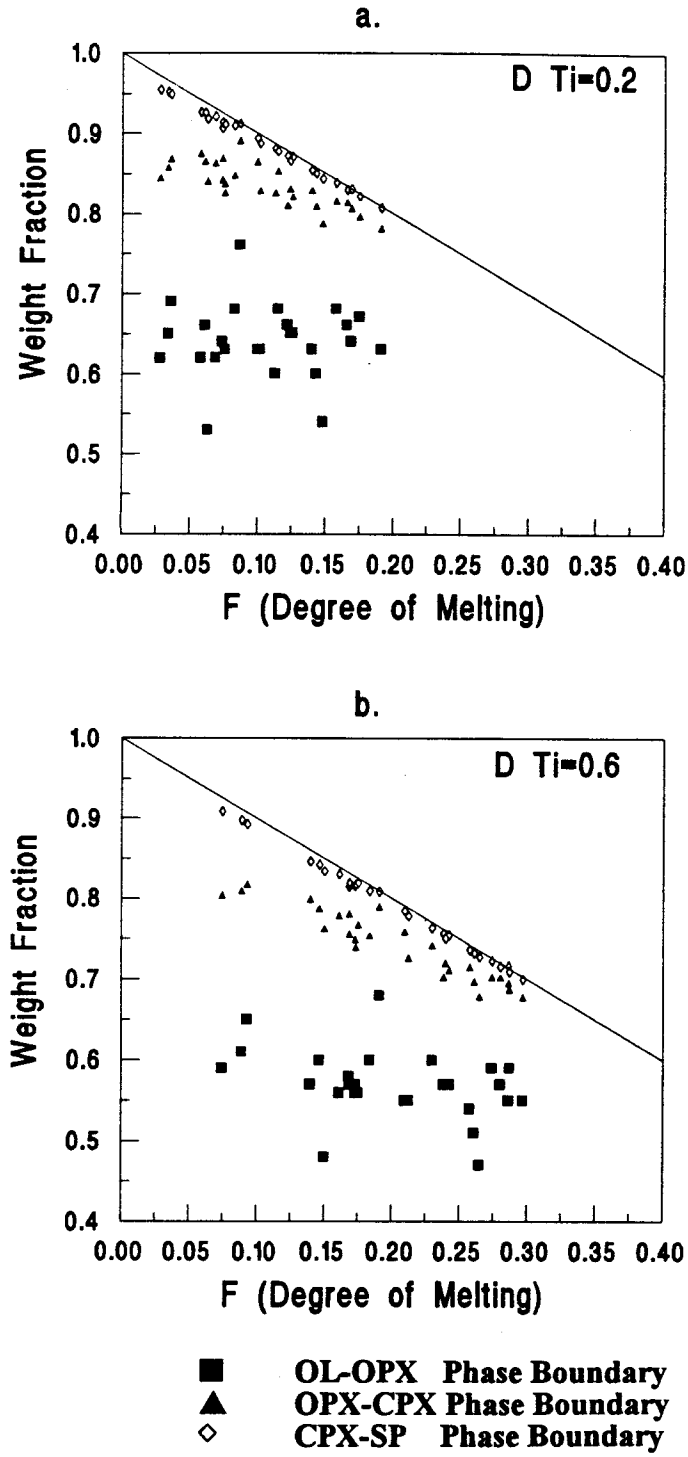

Figures 5.12 a, b: **MM-diagrams recalculated with different $D_{Ti}^{Cpx/Liquid}$. A comparison shows that a lower $D_{Ti}^{Cpx/Liquid}$ shifts the range of melting to lower values.**

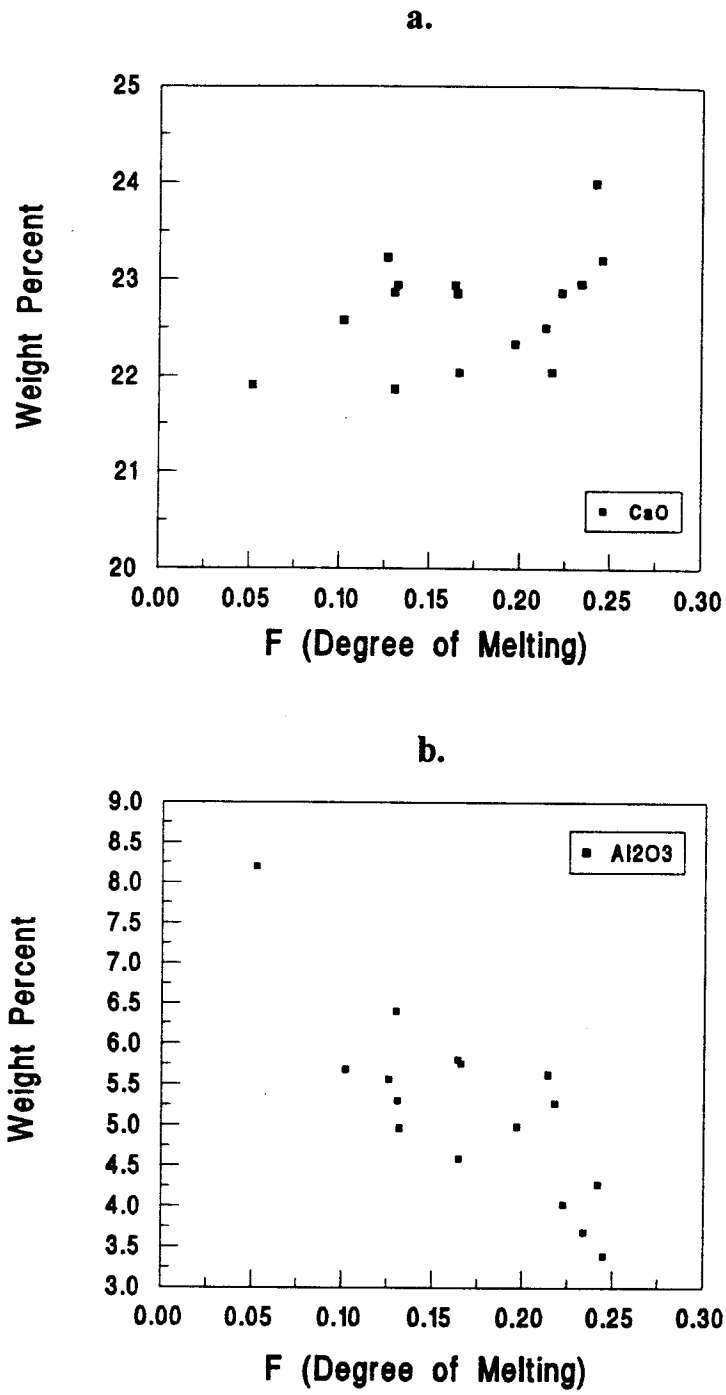

Figures 5.13 a, b: **CaO and Al_2O_3 in abyssal harzburgite clinopyroxenes as a function of F.**

5.3.3 Other Trace-Elements as Model Parameters

Theoretically, the whole inventory of trace elements should have experienced the same melting history. Therefore, it might be expected that, regardless of which trace element is examined, the abundance and the partitioning behavior should lead to similar MM-diagrams.

Zr, Nd, Eu, and Er which are representatives for the HSF, LRE, MRE and HRE elements, respectively, were chosen to construct further MM-diagrams. Distribution coefficients, trace element concentrations and estimated starting abundances were taken from Johnson et al. (1990, and references therein). The starting abundance is 30 ppm for Zr, 4.11 ppm for Nd, 0.67 ppm for Eu and 1.92 ppm for Er. Results are shown in Figures 5.14-5.17.

The Zr MM-diagram is the most similar to the Ti MM-diagram. REE MM-diagrams, however, show different results. All of them reflect a lower degree of melting for the least depleted sample and vary in the range of melting. Additionally, the Nd and Eu MM-graphs suggest that the Ol weight fraction increases during melting so that corresponding regression lines would show a positive slope.

However, Ti represent the most useful element for this kind of modeling since its partitioning behavior is by far better constrained by experiments in ultramafic minerals than it is for Zr or REE (R. Nielsen, 1993, per. comm.).

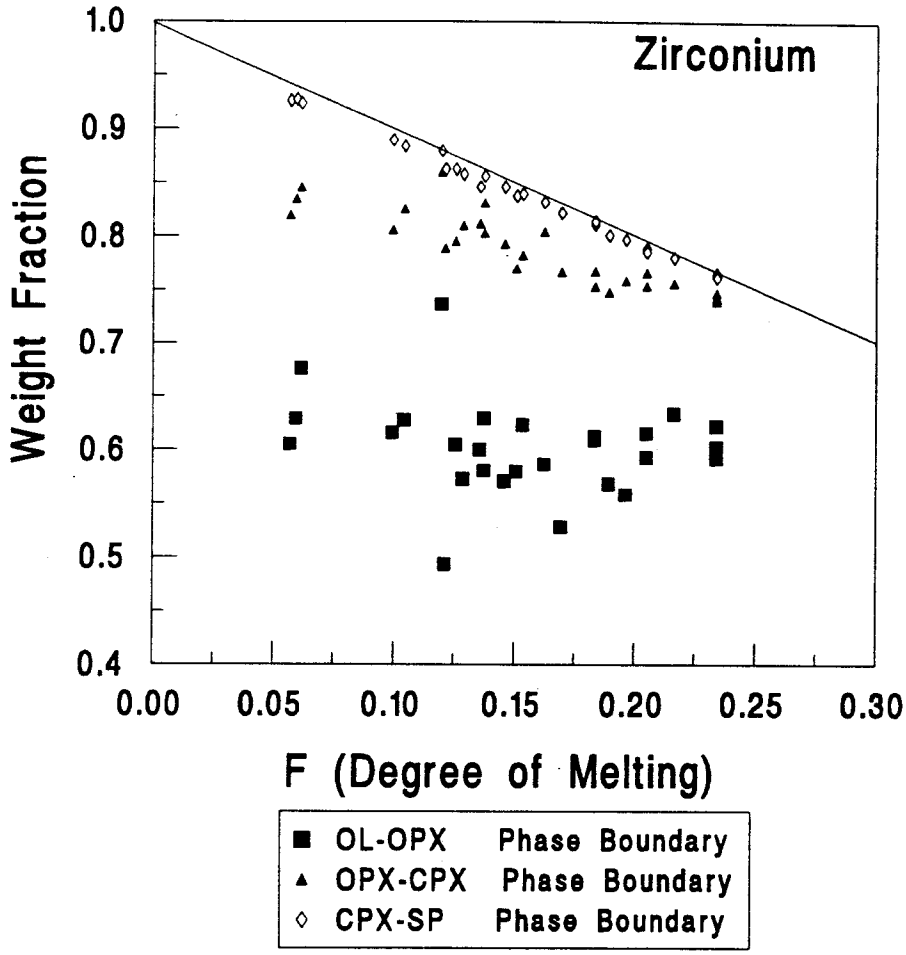

Figure 5.14: **MM-diagram constructed with the abundance and partitioning of Zr. Symbols are the same as in Figure 5.4.**

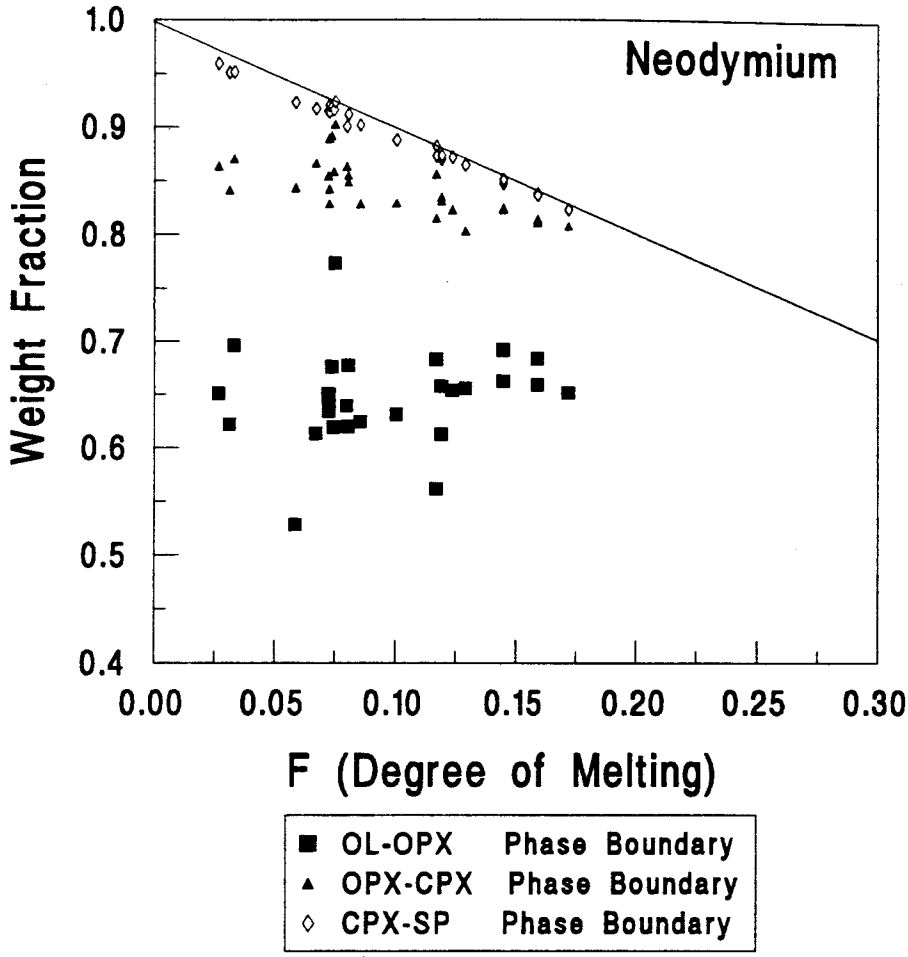

Figure 5.15: **MM-diagram constructed with the abundance and partitioning of Nd. Symbols are the same as in Figure 5.4.**

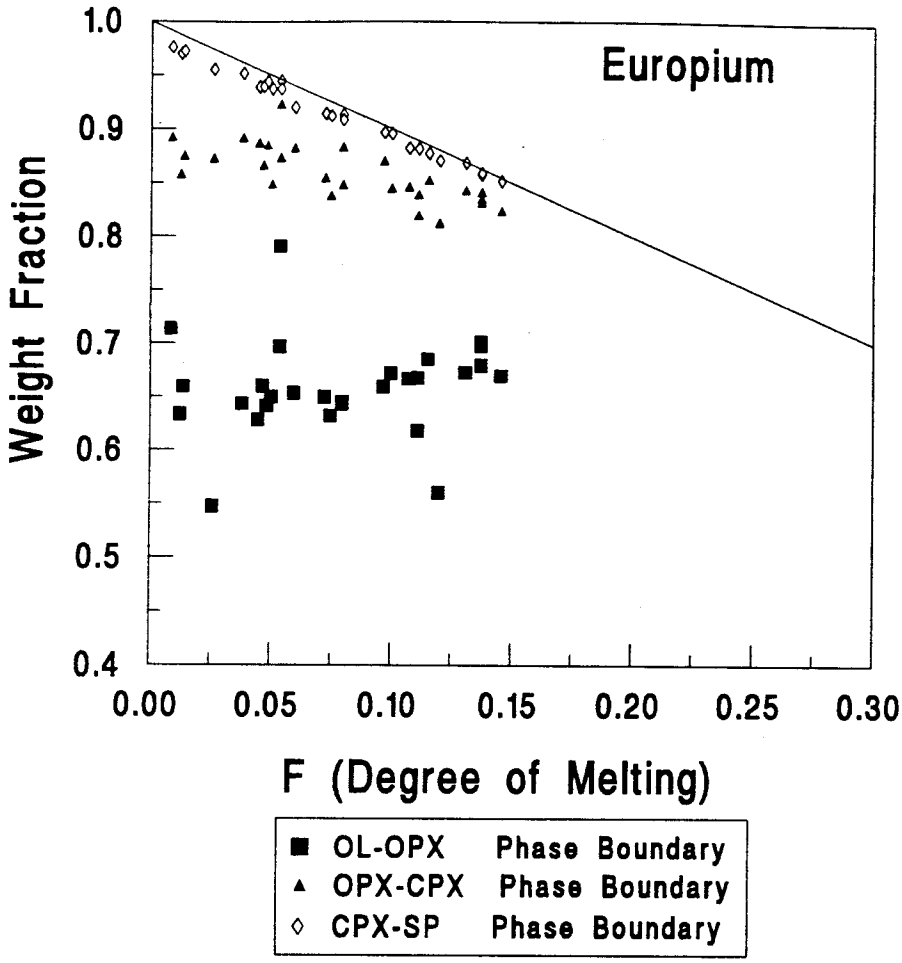

Figure 5.16: **MM-diagram constructed with the abundance and partitioning of Eu. Symbols are the same as in Figure 5.4.**

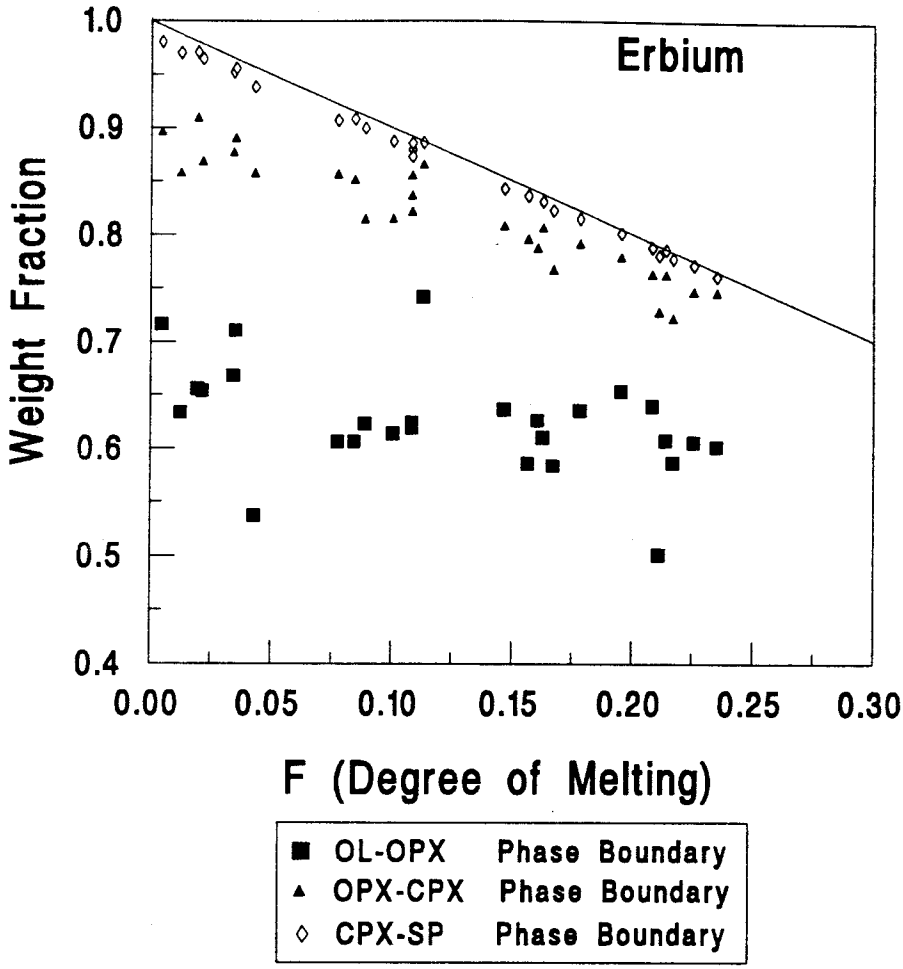

Figure 5.17: **MM-diagram constructed with the abundance and partitioning of Er. Symbols are the same as in Figure 5.4.**

5.4 Calibration of the MM-Diagram

In principle, there are at least three ways in which the MM-diagram could be calibrated for use as a "standard" for application to other peridotite suites. (Again, there are logical and topological parallels with standardization of seismic travel-time curves.) Section 5.1.2 discussed the modal-Cpx Ti calibration. This section addresses a calibration based on experimental petrology and then compares it to the modal one. A third possible calibration based on thermodynamic constraints is beyond the scope of this thesis.

Kinzler & Grove (1992 a, b, 1993) and Baker & Stolper (1993) have recently conducted high-pressure melting experiments on spinel lherzolite compositions relevant to this thesis and synthesized their results with those of earlier experiments. Although different in design, both studies yielded reaction coefficients for the mantle melting reaction which in general is expressed as:

$$1 \text{ Mass Unit Melt} = \gamma \text{ Ol} + \beta \text{ Opx} + \alpha \text{ Cpx} + \varepsilon \text{ Sp}$$

where γ, β, α and ε are the proportions of the mineral phases Ol, Opx, Cpx and Sp, respectively.

The reaction coefficients are equivalent to the melt mode in the melting equation given by Johnson et al. (1990). Experimental melting studies have shown that this reaction is "odd" (Baker & Stolper 1993; Kinzler & Grove 1992 a, b, 1993), meaning that olivine is generated during melting and has therefore a negative sign on the side of the mineral phases:

$$1 \text{ Mass Unit Melt} + \text{Ol} = \text{Opx} + \text{Cpx} + \text{Sp}$$

where:

	γ	β	α	ε
Kinzler & Grove (1992a)	-0.3	0.4	0.82	0.08
Baker & Stolper (1993)[1]	-0.22	0.37	0.73	0.12

[1]= reaction coefficients given by Baker & Stolper (1993) normalized for mass balance requirements

The experimentally-determined reaction coefficients listed above were used to construct phase boundaries in the MM-diagram. The starting mode for both calculations is taken from Baker & Stolper (1993) where: ol, opx, cpx and sp are in the proportions 0.50:0.30:0.17:0.03 by weight, respectively.

In using the Stolper & Baker (1993) reaction coefficients, the following "phase-boundary" equations can be derived (see Figure 5.18):

Ol-Opx phase boundary: $y = 0.50+0.22x$,

where the intersection with the y-axis is the starting mode for ol, and the slope is the γ reaction coefficient.

Opx-Cpx phase boundary: $y = 0.80-0.15x$,

where the intersection with the y-axis is the sum of the starting modes for ol and opx, and the slope a is the sum of the reaction coefficients: $a= \gamma+\beta= -0.22+0.37= 0.15$.

Cpx-Sp phase boundary: $y = 0.97-0.88x$,

where the intersection with the y-axis is the sum of the starting modes for ol, opx and cpx, and the slope a is the sum of the reaction coefficients $a=\gamma+\beta+\alpha=-0.22+0.37+0.73=0.88$.

And similarly for the reaction coefficients given by Kinzler & Grove (1992a) (see Figure 5.18):

Ol-Opx phase boundary: $y= 0.50+0.30x$,

Opx-Cpx phase boundary: $y= 0.80-0.10x$,

Cpx-Sp phase boundary: $y= 0.97-0.92x$.

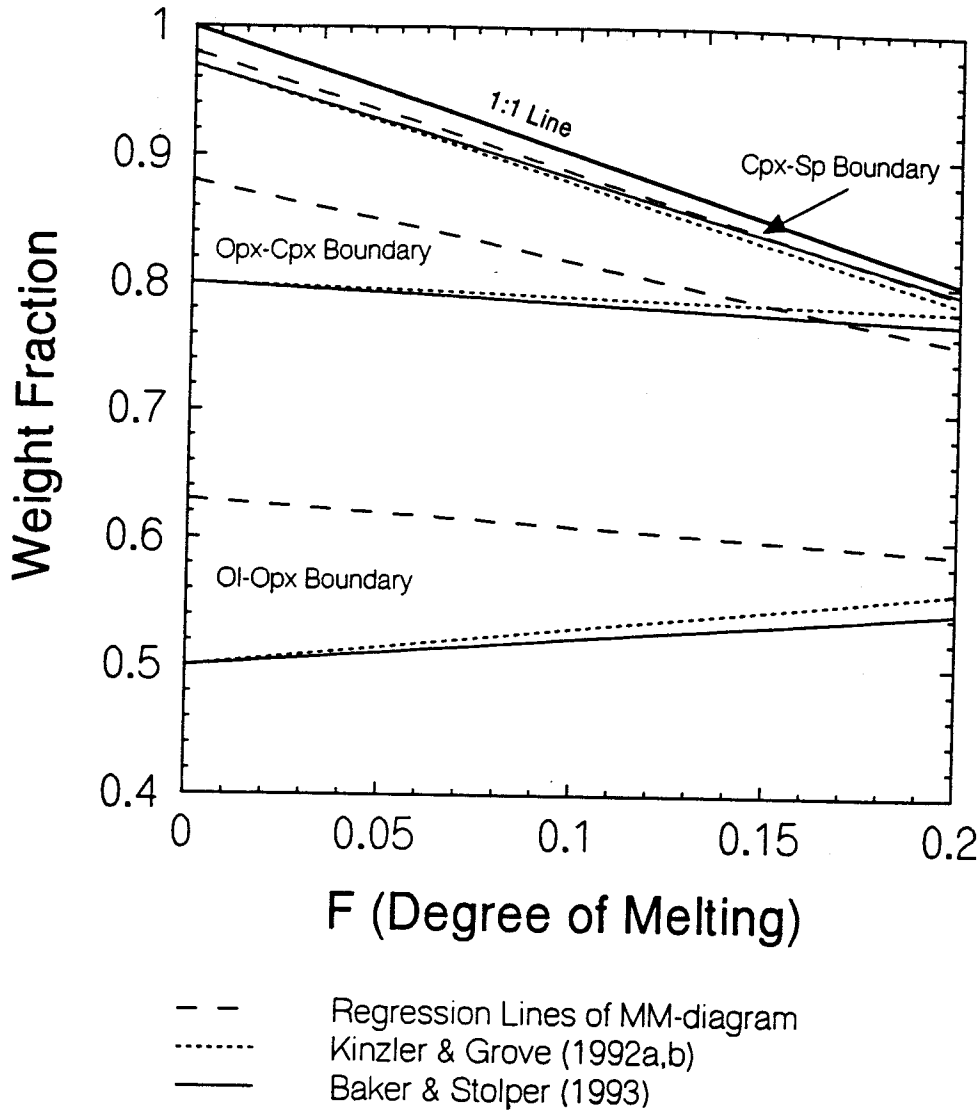

Figure 5.18: **Diagram illustrates the mantle melting reaction in the MM-diagram. Note that the experimentally-constrained reaction coefficients (Kinzler & Grove 1992a; Baker & Stolper 1993) require generation of olivine during melting.**

5.4.1 Analysis of Internal Consistency

Two of the parameters that must be specified in the fractional melting equation for calculation of F are the starting mode (X^α) and the melting mode (p^α) of each phase. Note that these values are *input* to an *analytical* calculation for each *individual* sample. As discussed in 5.x, after construction of a MM-diagram, the slopes and intercepts of the regression lines on the phase-boundaries yield estimates of the starting mineral modes and reaction coefficients, respectively. Note that these values are *output* from a *statistical* calculation for the entire *population* of samples used to "calibrate" the diagram. Thus, without introducing any circular reasoning, it is possible to test the internal consistency of the model by comparing the input/analytical/individual values with those from the output/statistical/population results and, if necessary, to iterate the model until consistency is achieved.

Table 5.2 compares the input and output parameters for six models. The first uses the starting mode (SM) and melting mode (MM) from Johnson et al. (1990, Table A2, p.2676). Although the output for the SM is fairly similar, that for the MM is significantly different, especially the Cpx/Opx ratio (< 1 for the model versus > 3 for Johnson et al. (1990)). Among other problems, it is clear that these proportions would not produce basaltic liquids. Further, the problem of olivine consumption rather than production as noted in the discussion of Figure 5.18. is confirmed by the positive sign of the MM value (0.20) from the regression equations.

The second model in Table 5.2 uses as the input starting mode the intersections with the y-axis from model ①, but the melting mode is unchanged. The resulting intercepts (output SM) match very well the input SM, so that model ② now shows good consistency for the X^α values. These values are therefore kept constant for further operations in Table 5.2.

The next set of models attempts to match the input MM values and the slopes of the regression lines. This step splits into three models, because three different melt modes are available. One is given by model ②, and two others are obtained from experimental reaction coefficients (Kinzler & Grove 1992a; Baker & Stolper 1993). A reasonably good consistency is shown by ③, and the result is illustrated in Figure 5.19. Here, olivine is generated, as indicated by the negative sign of the output MM value. However, both input and output data show small absolute values, so that this deviation might also reflect some statistical influence on the regression lines due to data dispersion along the Ol-Opx phase boundary. The match of input and output MM values is poor for both operation ④ and ⑤. While proper consumption and generation of the phases are confirmed by the signs of the output data, the match of the numerical values is rather poor. The output starting modes show again a consistently good match.

Finally, the input MM values of operation ④ are used as input in computation ⑥. In this model, both sets of output data agree very well with their corresponding input data. The resulting graph is shown in Figure 5.20.

Table 5.2:

$$D_{Ti}^{Mineral/Melt} = const.$$

①		*Ol*	*Opx*	*Cpx*	*Sp*	
Input:	*SM:*	0.55	0.25	0.18	0.02	Johnson et al. 1990
	MM:	0.10	0.20	0.68	0.02	Johnson et al. 1990
Output:	*SM:*	0.63	0.25	0.10	0.02	Intercepts y-axis
	MM:	0.20	0.41	0.33	0.06	Regression equations

②		*Ol*	*Opx*	*Cpx*	*Sp*	
Input:	*SM:*	0.63	0.25	0.10	0.02	Intercepts ①
	MM:	0.10	0.20	0.68	0.02	Johnson et al. 1990
Output:	*SM:*	0.63	0.25	0.09	0.03	
	MM:	-0.04	0.50	0.39	0.15	

③		*Ol*	*Opx*	*Cpx*	*Sp*	
Input:	*SM:*	0.63	0.25	0.10	0.02	Intercepts①
	MM:	-0.04	0.50	0.39	0.15	②
Output:	*SM:*	0.63	0.25	0.10	0.02	
	MM:	0.03	0.48	0.41	0.08	

④		*Ol*	*Opx*	*Cpx*	*Sp*	
Input:	*SM:*	0.63	0.25	0.10	0.02	Intercepts①
	MM:	-0.30	0.40	0.82	0.08	K&G
Output:	*SM:*	0.61	0.25	0.10	0.02	
	MM:	-0.14	0.54	0.50	0.08	

⑤		*Ol*	*Opx*	*Cpx*	*Sp*	
Input:	*SM:*	0.63	0.25	0.10	0.02	Intercepts①
	MM:	-0.22	0.37	0.73	0.12	B&S
Output:	*SM:*	0.62	0.25	0.11	0.02	
	MM:	-0.09	0.51	0.49	0.09	

⑥		*Ol*	*Opx*	*Cpx*	*Sp*	
Input:	*SM:*	0.63	0.25	0.10	0.02	Intercepts①
	MM:	-0.14	0.54	0.50	0.10	④
Output:	*SM:*	0.61	0.26	0.11	0.02	
	MM:	-0.18	0.55	0.53	0.10	

Where:

SM= Starting Mode X^{α}

MM= Melting Mode p^{α}

B&S= Baker & Stolper (1993)

K&G= Kinzler & Grove (1992)

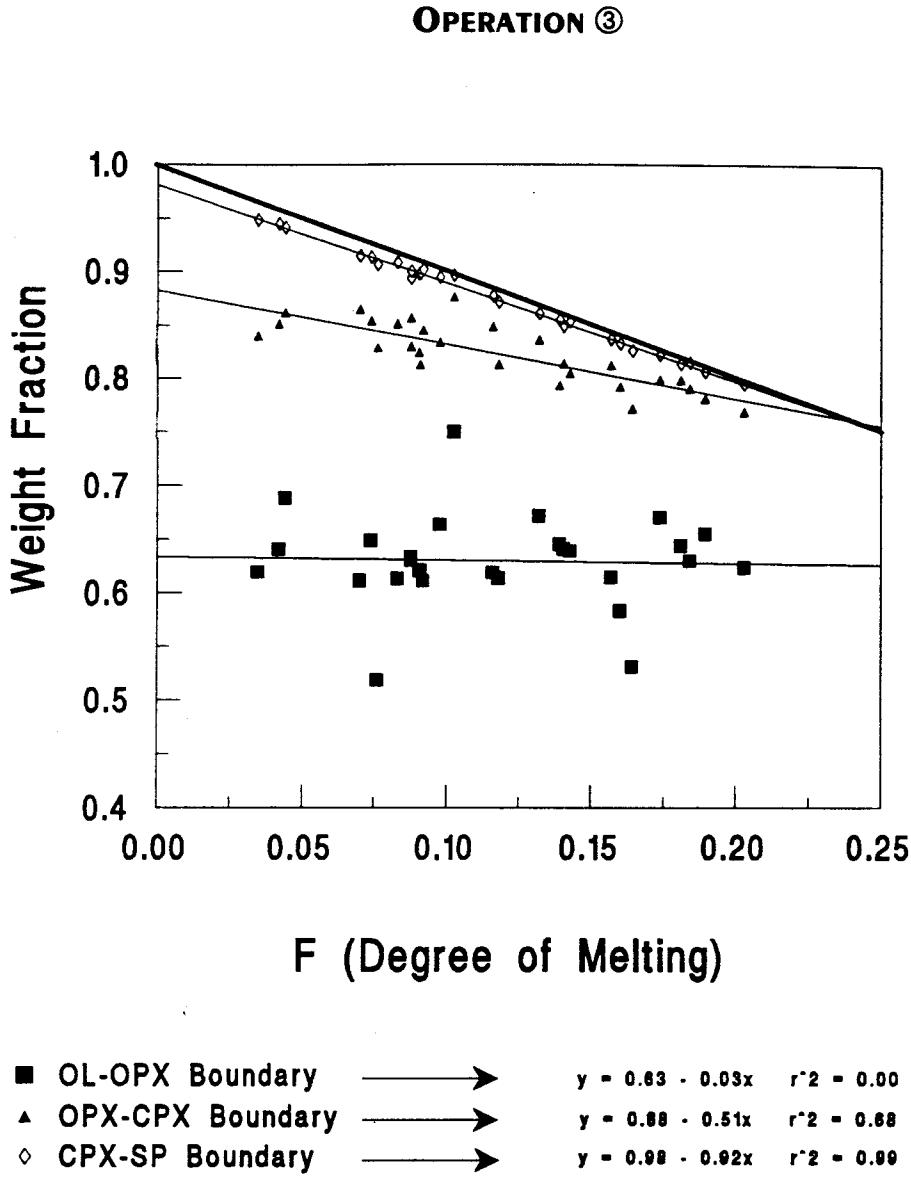

Figure 5.19: **Resulting MM-diagram of Operation ③ (compare with Table 5.2).**

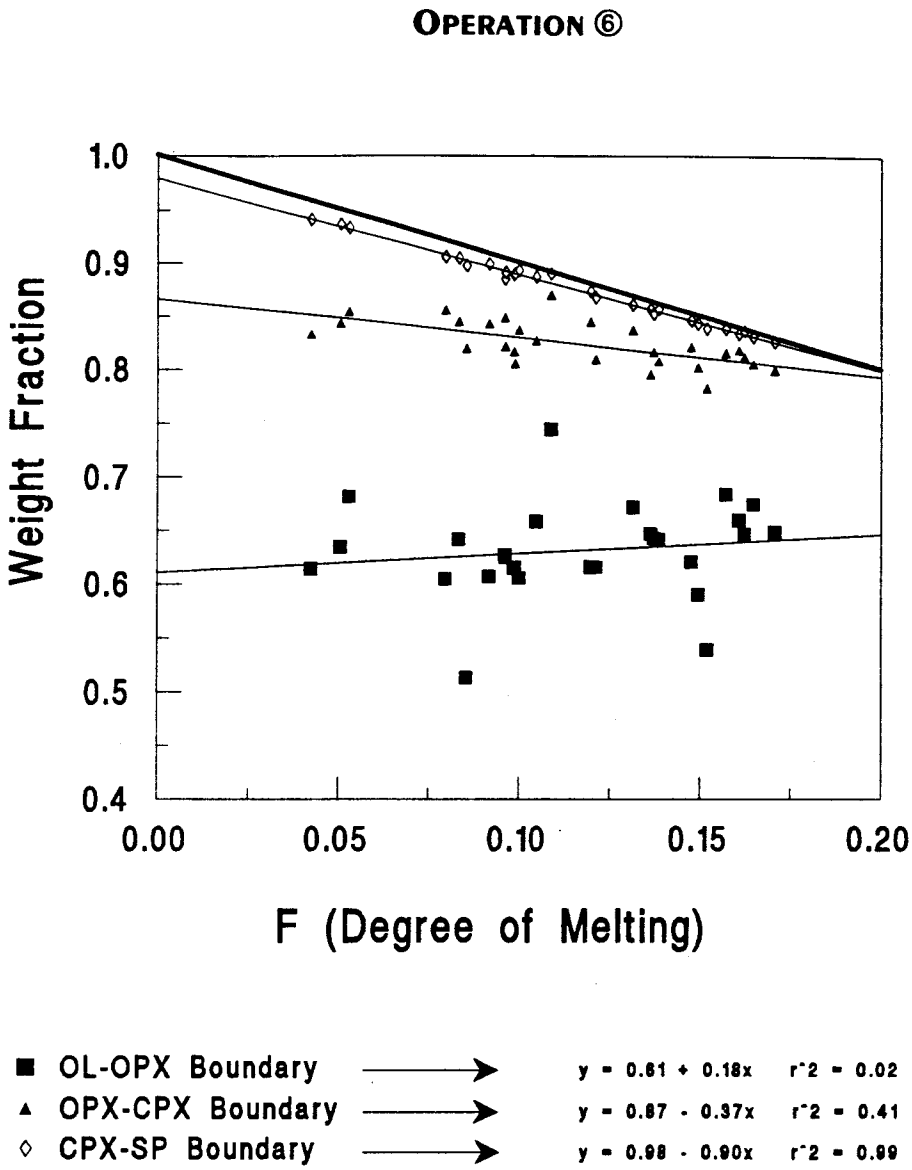

Figure 5.20: **Resulting MM-diagram of Operation ⑥ (compare with Table 5.2).**

5.4.2 Analysis of External Consistency

A comparison of experimentally determined reaction coefficients shows some serious discrepancies with the calibrated MM-Model of operation ⑥. Both experimental studies of Kinzler & Grove (1992) and Baker & Stolper (1993) suggest reaction coefficients that generate more olivine as well as consume more clinopyroxene compared to operation ⑥. Further, computations ⑥ and ③ suggest that clinopyroxene and orthopyroxene are consumed in similar proportions. This observation is not confirmed by experimental melting studies, and in that sense the results of previous section (5.4.1) are not externally consistent. The only parameters in the model that could be varied independently to address this problem are the distribution coefficients $D_{Ti}^{\alpha/Melt}$ and the starting abundance of Ti in clinopyroxene of the source rock $C_{Ti}^{0,Cpx}$. During following computations p^{α} and X^{α} values of Johnson et al. (1990) are kept constant.

In general, $D_{Ti}^{\alpha/Melt}$ affects the values for the initial bulk solid partition coefficient D_{Ti}^{0} and weighted partition coefficient of liquid P (see Appendix A). Distribution coefficients for Ol, Opx and Sp are much smaller than for Cpx and are not further considered. Changes in $D_{Ti}^{Cpx/Melt}$, however, yield more effect on P than on D_{Ti}^{0} since clinopyroxene has the greatest contribution to the liquid but a rather small modal abundance. As already discussed in 5.3.2 two extreme values of 0.2 and 0.6 for $D_{Ti}^{Cpx/Melt}$ involve shifts in the range as well as in the degree of melting. Figure 5.21 illustrates a plot of $D_{Ti}^{Cpx/Melt}$ for values from 0-1 versus the starting composition determined from the y-intercepts. Almost no change is achieved in the starting composition by changing the distribution coefficient. In contrast, reaction coefficients show more sensitivity as illustrated in Figure 5.22. With an increasing value for $D_{Ti}^{Cpx/Melt}$ the Ol consumption increases drastically while the Opx and Cpx consumption drops. Obviously, external consistency with the sign of the reaction coefficient for Ol could be achieved by decreasing $D_{Ti}^{Cpx/Melt}$ below about 0.2. Unfortunately, this would not address the large imbalance

between the MM values for Cpx and Opx (Cpx/Opx < 1 in the model but ~ 2 for Kinzler & Grove (1992a) and Baker & Stolper (1993).

The sensitivity to variations in the starting composition $C_{Ti}^{0,Cpx}$ has been discussed in 5.3.1. In changing this value shifts along the x-axis occur but will not affect the starting mode or reaction coefficients.

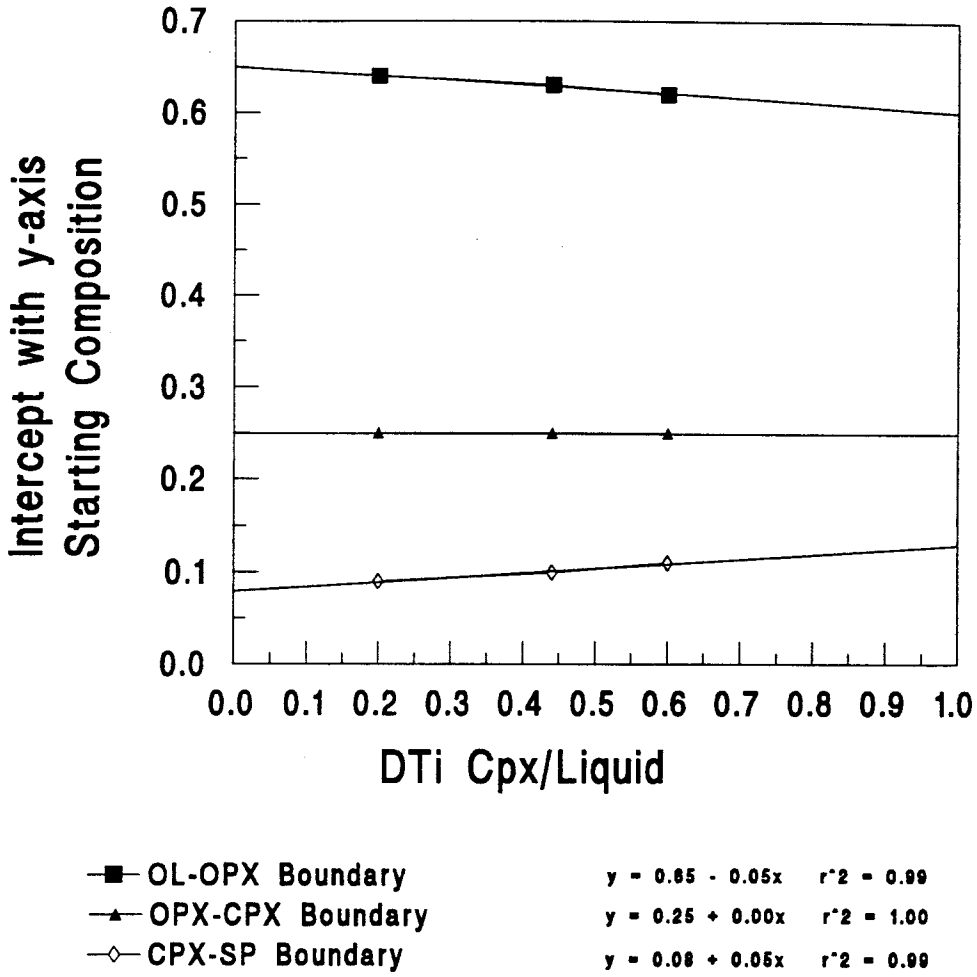

Figure 5.21: **Diagram shows the effect on starting composition in the MM-diagram by choosing different values for $D_{Ti}^{Cpx/Melt}$. All other input parameters were as specified in Operation ① in Table 5.2.**

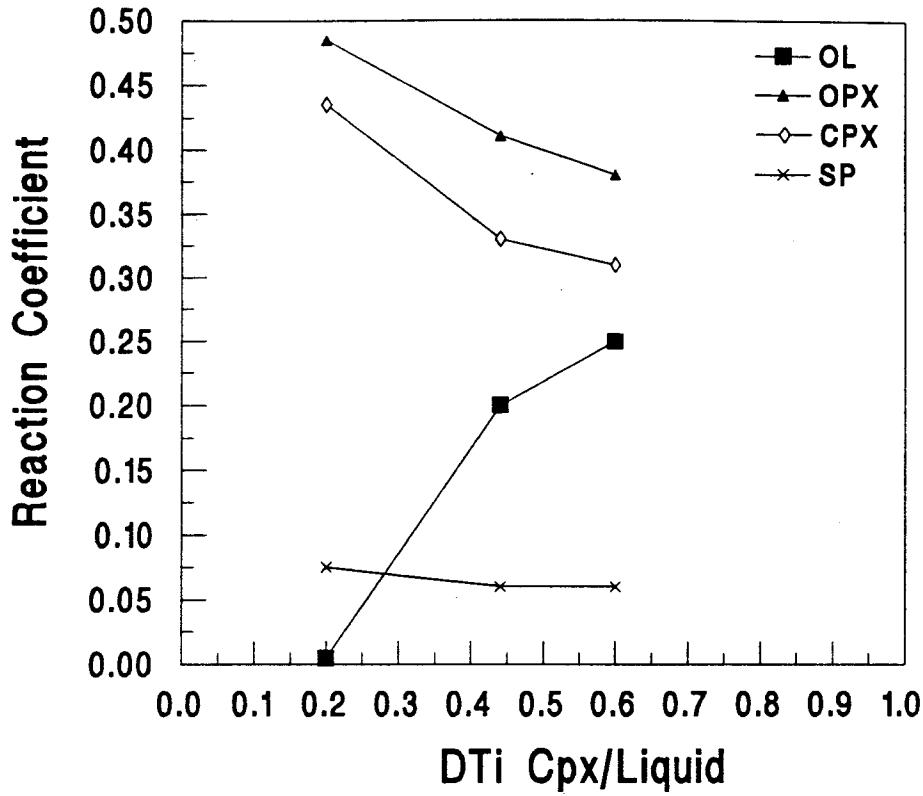

Figure 5.22: **Diagram shows the effect on reaction coefficients in the MM-diagram by choosing different values for $D_{Ti}^{Cpx/Melt}$. All other input parameters were as specified in Operation ① in Table 5.2.**

5.4.3 RESULTS

The MM-model developed in this chapter is based on the Ti distribution between Cpx and melt, and demonstrates how the modal proportions (in wt.%) of the mineral phases in a spinel lherzolite assemblage change as melting proceeds. The intersections of the regression line equations for the phase boundaries in this diagram with the y-axis reflect the starting composition prior to melting. The slope of the regression line equations can be used to derive the reaction coefficients that describe the upper mantle melting reaction.

In accordance with the MM-model a method for the calculation of F is introduced which is based solely on modal abundances. This method is applied to another abyssal peridotite population (see Appendix B), but in principle the method could apply to many peridotitic compositions and populations.

The original composition for the upper lithospheric mantle calculated from the MM-model in comparison to other suggested primitive upper mantle compositions shows a few percent mismatch in the SiO_2 and MgO contents, but is otherwise in generally good agreement.

Variations in input parameters such as starting abundance of Ti in clinopyroxene of the source rock, variations in $D_{Ti}^{Cpx/Liquid}$, melting mode proportions, and the starting mode of the mineral phases demonstrate the sensitivity of this MM-model.

In order to calibrate the MM-diagram to experimentally-derived results for upper mantle melting (Kinzler & Grove 1992a; Baker & Stolper 1993), reaction coefficients and starting abundances from those experiments which are exchangeable with the melting modes and starting mode of the fractional melting equation, respectively, are used as input values. This procedure connects results of two independent approaches. These further calculations show that a calibration with experimentally-constrained data leads to an internal consistency. The iterative values confirm the experimental observation that Ol is generated during melting (so called "odd" mantle melting reaction) as indicated by the

negative sign for the olivine reaction coefficient in operation ⑥ (Table 5.2, p. 5-36). Reaction coefficients for Opx and Cpx, however, have similar proportions; this observation does not concur with the experimentally-determined mantle melt reaction. Moreover, this result implies that the produced liquid would be too MgO rich to be related to mid-ocean ridge basalts.

A satisfactory link between the trace-element fractional melting model based on ion probe data of clinopyroxenes in abyssal peridotites (Johnson et al. 1990) and experimental petrology on upper mantle melting can therefore not be obtained. Although the melting has presumably occurred under fractional rather than equilibrium conditions (Johnson et al. 1990) in order to generate the very low abundances of Ti, Zr, and REE in clinopyroxene for the least-depleted samples, the details with respect to melt separation and migration beneath the mid-ocean ridges are not yet well constrained.

Alternatively, it is possible that the chemical pattern of abyssal peridotites does not necessarily reflect a single-stage depletion process. Elthon (1992) showed that the range of Na_2O abundance in abyssal peridotites is too high to be generated by fractional melting of a likely primitive upper mantle composition, and suggested therefore that the depleted mantle became refertilized with up to 10% depleted basaltic liquids *after* fractional melting has occurred. In his opinion refertilization may be a dominantly controlling process for chemical trends in abyssal peridotites. (However, the distinct Ti-Zr fractionation trend of clinopyroxenes (Figure 1.2) would then, as a consequence to Elthon's theory, require that the secondary enrichment process had a quite uniform nature in order to maintain the Ti/Zr trend after depletion has occurred.)

The lack of detailed understanding of the process(es) of melt separation and percolation within the melting column, and their effects on the composition of abyssal peridotites might be among additional uncertainties that need to be addressed before a model can be constructed that achieves both internal and external consistency.

Table 5.3: **Modal analyses of abyssal peridotites. Data are from Johnson et al.(1990).**

SAMPLE	OLIVINE	ORTHOPYROXENE	CLINOPYROXENE	SPINEL
Vulc5:41-31	71.8	18.1	8.9	1.2
Vulc5:41-15	63.9	22.7	2.0	1.4
Vulc5:41-30	65.7	27.2	5.8	1.3
Vulc5:41-33	68.1	21.0	9.9	1.0
Vulc5:41-45	68.1	22.3	8.5	1.1
Vulc5:34-56	74.8	17.1	7.5	0.6
Vulc5:35-1	74.4	19.2	6.0	0.4
Vulc5:35-19	70.0	22.1	6.9	1.1
Vulc5:35-22	77.4	18.9	3.0	0.7
Vulc5:35-30	74.7	20.1	4.3	1.0
Vulc5:37-3	82.7	13.9	2.4	0.1
All107:40-6	78.2	18.1	3.4	0.1
All107:40-11	81.1	15.5	2.9	0.4
All107:40-13	78.7	18.8	2.0	0.4
IO11/76:56-57	69.6	24.5	4.3	1.7
IO11/76:56-10	73.4	8.70	7.2	0.7
IO11/76:56-54	69.0	21.7	8.2	1.1
IO11/76:58-34	70.0	25.9	3.5	0.6
PS 86:6-37	66.6	21.9	10.4	1.1
Prot5:19-2	70.0	22.0	7.0	1.0
Prot5:19-2	72.8	23.4	3.2	0.6
Prot5:29-26	63.5	28.6	7.0	0.9
Prot5:38-1	69.4	24.8	5.1	0.7
RC27-9:6-3	67.1	25.6	6.6	0.6
RC27-9:6-8	66.6	25.8	6.6	0.8
RC27-9:25-14	56.1	33.5	9.0	1.5
PS 86:6-37	66.6	21.9	10.4	1.1
Prot5:19-2	70.0	22.0	7.0	1.0
Prot5:19-2	72.8	23.4	3.2	0.6
Prot5:29-26	63.5	28.6	7.0	0.9
Prot5:38-1	69.4	24.8	5.1	0.7
RC27-9:6-3	67.1	25.6	6.6	0.6
RC27-9:6-8	66.6	25.8	6.6	0.8
RC27-9:25-14	56.1	33.5	9.0	1.5

Table 5.4.: **Microprobe analyses of abyssal peridotites. Data are from Johnson et al. (1990) and Dick (1989).**

SAMPLE	PHASE	SiO_2	TiO_2	Al_2O_3	FeO	MnO	MgO	CaO	Na_2O	K_2O	Cr_2O_3	NiO	SUM
Vulc5:41-30	OL	40.66	0	0	9.39	0.18	49.66	0.04	0	0	0	0.34	100.27
	OPX	53.66	0.1	5.35	5.9	0.12	30.75	2.69	0.06	0.03	0.67	0	99.33
	CPX	50.66	0.31	5.68	2.73	0.06	15.76	22.57	0.45	0	0.99	0	99.21
	SP	0	0	49.68	13.42	0.04	19.42	0	0	0	16.19	0.2	98.95
	BULK	44.05	0.03	2.55	8.22	0.15	42.49	1.66	0.02	0.009	0.5	0.23	99.9
Vulc5:41-33	OL	40.63	0	0	9.4	0.2	49.74	0.03	0	0	0	0.3	100.3
	OPX	52.74	0.09	5.48	6.07	0.04	30.06	2.86	0.05	0.01	0.38	0	97.78
	CPX	50.18	0.23	6.83	3.22	0.03	17.57	19.08	0.45	0	1.58	0	99.17
	SP	0	0	51.11	12.47	0.06	19.59	0	0	0	15.43	0.18	98.84
	BULK	43.59	0.04	2.41	8.16	0.15	42.22	2.41	0.053	0.002	0.413	0.21	99.66
Vulc5:41-45	OL	40.56	0	0	10	0.24	49.33	0.04	0	0	0	0.26	100.43
	OPX	53.74	0.11	5.56	6.38	0.12	30.45	2.02	0.05	0.04	0.65	0	99.12
	CPX	50.36	0.24	6.37	3.49	0.07	17.42	20.51	0.41	0.02	1.11	0	100.00
	SP	0	0	51.27	13.48	0.05	19.06	0	0	0	14.75	0.18	98.61
	BULK	43.71	0.044	2.48	8.72	0.2	42.14	2.11	0.04	0.01	0.44	0.18	100.07
Vulc5:35-1	OL	40.97	0	0	9.37	0.11	49.33	0.04	0	0	0	0.32	100.14
	OPX	54.21	0.02	4.03	6.09	0.25	31.36	1.93	0.05	0.02	0.64	0	98.6
	CPX	51.24	0.07	5.32	3.54	0.08	17.86	19.84	0.35	0.03	1.28	0	99.61
	SP	0	0	44.19	14.66	0.09	17.98	0	0	0	22.43	0.19	99.54
	BULK	43.87	0.001	1.32	8.44	0.14	43.93	1.52	0.03	0.006	0.32	0.24	99.82
Vulc5:35-22	OL	40.75	0	0	9	0.16	49.42	0.02	0	0	0	0.34	99.69
	OPX	55.09	0	3.74	5.1	0.15	32.77	2.36	0.03	0	0.6	0	99.84
	CPX	51.34	0.1	4.56	2.98	0.1	18.69	20.02	0.24	0	1.19	0	99.22
	SP	0	0.08	42.99	15.72	0.11	17.32	0	0	0	24.06	0.25	100.53
	BULK	43.39	0.004	1.22	8.16	0.16	45.13	1.02	0.01	0	0.37	0.51	99.97

Table 5.4 continued:

SAMPLE	PHASE	SiO_2	TiO_2	Al_2O_3	FeO	MnO	MgO	CaO	Na_2O	K_2O	Cr_2O_3	NiO	SUM
Vulc5:35-30	OL	40.79	0	0	8.77	0.14	49.91	0.03	0	0	0	0.34	99.98
	OPX	54.76	0	4.37	5.24	0.14	32.34	2.6	0.01	0.01	0.51	0	99.98
	CPX	50.38	0.04	5.05	4.09	0.05	21.56	16.55	0.11	0.02	0.9	0	99.2
	SP	0	0.14	46.32	13.54	0.11	18.79	0	0	0	20.54	0.1	99.54
	BULK	43.47	0.003	1.66	7.93	0.14	44.86	1.21	0.006	0.003	0.4	0.26	99.94
All107:40-6	OL	40.36	0	0	8.98	0.12	49.1	0.04	0	0	0	0.29	98.89
	OPX	55.19	0	3.82	5.58	0.16	33.21	2.23	0	0	0.66	0	100.85
	CPX	51.52	0	4.7	3.01	0.11	18.66	21.11	0.05	0.02	1.2	0	100.38
	SP	0	0.04	38.66	14.54	0.1	17.39	0	0	0	29.09	0.22	100.04
	BULK	43.25	0	0.99	8.19	0.13	45.13	1.11	0.002	0	0.27	0.23	99.3
IO11/76:56-57	OL	39.84	0	0	9.52	0.13	48.99	0.02	0	0	0	0.27	98.77
	OPX	54.21	0.1	5.21	6.03	0.13	31.2	1.91	0.04	0.02	0.73	0	99.58
	CPX	50.99	0.28	6.46	2.67	0.07	17.01	20.33	0.77	0.01	1.14	0	99.73
	SP	0	0.03	53.18	11.11	0.06	19.63	0	0	0	14.58	0.3	98.89
	BULK	43.25	0.04	2.31	8.41	0.13	42.98	1.31	0.04	0.005	0.44	0.19	99.11
IO11/76:56-10	OL	40.42	0	0	9.24	0.26	49.22	0.01	0	0	0	0.4	99.55
	OPX	54.27	0.07	5.28	5.54	0.13	31.33	1.88	0.1	0.01	0.34	0	98.95
	CPX	51.26	0.18	6.79	2.74	0.06	16.86	19.73	0.79	0	1.01	0	99.42
	SP	0	0.14	52.21	10.65	0.04	20.32	0	0	0	14.94	0.08	98.38
	BULK	43.41	0.03	1.87	8.12	0.22	43.43	1.7	0.07	0.002	0.26	0.3	99.41
IO11/76:58-34	OL	40.4	0	0	9.49	0.08	49.09	0.02	0	0	0	0.26	99.34
	OPX	54.6	0.05	5.21	5.74	0.06	31.71	1.95	0.08	0	0.41	0	99.81
	CPX	50.34	0.09	6.48	3.14	0.11	17.38	19.35	0.71	0.01	1.46	0	99.27
	SP	0	0	50.79	12.55	0.04	19.22	0	0	0	16.14	0.34	99.08
	BULK	44.1	0.02	1.96	8.33	0.075	43.31	1.16	0.044	0	0.28	0.19	99.47

REFERENCES

Allegre C.J. & Hart S.R., (eds.), *Trace elements in igneous petrology*, Developments in Petrology 5, Elsevier Science Publisher B.V., Amsterdam, 1978, 272 pp.

Anderson D.L., 1990, Geophysics of the continental mantle: an historical perspective, in: *Continental mantle*, Menzies M.A. (ed.), Oxford Science Publication, 1-30.

Baker M.B. & Stolper E.M., 1993, Determining the composition on high-pressure mantle melts using diamond aggregates, *Geochim. Cosmochim. Acta*, (in press).

Baldridge W.S., 1979, Mafic and ultramafic inclusion suites from the Rio Grande Rift (New Mexico) and their bearing on the composition and thermal state of the lithosphere, *J. Volcan. Geothermal. Res. 6*, 319-351.

Best M.G., 1974, Contrasting types of chromium-spinel peridotite xenoliths in basanitic lavas, Western Grand Canyon, Arizona, *Earth Planet. Sci. Lett 23*, 229-237.

Bonatti E. & Michael P.J., 1989, Mantle peridotites from continental rifts to ocean basins to subduction zones, *Earth Planet. Sci. Lett. 92*, 297-311.

Cimmino F., Pedemonte G.M. & Piccardo G.B., 1976, Petrology of ultramafic xenoliths in fissure alkali basalts of the Assab regions (Afar, Ethiopia), *Soc. Ital. Mineral. Petrol. 32*, 561-577.

Dawson J.B., 1984, Contrasting types of upper mantle metasomatism?, in: *Kimberlites-II: The mantle and mantle-crust relationship*, Kornprobst J (ed.), Elsevier Science Publishers B.V, Amsterdam, 289-294.

Dick H.J.B., Fisher R.L. & Bryan W.B., 1984, Mineralogic variability of the uppermost mantle along mid-ocean ridges, *Earth Planet. Sci. Lett. 69*, 88-106.

Dick H.J.B. & Fisher R.L., 1984, Mineralogic studies of the residues of mantle melting: abyssal and alpine-type peridotites, in: *Kimberlites II: The mantle and mantle-crust relationships*, Kornprobst J (ed.), Elsevier Science Publishers B.V., Amsterdam, 295-308.

Dick H.J.B., 1989, Abyssal peridotites, very slow spreading ridges and ocean ridge magmatism, in: Magmatism on the ocean basins, *Geol. Soc. Spec. Publ. No.42*, 71-105.

Elthon D., 1992, Chemical trends in abyssal peridotites: refertilization of depleted suboceanic mantle, *J. Geophys. Res. 97*, 9015-9025.

Frechen J., 1963, Kristallisation, Mineralbestand, Mineralchemismus und Förderfolge der Mafite vom Dreiser Weiher in der Eifel, *Neues Jahrb. Mineral. Geol. Paleontol. Monatsh., Abt 1.*, 205-255.

Frey F.A. & Green D.H., 1974, The mineralogy, geochemistry and origin of lherzolite inclusions from Victorian basanites, *Geochim. Cosmochim. Acta 38*, 1023-1059.

Frey F.A. & Prinz M., 1978, Ultramafic inclusions from San Carlos, Arizona: petrologic and geochemical data bearing on their petrogenesis, *Earth Planet. Sci. Lett. 38*, 129-176.

Galer S.J.G. & O'Nions R.K., 1989, Chemical and isotopic studies of ultramafic inclusions from the San Carlos Volcanic Field, Arizona: A bearing on their petrogenesis, *J. Petrol. 30*, 1033-1064.

Gallahan W.E & Nielsen R.L., 1992, The partitioning of Sc, Y and the rare-earth elements between high Ca-pyroxene and natural mafic to intermediate lavas at 1 atmosphere, *Geochim. Cosmochim. Acta 56*, 2387-2404.

Gast P.W., 1968, Trace element fractionation and the origin of tholeiitic and alkaline magma types, *Geochim. Cosmochim. Acta 32*, 1057-1068.

Hart S. & Zindler A., 1986, In search of a bulk-earth composition, *Chem. Geol. 57*, 247-267.

Harte B., 1976, Rock nomenclature with particular relation to deformation and recrystallisation textures in olivine-bearing xenoliths, *J. Geol. 85*, 279-288.

Hawkesworth C.J. & Norry M.J., (eds.), *Continental basalts and mantle xenoliths*, Shiva Geological Series, 1983, 272 pp.

Irving A.J., 1980, Petrology and geochemistry of composite ultramafic xenoliths in alkalic basalts and implications for magmatic processes within the mantle, *Amer. J. Sci. 280-A*, p.289-426.

Irving A.J. & Frey F.A., 1984, Trace element abundances in megacrysts and their host basalts: constraints on partition coefficients and megacryst genesis, *Geochim. Cosmochim. Acta 48*, 1201-1221.

Johnson K.T.M, 1990, Trace element geochemistry of oceanic peridotites and silicate melt inclusions: Implications for mantle melting and ocean-ridge magmagenesis, Ph.D. thesis, Mass. Inst. of Technol./Woods Hole Oceanogr. Inst., Woods Hole, Mass.

Johnson K.T.M., Dick H.J.B & Shimizu N., 1990, Melting in oceanic upper mantle: an ion microprobe study of diopsides in abyssal peridotites, *J. Geophys. Res. 95*, 2 661-2 678.

Johnson K.T.M & Dick H.J.B., 1992, Open system melting and temporal and spatial variation of peridotite and basalt at the Atlantis II fracture zone, *J. Geophys. Res. 97*, 9 219-9 241.

Jagoutz E., Palme H., Baddenhausen H., Blum K., Cendales M., Dreibus G., Spettel B., Lorenz V. & Wänke H., 1979, The abundance of major, minor and trace elements in the earth's mantle as derived from primitive ultramafic nodules, *Proc. Lunar Planet. Sci. Conf. 10th*, 2 031-2 050.

Jaques A.L. & Green D.H., 1980, Anhydrous melting of peridotite at 0-15 Kb pressure and the genesis of tholeiitic basalts, *Contrib. Mineral. Petrol. 73*, 287-310.

Kinzler R.J. & Grove T.L., 1992a, Primary magmas of mid-ocean ridge basalts 1: experiments and methods, *J. Geophys. Res. 97*, 6 885-6 906.

Kinzler R.J. & Grove T.L., 1992b, Primary magmas of mid-ocean ridge basalts 2: applications, *J. Geophys. Res. 97*, 6 907-6 926.

Kinzler R.J. & Grove T.L., 1993, Corrections, clarifications, and further discussion of the primary magmas of mid-ocean ridge basalts, 1 experiments and methods, and 2 applications, *J. Geophys. Res.*, in press.

Kornprobst J., (ed.), *Kimberlites II: the mantle and crust-mantle relationships*, Developments in Petrology 11B, Elsevier Science Publisher B.V., Amsterdam, 1984, 392 pp.

Liang Y. & Elthon D., 1990, Geochemistry and petrology of spinel lherzolite xenoliths from Xalapasco de La Joya, San Luis Potosi, Mexico: Partial melting and mantle metasomatism, *J. Geophys. Res. 95*, 15 859-15 877.

Lipin B.R. & McKay G.A., (eds.), *Geochemistry and mineralogy of rare earth elements*, Mineral. Soc. Amer. Rev. Mineral. 21, 1989, 348 pp.

Maaløe S. & Aoki K.-i., 1977, The major element composition of the upper mantle estimated from the composition of lherzolites, *Contrib. Mineral. Petrol. 63*, 161-173.

Marsh B.D., 1981, On the crystallinity, probability of occurrence, and rheology of lava and magma, *Contrib. Mineral. Petrol. 78*, 85-98.

McDonough W.F & Frey F.A., 1989, Rare earth elements in upper mantle rocks, in: *Geochemistry and mineralogy of rare earth elements*. Lipin B.R. & McKay G.A. (eds.), Mineral. Soc. Amer. Rev. Miner. 21, 99-145.

McDonough W.F., 1990, Constraints on the composition of the continental lithospheric mantle, *Earth Planet. Sci. Lett. 101*, 1-18.

Menzies M.A., (ed.), *Continental mantle*, Oxford Science Publication, 1990, 184 pp.

Mercier J-C.C. & Nicolas A., 1974, Textures and fabrics of upper-mantle peridotites as illustrated by xenoliths from basalts, *J. Petrol. 16*, 454-487.

Michael P.J. & Bonatti E., 1985, Peridotite composition from the North Atlantic: regional and tectonic variations and implications for partial melting, *Earth Planet. Sci. Lett. 73*, 91-104.

Mysen B.O. & Kushiro I., 1977, Compositional variations of coexisting phases with degree of melting of peridotite in the upper mantle, *Amer. Mineral. 62*, 843-865.

Nielsen R.L., Gallahan W.E. & Newberger F., 1992, Experimentally determined mineral-melt partitioning coefficients for Sc, Y and REE for olivine, orthopyroxene, pigeonite, magnetite and ilmenite, *Contrib. Miner. Soc. 110*. 488-499.

Nixon P.H., (ed.), *Mantle xenoliths*, Wiley & Sons, New York, 1987, 844 pp.

O'Reilly S.Y., Griffin W.L. & Ryan C.G., 1991, Residence of trace elements in metasomatized spinel lherzolite xenolith: a proton-microprobe study, *Contrib. Mineral. Petrol. 109*, 98-113.

Roden M.F. & Murthy V.R., 1985, Mantle metasomatism, *Ann. Rev. Earth Planet. Sci. 13*, 269-296.

Roden M.F & Shimizu N., 1993, Ion microprobe analyses bearing on the composition of the upper mantle beneath the Basin and Range and Colorado plateau provinces, *J. Geophys. Res.* (in press).

Ringwood A.E., (ed.), *Origin of the earth and moon*, Springer Verlag N.Y, 1979, 295pp.

Sachtleben T. & Seck H.A., 1981, Chemical control of Al-solubility in orthopyroxene and its implications on pyroxene geothermometry, *Contrib. Mineral. Petrol.* 78, 157-165.

Schilling J.G. & Winchester J.W., 1967, Rare-earth fractionation and magmatic processes, in: *Mantles of the Earth and terrestrial planets*, Runcorn (ed.), Wiley-Interscience, 267-283.

Schmincke H.U., 1967, Stratigraphy and petrography of four upper Yakima basalt flows in south-central Washington, *Geol. Soc. Am. Bull 78*, 1385-1422.

Schneider M.E. & Eggler D.H., 1986, Fluids in equilibrium with peridotite mineral: implications for mantle metasomatism, *Geochim. Cosmochim. Acta 50*, 711-724.

Shaw D.M., 1970, Trace element fractionation during anatexis, *Geochim. Cosmochim. Acta 34*, 237-243.

Stolper E., 1980, A phase diagram for mid-ocean ridge basalts: Preliminary results and implications for petrogenesis, *Contrib. Mineral. Petrol. 74*, 13-27.

Stormer J.C., Gomes C.B. & Torquato J.R.F., 1975, Spinel lherzolite nodules in basanite lavas from Asuncion, Paraguay, *Revista Brasil. Geosci. 5*, 176-185.

Stosch H.-G. & Seck H.A., 1980, Geochemistry and mineralogy of two spinel peridotite suites from Dreiser Weiher, West Germany, *Geochim. Cosmochim. Acta 44*, 457-470.

Stosch H.-G., 1982, Rare earth element partitioning between minerals from anhydrous spinel peridotite xenoliths, *Geochim. Cosmochim. Acta 46*, 793-811.

Stosch H.-G. & Lugmair G.W., 1986, Trace element and Sr and Nd isotope geochemistry of peridotite xenoliths from the Eifel (West Germany) and their bearing on the evolution of the subcontinental lithosphere, *Earth Planet. Sci. Lett. 80*, 281-298.

Swanson D.A., 1967, Yakima basalt of the Tieton River area, south-central Washington, *Geol. Soc. Am. Bull. 78*, 1 077-1 110.

Takahashi E., 1986, Melting of a dry peridotite KLB-1 up to 14 GPa: Implications on the origin of peridotitic upper mantle, *J. Geophys. Res. 91*, .9 367-9 382.

Wilshire H.G. & Shervais J.W., 1975, Al-augite and Cr-diopside ultramafic xenoliths in basaltic rocks from Western United States: Structural and textural relationship, *Phys. Cem. Earth 9*, 257-272.

Wilshire H.G., Meyer C.E., Nakata J.K., Calk L.C., Shervais J.W., Nielson J.E & Schwarzman E.C., 1988, Mafic and ultramafic xenoliths from volcanic rocks of the Western United States, *U.S.G.S. Prof. Pap. 1443*, 180 pp.

Wilson M., (ed.), *Igneous petrogenesis-a global tectonic approach*, Unwin Hyman, London, 1989, 466p.

Wood & Fraser, 1976, Behavior of trace elements components, in: *Elementary thermodynamics for geologists*, Oxford Univ. Press, 195-225.

Zindler A. & Jagoutz E., 1987, Mantle cryptology, *Geochim. Cosmochim. Acta 52*, 319-333.

APPENDIX A:

Nomenclature and Abbreviations:

ol = olivine
opx = orthopyroxene
cpx = clinopyroxene
sp = spinel

HFSE = High field strength elements, elements with valency greater than 2, e.g. Ti^{4+}, Zr^{4+}.

LILE = Large ion lithophile elements, elements of large ionic radius and with valencies of 1 or 2 (e.g. Rb^{1+}, Ba^{2+})

REE = Rare earth elements, incompatibility is decreasing relative to increasing atomic number; their chemical behavior is very similar due to their valence electron configuration; ionic radius increases with increasing atomic number (≅ lanthanide contraction).

LREE = Light rare earth elements (La, Ce, Pr, Nd)
MREE = Middle rare earth elements (Sm, Eu, Gd, Tb, Dy)
HREE = Heavy rare earth elements (Ho, Er, Tm, Yb, Lu)

D_i $= \sum D_i^a X^a = (D_i^0 - PF)/(1-F)$
bulk solid partition coefficient of element *i* at F percent meting

D_i^o $= \sum D_i^a X^{0,a}$ initial bulk solid partition coefficient of element *i*

P $= \sum D_i^a p^{0,a}$ weighted partition coefficient of liquid

F = weight fraction of melt relative to original parent

p^{α} = proportion of mineral phase α entering the liquid

$X^{0,\alpha}$ = initial weight fraction of mineral phase α

C_i^s = concentration of element *i* in bulk solid

C_i^L = concentration of element *i* in the liquid

C_i^0 = concentration of *i* in original bulk solid

APPENDIX B:

Calculation of F for Samples from the Atlantis II Fracture Zone

From the recent paper of Johnson & Dick (1992) additional modal data for abyssal peridotites from nine dredge hauls from the Atlantis II fracture zone are available. In the following, F is calculated for 24 samples according to the method introduced in paragraph 5.2.1.

Again, all samples are plagioclase-free peridotites. The samples show a wide range of trace-elements contents that is close to the overall range found for the SW Indian ridge (Johnson et al. 1990; Johnson & Dick 1992). As pointed out by Johnson & Dick (1992), a significant break occurs in the peridotitic composition as well as in the modal mineralogy across the transform fault (East wall → West wall). This observation suggests that the transform fault acts as a boundary for different melting regimes and/or initial mantle compositions. Modal compositions of the Atlantis II peridotites cover a large range, where samples from the West wall are in general more olivine-rich than those from the East wall. They also exhibit a greater depletion in incompatible trace-elements (Johnson & Dick 1992). These observations might suggest that samples from the West wall have experienced a greater degree of melting.

Figure A-1 summarizes calculations for F. Assuming a similar source rock composition, results confirm that samples from the west wall are products of higher degrees of melting.

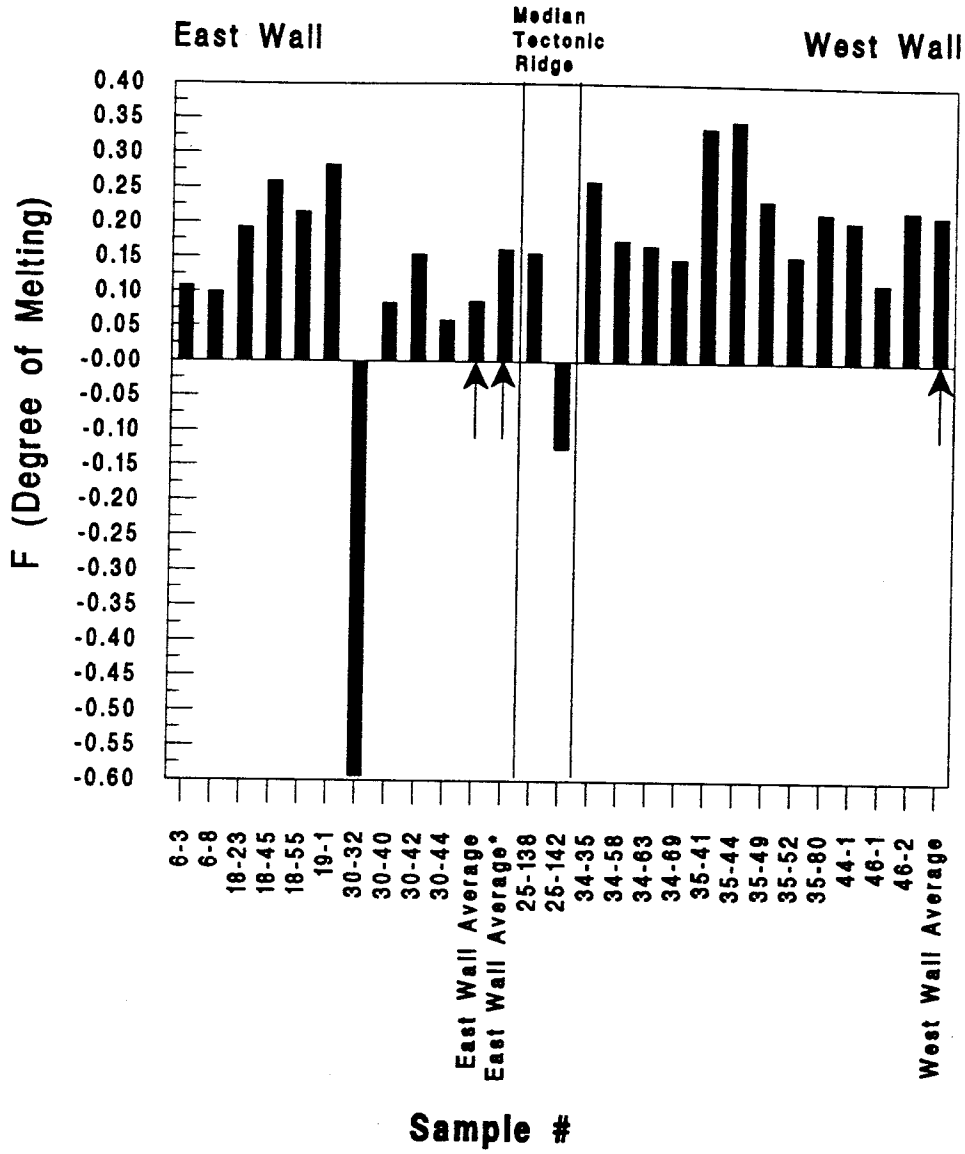

Figure A-1: **Abyssal peridotites indicated by sample numbers versus the calculated degree of melting. Sample # 30:32 shows an unusual high mode of CPX (13.9 wt. %), and sample # 25:142 has a low mode of OL (56.3 wt. %) as well as a high OPX mode (33.6 wt.%). These "extreme" fertile values result in negative degrees of melting.**

Sample ID: RC27-9:6-3

Enter the volume fractions of the four phases:

$VOL := 0.671 \quad VOPX := 0.256 \quad VCPX := 0.066 \quad VSP := 0.006$

Convert to mass fractions, assuming ρ_{rock} = 3.3 g/cm^3 and others as shown:

$$OL := \frac{3.3}{3.3} \cdot VOL \quad OPX := \frac{3.3}{3.3} \cdot VOPX \quad CPX := \frac{3.0}{3.3} \cdot VCPX \quad SP := \frac{4.1}{3.3} \cdot VSP$$

$SUM := OL + OPX + CPX + SP \quad SUM = 0.994$

$$OL := \frac{OL}{SUM} \quad OPX := \frac{OPX}{SUM} \quad CPX := \frac{CPX}{SUM} \quad SP := \frac{SP}{SUM}$$

$OL = 0.675 \quad OPX = 0.257 \quad CPX = 0.06 \quad SP = 0.007$

Calculate coefficients for left-hand terms in three best-fit linear equations:

$a_1 := 0.0911 - 0.4621 \cdot OL \quad a_2 := 0.1895 - 0.3098 \cdot (OL + OPX)$

$a_3 := 0.2873 - 0.3061 \cdot (OL + OPX + CPX)$

Calculate right-hand terms for equations:

$b_1 := 0.2906 - 0.4621 \cdot OL \quad b_2 := 0.2725 - 0.3098 \cdot (OL + OPX)$

$b_3 := 0.3002 - 0.3061 \cdot (OL + OPX + CPX)$

Define column vectors A and B for A*F=B:

$$A := \begin{bmatrix} a_1 \\ a_2 \\ a_3 \end{bmatrix} \quad B := \begin{bmatrix} b_1 \\ b_2 \\ b_3 \end{bmatrix}$$

Calculate least-squares solution for F:

$F := (A^T \cdot A)^{-1} \cdot A^T \cdot B \quad F = 0.108$

Sample ID: RC27-9:6-8

Enter the volume fractions of the four phases:

$VOL := 0.666 \qquad VOPX := 0.258 \qquad VCPX := 0.066 \qquad VSP := 0.008$

Convert to mass fractions, assuming ρ_{rock} = 3.3 g/cm^3 and others as shown:

$$OL := \frac{3.3}{3.3} \cdot VOL \qquad OPX := \frac{3.3}{3.3} \cdot VOPX \qquad CPX := \frac{3.0}{3.3} \cdot VCPX \qquad SP := \frac{4.1}{3.3} \cdot VSP$$

$SUM := OL + OPX + CPX + SP \qquad SUM = 0.994$

$$OL := \frac{OL}{SUM} \qquad OPX := \frac{OPX}{SUM} \qquad CPX := \frac{CPX}{SUM} \qquad SP := \frac{SP}{SUM}$$

$OL = 0.67 \qquad OPX = 0.26 \qquad CPX = 0.06 \qquad SP = 0.01$

Calculate coefficients for left-hand terms in three best-fit linear equations:

$a_1 := 0.0911 - 0.4621 \cdot OL \qquad a_2 := 0.1895 - 0.3098 \cdot (OL + OPX)$

$a_3 := 0.2873 - 0.3061 \cdot (OL + OPX + CPX)$

Calculate right-hand terms for equations:

$b_1 := 0.2906 - 0.4621 \cdot OL \qquad b_2 := 0.2725 - 0.3098 \cdot (OL + OPX)$

$b_3 := 0.3002 - 0.3061 \cdot (OL + OPX + CPX)$

Define column vectors A and B for A*F=B:

$$A := \begin{bmatrix} a_1 \\ a_2 \\ a_3 \end{bmatrix} \qquad B := \begin{bmatrix} b_1 \\ b_2 \\ b_3 \end{bmatrix}$$

Calculate least-squares solution for F:

$F := \left(A^T \cdot A\right)^{-1} \cdot A^T \cdot B \qquad F = 0.099$

Sample ID: RC27-9:18-23

Enter the volume fractions of the four phases:

$VOL := 0.734 \quad VOPX := 0.186 \quad VCPX := 0.072 \quad VSP := 0.009$

Convert to mass fractions, assuming ρ_{rock} = 3.3 g/cm^3 and others as shown:

$$OL := \frac{3.3}{3.3} \cdot VOL \quad OPX := \frac{3.3}{3.3} \cdot VOPX \quad CPX := \frac{3.0}{3.3} \cdot VCPX \quad SP := \frac{4.1}{3.3} \cdot VSP$$

$SUM := OL + OPX + CPX + SP \qquad SUM = 0.997$

$$OL := \frac{OL}{SUM} \quad OPX := \frac{OPX}{SUM} \quad CPX := \frac{CPX}{SUM} \quad SP := \frac{SP}{SUM}$$

$OL = 0.736 \quad OPX = 0.187 \quad CPX = 0.066 \quad SP = 0.011$

Calculate coefficients for left-hand terms in three best-fit linear equations:

$a_1 := 0.0911 - 0.4621 \cdot OL \qquad a_2 := 0.1895 - 0.3098 \cdot (OL + OPX)$

$a_3 := 0.2873 - 0.3061 \cdot (OL + OPX + CPX)$

Calculate right-hand terms for equations:

$b_1 := 0.2906 - 0.4621 \cdot OL \qquad b_2 := 0.2725 - 0.3098 \cdot (OL + OPX)$

$b_3 := 0.3002 - 0.3061 \cdot (OL + OPX + CPX)$

Define column vectors A and B for A*F=B:

$$A := \begin{bmatrix} a_1 \\ a_2 \\ a_3 \end{bmatrix} \qquad B := \begin{bmatrix} b_1 \\ b_2 \\ b_3 \end{bmatrix}$$

Calculate least-squares solution for F:

$F := (A^T \cdot A)^{-1} \cdot A^T \cdot B \qquad F = 0.192$

Sample ID: RC27-9:18-45

Enter the volume fractions of the four phases:

$VOL := 0.779 \quad VOPX := 0.194 \quad VCPX := 0.023 \quad VSP := 0.004$

Convert to mass fractions, assuming ρ_{rock} = 3.3 g/cm^3 and others as shown:

$$OL := \frac{3.3}{3.3} \cdot VOL \quad OPX := \frac{3.3}{3.3} \cdot VOPX \quad CPX := \frac{3.0}{3.3} \cdot VCPX \quad SP := \frac{4.1}{3.3} \cdot VSP$$

$SUM := OL + OPX + CPX + SP \quad SUM = 0.999$

$$OL := \frac{OL}{SUM} \quad OPX := \frac{OPX}{SUM} \quad CPX := \frac{CPX}{SUM} \quad SP := \frac{SP}{SUM}$$

$OL = 0.78 \quad OPX = 0.194 \quad CPX = 0.021 \quad SP = 0.005$

Calculate coefficients for left-hand terms in three best-fit linear equations:

$a_1 := 0.0911 - 0.4621 \cdot OL \quad a_2 := 0.1895 - 0.3098 \cdot (OL + OPX)$

$a_3 := 0.2873 - 0.3061 \cdot (OL + OPX + CPX)$

Calculate right-hand terms for equations:

$b_1 := 0.2906 - 0.4621 \cdot OL \quad b_2 := 0.2725 - 0.3098 \cdot (OL + OPX)$

$b_3 := 0.3002 - 0.3061 \cdot (OL + OPX + CPX)$

Define column vectors A and B for A*F=B:

$$A := \begin{bmatrix} a_1 \\ a_2 \\ a_3 \end{bmatrix} \quad B := \begin{bmatrix} b_1 \\ b_2 \\ b_3 \end{bmatrix}$$

Calculate least-squares solution for F:

$F := (A^T \cdot A)^{-1} \cdot A^T \cdot B \quad F = 0.259$

Sample ID: RC27-9:18-55

Enter the volume fractions of the four phases:

$VOL := 0.745 \qquad VOPX := 0.205 \qquad VCPX := 0.045 \qquad VSP := 0.005$

Convert to mass fractions, assuming ρ_{rock} = 3.3 g/cm^3 and others as shown:

$$OL := \frac{3.3}{3.3} \cdot VOL \qquad OPX := \frac{3.3}{3.3} \cdot VOPX \qquad CPX := \frac{3.0}{3.3} \cdot VCPX \qquad SP := \frac{4.1}{3.3} \cdot VSP$$

$SUM := OL + OPX + CPX + SP \qquad SUM = 0.997$

$$OL := \frac{OL}{SUM} \qquad OPX := \frac{OPX}{SUM} \qquad CPX := \frac{CPX}{SUM} \qquad SP := \frac{SP}{SUM}$$

$OL = 0.747 \qquad OPX = 0.206 \qquad CPX = 0.041 \qquad SP = 0.006$

Calculate coefficients for left-hand terms in three best-fit linear equations:

$a_1 := 0.0911 - 0.4621 \cdot OL \qquad a_2 := 0.1895 - 0.3098 \cdot (OL + OPX)$

$a_3 := 0.2873 - 0.3061 \cdot (OL + OPX + CPX)$

Calculate right-hand terms for equations:

$b_1 := 0.2906 - 0.4621 \cdot OL \qquad b_2 := 0.2725 - 0.3098 \cdot (OL + OPX)$

$b_3 := 0.3002 - 0.3061 \cdot (OL + OPX + CPX)$

Define column vectors A and B for A*F=B:

$$A := \begin{bmatrix} a_1 \\ a_2 \\ a_3 \end{bmatrix} \qquad B := \begin{bmatrix} b_1 \\ b_2 \\ b_3 \end{bmatrix}$$

Calculate least-squares solution for F:

$F := (A^T \cdot A)^{-1} \cdot A^T \cdot B \qquad F = 0.215$

Sample ID: RC27-9:19-1

Enter the volume fractions of the four phases:

$VOL := 0.838 \qquad VOPX := 0.0 \qquad VCPX := 0.0 \qquad VSP := 0.162$

Convert to mass fractions, assuming ρ_{rock} = 3.3 g/cm^3 and others as shown:

$$OL := \frac{3.3}{3.3} \cdot VOL \qquad OPX := \frac{3.3}{3.3} \cdot VOPX \qquad CPX := \frac{3.0}{3.3} \cdot VCPX \qquad SP := \frac{4.1}{3.3} \cdot VSP$$

$SUM := OL + OPX + CPX + SP \qquad SUM = 1.039$

$$OL := \frac{OL}{SUM} \qquad OPX := \frac{OPX}{SUM} \qquad CPX := \frac{CPX}{SUM} \qquad SP := \frac{SP}{SUM}$$

$OL = 0.806 \qquad OPX = 0 \qquad CPX = 0 \qquad SP = 0.194$

Calculate coefficients for left-hand terms in three best-fit linear equations:

$a_1 := 0.0911 - 0.4621 \cdot OL \qquad a_2 := 0.1895 - 0.3098 \cdot (OL + OPX)$

$a_3 := 0.2873 - 0.3061 \cdot (OL + OPX + CPX)$

Calculate right-hand terms for equations:

$b_1 := 0.2906 - 0.4621 \cdot OL \qquad b_2 := 0.2725 - 0.3098 \cdot (OL + OPX)$

$b_3 := 0.3002 - 0.3061 \cdot (OL + OPX + CPX)$

Define column vectors A and B for A*F=B:

$$A := \begin{bmatrix} a_1 \\ a_2 \\ a_3 \end{bmatrix} \qquad B := \begin{bmatrix} b_1 \\ b_2 \\ b_3 \end{bmatrix}$$

Calculate least-squares solution for F:

$F := (A^T \cdot A)^{-1} \cdot A^T \cdot B \qquad F = 0.283$

Sample ID: RC27-9:30-32

Enter the volume fractions of the four phases:

$VOL := 0.425 \qquad VOPX := 0.421 \qquad VCPX := 0.151 \qquad VSP := 0.005$

Convert to mass fractions, assuming ρ_{rock} = 3.3 g/cm^3 and others as shown:

$$OL := \frac{3.3}{3.3} \cdot VOL \qquad OPX := \frac{3.3}{3.3} \cdot VOPX \qquad CPX := \frac{3.0}{3.3} \cdot VCPX \qquad SP := \frac{4.1}{3.3} \cdot VSP$$

$SUM := OL + OPX + CPX + SP \qquad SUM = 0.989$

$$OL := \frac{OL}{SUM} \qquad OPX := \frac{OPX}{SUM} \qquad CPX := \frac{CPX}{SUM} \qquad SP := \frac{SP}{SUM}$$

$OL = 0.43 \qquad OPX = 0.425 \qquad CPX = 0.139 \qquad SP = 0.006$

Calculate coefficients for left-hand terms in three best-fit linear equations:

$a_1 := 0.0911 - 0.4621 \cdot OL \qquad a_2 := 0.1895 - 0.3098 \cdot (OL + OPX)$

$a_3 := 0.2873 - 0.3061 \cdot (OL + OPX + CPX)$

Calculate right-hand terms for equations:

$b_1 := 0.2906 - 0.4621 \cdot OL \qquad b_2 := 0.2725 - 0.3098 \cdot (OL + OPX)$

$b_3 := 0.3002 - 0.3061 \cdot (OL + OPX + CPX)$

Define column vectors A and B for A*F=B:

$$A := \begin{bmatrix} a_1 \\ a_2 \\ a_3 \end{bmatrix} \qquad B := \begin{bmatrix} b_1 \\ b_2 \\ b_3 \end{bmatrix}$$

Calculate least-squares solution for F:

$F := \left(A^T \cdot A\right)^{-1} \cdot A^T \cdot B \qquad F = -0.594$

Sample ID: RC27-9:30-40

Enter the volume fractions of the four phases:

$VOL := 0.663 \qquad VOPX := 0.237 \qquad VCPX := 0.092 \qquad VSP := 0.008$

Convert to mass fractions, assuming ρ_{rock} = 3.3 g/cm^3 and others as shown:

$$OL := \frac{3.3}{3.3} \cdot VOL \qquad OPX := \frac{3.3}{3.3} \cdot VOPX \qquad CPX := \frac{3.0}{3.3} \cdot VCPX \qquad SP := \frac{4.1}{3.3} \cdot VSP$$

$SUM := OL + OPX + CPX + SP \qquad SUM = 0.994$

$$OL := \frac{OL}{SUM} \qquad OPX := \frac{OPX}{SUM} \qquad CPX := \frac{CPX}{SUM} \qquad SP := \frac{SP}{SUM}$$

$OL = 0.667 \qquad OPX = 0.239 \qquad CPX = 0.084 \qquad SP = 0.01$

Calculate coefficients for left-hand terms in three best-fit linear equations:

$a_1 := 0.0911 - 0.4621 \cdot OL \qquad a_2 := 0.1895 - 0.3098 \cdot (OL + OPX)$

$a_3 := 0.2873 - 0.3061 \cdot (OL + OPX + CPX)$

Calculate right-hand terms for equations:

$b_1 := 0.2906 - 0.4621 \cdot OL \qquad b_2 := 0.2725 - 0.3098 \cdot (OL + OPX)$

$b_3 := 0.3002 - 0.3061 \cdot (OL + OPX + CPX)$

Define column vectors A and B for A*F=B:

$$A := \begin{bmatrix} a_1 \\ a_2 \\ a_3 \end{bmatrix} \qquad B := \begin{bmatrix} b_1 \\ b_2 \\ b_3 \end{bmatrix}$$

Calculate least-squares solution for F:

$F := \left(A^T \cdot A\right)^{-1} \cdot A^T \cdot B \qquad F = 0.083$

Sample ID: RC27-9:30-42

Enter the volume fractions of the four phases:

$VOL := 0.701 \qquad VOPX := 0.235 \qquad VCPX := 0.053 \qquad VSP := 0.010$

Convert to mass fractions, assuming ρ_{rock} = 3.3 g/cm^3 and others as shown:

$$OL := \frac{3.3}{3.3} \cdot VOL \qquad OPX := \frac{3.3}{3.3} \cdot VOPX \qquad CPX := \frac{3.0}{3.3} \cdot VCPX \qquad SP := \frac{4.1}{3.3} \cdot VSP$$

$SUM := OL + OPX + CPX + SP \qquad SUM = 0.997$

$$OL := \frac{OL}{SUM} \qquad OPX := \frac{OPX}{SUM} \qquad CPX := \frac{CPX}{SUM} \qquad SP := \frac{SP}{SUM}$$

$OL = 0.703 \qquad OPX = 0.236 \qquad CPX = 0.048 \qquad SP = 0.012$

Calculate coefficients for left-hand terms in three best-fit linear equations:

$a_1 := 0.0911 - 0.4621 \cdot OL \qquad a_2 := 0.1895 - 0.3098 \cdot (OL + OPX)$

$a_3 := 0.2873 - 0.3061 \cdot (OL + OPX + CPX)$

Calculate right-hand terms for equations:

$b_1 := 0.2906 - 0.4621 \cdot OL \qquad b_2 := 0.2725 - 0.3098 \cdot (OL + OPX)$

$b_3 := 0.3002 - 0.3061 \cdot (OL + OPX + CPX)$

Define column vectors A and B for A*F=B:

$$A := \begin{bmatrix} a_1 \\ a_2 \\ a_3 \end{bmatrix} \qquad B := \begin{bmatrix} b_1 \\ b_2 \\ b_3 \end{bmatrix}$$

Calculate least-squares solution for F:

$F := \left(A^T \cdot A\right)^{-1} \cdot A^T \cdot B \qquad F = 0.153$

Sample ID: RC27-9:30-44

Enter the volume fractions of the four phases:

$VOL := 0.650 \qquad VOPX := 0.245 \qquad VCPX := 0.095 \qquad VSP := 0.010$

Convert to mass fractions, assuming ρ_{rock} = 3.3 g/cm^3 and others as shown:

$$OL := \frac{3.3}{3.3} \cdot VOL \qquad OPX := \frac{3.3}{3.3} \cdot VOPX \qquad CPX := \frac{3.0}{3.3} \cdot VCPX \qquad SP := \frac{4.1}{3.3} \cdot VSP$$

$SUM := OL + OPX + CPX + SP \qquad SUM = 0.994$

$$OL := \frac{OL}{SUM} \qquad OPX := \frac{OPX}{SUM} \qquad CPX := \frac{CPX}{SUM} \qquad SP := \frac{SP}{SUM}$$

$OL = 0.654 \qquad OPX = 0.247 \qquad CPX = 0.087 \qquad SP = 0.013$

Calculate coefficients for left-hand terms in three best-fit linear equations:

$a_1 := 0.0911 - 0.4621 \cdot OL \qquad a_2 := 0.1895 - 0.3098 \cdot (OL + OPX)$

$a_3 := 0.2873 - 0.3061 \cdot (OL + OPX + CPX)$

Calculate right-hand terms for equations:

$b_1 := 0.2906 - 0.4621 \cdot OL \qquad b_2 := 0.2725 - 0.3098 \cdot (OL + OPX)$

$b_3 := 0.3002 - 0.3061 \cdot (OL + OPX + CPX)$

Define column vectors A and B for A*F=B:

$$A := \begin{bmatrix} a_1 \\ a_2 \\ a_3 \end{bmatrix} \qquad B := \begin{bmatrix} b_1 \\ b_2 \\ b_3 \end{bmatrix}$$

Calculate least-squares solution for F:

$F := (A^T \cdot A)^{-1} \cdot A^T \cdot B \qquad F = 0.058$

Sample ID: RC27-9:25-138

Enter the volume fractions of the four phases:

$VOL := 0.711 \quad VOPX := 0.183 \quad VCPX := 0.095 \quad VSP := 0.011$

Convert to mass fractions, assuming ρ_{rock} = 3.3 g/cm^3 and others as shown:

$$OL := \frac{3.3}{3.3} \cdot VOL \quad OPX := \frac{3.3}{3.3} \cdot VOPX \quad CPX := \frac{3.0}{3.3} \cdot VCPX \quad SP := \frac{4.1}{3.3} \cdot VSP$$

$SUM := OL + OPX + CPX + SP \qquad SUM = 0.994$

$$OL := \frac{OL}{SUM} \quad OPX := \frac{OPX}{SUM} \quad CPX := \frac{CPX}{SUM} \quad SP := \frac{SP}{SUM}$$

$OL = 0.715 \quad OPX = 0.184 \quad CPX = 0.087 \quad SP = 0.014$

Calculate coefficients for left-hand terms in three best-fit linear equations:

$a_1 := 0.0911 - 0.4621 \cdot OL \qquad a_2 := 0.1895 - 0.3098 \cdot (OL + OPX)$

$a_3 := 0.2873 - 0.3061 \cdot (OL + OPX + CPX)$

Calculate right-hand terms for equations:

$b_1 := 0.2906 - 0.4621 \cdot OL \qquad b_2 := 0.2725 - 0.3098 \cdot (OL + OPX)$

$b_3 := 0.3002 - 0.3061 \cdot (OL + OPX + CPX)$

Define column vectors A and B for A*F=B:

$$A := \begin{bmatrix} a_1 \\ a_2 \\ a_3 \end{bmatrix} \qquad B := \begin{bmatrix} b_1 \\ b_2 \\ b_3 \end{bmatrix}$$

Calculate least-squares solution for F:

$F := (A^T \cdot A)^{-1} \cdot A^T \cdot B \qquad F = 0.155$

Sample ID: RC27-9:25-142

Enter the volume fractions of the four phases:

$VOL := 0.561 \qquad VOPX := 0.335 \qquad VCPX := 0.090 \qquad VSP := 0.015$

Convert to mass fractions, assuming ρ_{rock} = 3.3 g/cm^3 and others as shown:

$$OL := \frac{3.3}{3.3} \cdot VOL \qquad OPX := \frac{3.3}{3.3} \cdot VOPX \qquad CPX := \frac{3.0}{3.3} \cdot VCPX \qquad SP := \frac{4.1}{3.3} \cdot VSP$$

$SUM := OL + OPX + CPX + SP \qquad SUM = 0.996$

$$OL := \frac{OL}{SUM} \qquad OPX := \frac{OPX}{SUM} \qquad CPX := \frac{CPX}{SUM} \qquad SP := \frac{SP}{SUM}$$

$OL = 0.563 \qquad OPX = 0.336 \qquad CPX = 0.082 \qquad SP = 0.019$

Calculate coefficients for left-hand terms in three best-fit linear equations:

$a_1 := 0.0911 - 0.4621 \cdot OL \qquad a_2 := 0.1895 - 0.3098 \cdot (OL + OPX)$

$a_3 := 0.2873 - 0.3061 \cdot (OL + OPX + CPX)$

Calculate right-hand terms for equations:

$b_1 := 0.2906 - 0.4621 \cdot OL \qquad b_2 := 0.2725 - 0.3098 \cdot (OL + OPX)$

$b_3 := 0.3002 - 0.3061 \cdot (OL + OPX + CPX)$

Define column vectors A and B for A*F=B:

$$A := \begin{bmatrix} a_1 \\ a_2 \\ a_3 \end{bmatrix} \qquad B := \begin{bmatrix} b_1 \\ b_2 \\ b_3 \end{bmatrix}$$

Calculate least-squares solution for F:

$F := \left(A^T \cdot A\right)^{-1} \cdot A^T \cdot B \qquad F = -0.125$

Sample ID: RC27-9:34-35

Enter the volume fractions of the four phases:

$VOL := 0.779 \qquad VOPX := 0.199 \qquad VCPX := 0.017 \qquad VSP := 0.006$

Convert to mass fractions, assuming ρ_{rock} = 3.3 g/cm^3 and others as shown:

$$OL := \frac{3.3}{3.3} \cdot VOL \qquad OPX := \frac{3.3}{3.3} \cdot VOPX \qquad CPX := \frac{3.0}{3.3} \cdot VCPX \qquad SP := \frac{4.1}{3.3} \cdot VSP$$

$SUM := OL + OPX + CPX + SP \qquad SUM = 1.001$

$$OL := \frac{OL}{SUM} \qquad OPX := \frac{OPX}{SUM} \qquad CPX := \frac{CPX}{SUM} \qquad SP := \frac{SP}{SUM}$$

$OL = 0.778 \qquad OPX = 0.199 \qquad CPX = 0.015 \qquad SP = 0.007$

Calculate coefficients for left-hand terms in three best-fit linear equations:

$a_1 := 0.0911 - 0.4621 \cdot OL \qquad a_2 := 0.1895 - 0.3098 \cdot (OL + OPX)$

$a_3 := 0.2873 - 0.3061 \cdot (OL + OPX + CPX)$

Calculate right-hand terms for equations:

$b_1 := 0.2906 - 0.4621 \cdot OL \qquad b_2 := 0.2725 - 0.3098 \cdot (OL + OPX)$

$b_3 := 0.3002 - 0.3061 \cdot (OL + OPX + CPX)$

Define column vectors A and B for A*F=B:

$$A := \begin{bmatrix} a_1 \\ a_2 \\ a_3 \end{bmatrix} \qquad B := \begin{bmatrix} b_1 \\ b_2 \\ b_3 \end{bmatrix}$$

Calculate least-squares solution for F:

$F := \left(A^T \cdot A\right)^{-1} \cdot A^T \cdot B \qquad F = 0.258$

Sample ID: RC27-9:34-58

Enter the volume fractions of the four phases:

VOL := 0.709 VOPX := 0.254 VCPX := 0.033 VSP := 0.004

Convert to mass fractions, assuming ρ_{rock} = 3.3 g/cm^3 and others as shown:

$$OL := \frac{3.3}{3.3}\cdot VOL \qquad OPX := \frac{3.3}{3.3}\cdot VOPX \qquad CPX := \frac{3.0}{3.3}\cdot VCPX \qquad SP := \frac{4.1}{3.3}\cdot VSP$$

$$SUM := OL + OPX + CPX + SP \qquad SUM = 0.998$$

$$OL := \frac{OL}{SUM} \qquad OPX := \frac{OPX}{SUM} \qquad CPX := \frac{CPX}{SUM} \qquad SP := \frac{SP}{SUM}$$

OL = 0.71 OPX = 0.255 CPX = 0.03 SP = 0.005

Calculate coefficients for left-hand terms in three best-fit linear equations:

$a_1 := 0.0911 - 0.4621\cdot OL$ $a_2 := 0.1895 - 0.3098\cdot(OL + OPX)$

$a_3 := 0.2873 - 0.3061\cdot(OL + OPX + CPX)$

Calculate right-hand terms for equations:

$b_1 := 0.2906 - 0.4621\cdot OL$ $b_2 := 0.2725 - 0.3098\cdot(OL + OPX)$

$b_3 := 0.3002 - 0.3061\cdot(OL + OPX + CPX)$

Define column vectors A and B for A*F=B:

$$A := \begin{bmatrix} a_1 \\ a_2 \\ a_3 \end{bmatrix} \qquad B := \begin{bmatrix} b_1 \\ b_2 \\ b_3 \end{bmatrix}$$

Calculate least-squares solution for F:

$$F := \left(A^T\cdot A\right)^{-1}\cdot A^T\cdot B \qquad F = 0.174$$

Sample ID: RC27-9:34-63

Enter the volume fractions of the four phases:

$VOL := 0.711 \quad VOPX := 0.227 \quad VCPX := 0.055 \quad VSP := 0.007$

Convert to mass fractions, assuming ρ_{rock} = 3.3 g/cm^3 and others as shown:

$$OL := \frac{3.3}{3.3} \cdot VOL \quad OPX := \frac{3.3}{3.3} \cdot VOPX \quad CPX := \frac{3.0}{3.3} \cdot VCPX \quad SP := \frac{4.1}{3.3} \cdot VSP$$

$SUM := OL + OPX + CPX + SP \qquad SUM = 0.997$

$$OL := \frac{OL}{SUM} \quad OPX := \frac{OPX}{SUM} \quad CPX := \frac{CPX}{SUM} \quad SP := \frac{SP}{SUM}$$

$OL = 0.713 \quad OPX = 0.228 \quad CPX = 0.05 \quad SP = 0.009$

Calculate coefficients for left-hand terms in three best-fit linear equations:

$a_1 := 0.0911 - 0.4621 \cdot OL \qquad a_2 := 0.1895 - 0.3098 \cdot (OL + OPX)$

$a_3 := 0.2873 - 0.3061 \cdot (OL + OPX + CPX)$

Calculate right-hand terms for equations:

$b_1 := 0.2906 - 0.4621 \cdot OL \qquad b_2 := 0.2725 - 0.3098 \cdot (OL + OPX)$

$b_3 := 0.3002 - 0.3061 \cdot (OL + OPX + CPX)$

Define column vectors A and B for A*F=B:

$$A := \begin{bmatrix} a_1 \\ a_2 \\ a_3 \end{bmatrix} \qquad B := \begin{bmatrix} b_1 \\ b_2 \\ b_3 \end{bmatrix}$$

Calculate least-squares solution for F:

$F := (A^T \cdot A)^{-1} \cdot A^T \cdot B \qquad F = 0.167$

Sample ID: RC27-9:34-69

Enter the volume fractions of the four phases:

$VOL := 0.691 \qquad VOPX := 0.268 \qquad VCPX := 0.035 \qquad VSP := 0.006$

Convert to mass fractions, assuming ρ_{rock} = 3.3 g/cm^3 and others as shown:

$$OL := \frac{3.3}{3.3} \cdot VOL \qquad OPX := \frac{3.3}{3.3} \cdot VOPX \qquad CPX := \frac{3.0}{3.3} \cdot VCPX \qquad SP := \frac{4.1}{3.3} \cdot VSP$$

$SUM := OL + OPX + CPX + SP \qquad SUM = 0.998$

$$OL := \frac{OL}{SUM} \qquad OPX := \frac{OPX}{SUM} \qquad CPX := \frac{CPX}{SUM} \qquad SP := \frac{SP}{SUM}$$

$OL = 0.692 \qquad OPX = 0.268 \qquad CPX = 0.032 \qquad SP = 0.007$

Calculate coefficients for left-hand terms in three best-fit linear equations:

$a_1 := 0.0911 - 0.4621 \cdot OL \qquad a_2 := 0.1895 - 0.3098 \cdot (OL + OPX)$

$a_3 := 0.2873 - 0.3061 \cdot (OL + OPX + CPX)$

Calculate right-hand terms for equations:

$b_1 := 0.2906 - 0.4621 \cdot OL \qquad b_2 := 0.2725 - 0.3098 \cdot (OL + OPX)$

$b_3 := 0.3002 - 0.3061 \cdot (OL + OPX + CPX)$

Define column vectors A and B for A*F=B:

$$A := \begin{bmatrix} a_1 \\ a_2 \\ a_3 \end{bmatrix} \qquad B := \begin{bmatrix} b_1 \\ b_2 \\ b_3 \end{bmatrix}$$

Calculate least-squares solution for F:

$F := \left(A^T \cdot A\right)^{-1} \cdot A^T \cdot B \qquad F = 0.147$

Sample ID: RC27-9:35-41

Enter the volume fractions of the four phases:

$VOL := 0.855 \qquad VOPX := 0.137 \qquad VCPX := 0.004 \qquad VSP := 0.004$

Convert to mass fractions, assuming ρ_{rock} = 3.3 g/cm^3 and others as shown:

$$OL := \frac{3.3}{3.3} \cdot VOL \qquad OPX := \frac{3.3}{3.3} \cdot VOPX \qquad CPX := \frac{3.0}{3.3} \cdot VCPX \qquad SP := \frac{4.1}{3.3} \cdot VSP$$

$SUM := OL + OPX + CPX + SP \qquad SUM = 1.001$

$$OL := \frac{OL}{SUM} \qquad OPX := \frac{OPX}{SUM} \qquad CPX := \frac{CPX}{SUM} \qquad SP := \frac{SP}{SUM}$$

$OL = 0.854 \qquad OPX = 0.137 \qquad CPX = 0.004 \qquad SP = 0.005$

Calculate coefficients for left-hand terms in three best-fit linear equations:

$a_1 := 0.0911 - 0.4621 \cdot OL \qquad a_2 := 0.1895 - 0.3098 \cdot (OL + OPX)$

$a_3 := 0.2873 - 0.3061 \cdot (OL + OPX + CPX)$

Calculate right-hand terms for equations:

$b_1 := 0.2906 - 0.4621 \cdot OL \qquad b_2 := 0.2725 - 0.3098 \cdot (OL + OPX)$

$b_3 := 0.3002 - 0.3061 \cdot (OL + OPX + CPX)$

Define column vectors A and B for A*F=B:

$$A := \begin{bmatrix} a_1 \\ a_2 \\ a_3 \end{bmatrix} \qquad B := \begin{bmatrix} b_1 \\ b_2 \\ b_3 \end{bmatrix}$$

Calculate least-squares solution for F:

$F := (A^T \cdot A)^{-1} \cdot A^T \cdot B \qquad F = 0.337$

Sample ID: RC27-9:35-44

Enter the volume fractions of the four phases:

$VOL := 0.867 \qquad VOPX := 0.130 \qquad VCPX := 0.000 \qquad VSP := 0.003$

Convert to mass fractions, assuming ρ_{rock} = 3.3 g/cm^3 and others as shown:

$$OL := \frac{3.3}{3.3} \cdot VOL \qquad OPX := \frac{3.3}{3.3} \cdot VOPX \qquad CPX := \frac{3.0}{3.3} \cdot VCPX \qquad SP := \frac{4.1}{3.3} \cdot VSP$$

$SUM := OL + OPX + CPX + SP \qquad SUM = 1.001$

$$OL := \frac{OL}{SUM} \qquad OPX := \frac{OPX}{SUM} \qquad CPX := \frac{CPX}{SUM} \qquad SP := \frac{SP}{SUM}$$

$OL = 0.866 \qquad OPX = 0.13 \qquad CPX = 0 \qquad SP = 0.004$

Calculate coefficients for left-hand terms in three best-fit linear equations:

$a_1 := 0.0911 - 0.4621 \cdot OL \qquad a_2 := 0.1895 - 0.3098 \cdot (OL + OPX)$

$a_3 := 0.2873 - 0.3061 \cdot (OL + OPX + CPX)$

Calculate right-hand terms for equations:

$b_1 := 0.2906 - 0.4621 \cdot OL \qquad b_2 := 0.2725 - 0.3098 \cdot (OL + OPX)$

$b_3 := 0.3002 - 0.3061 \cdot (OL + OPX + CPX)$

Define column vectors A and B for A*F=B:

$$A := \begin{bmatrix} a_1 \\ a_2 \\ a_3 \end{bmatrix} \qquad B := \begin{bmatrix} b_1 \\ b_2 \\ b_3 \end{bmatrix}$$

Calculate least-squares solution for F:

$F := \left(A^T \cdot A\right)^{-1} \cdot A^T \cdot B \qquad F = 0.348$

Sample ID: RC27-9:35-49

Enter the volume fractions of the four phases:

$VOL := 0.760 \qquad VOPX := 0.195 \qquad VCPX := 0.041 \qquad VSP := 0.005$

Convert to mass fractions, assuming ρ_{rock} = 3.3 g/cm^3 and others as shown:

$$OL := \frac{3.3}{3.3} \cdot VOL \qquad OPX := \frac{3.3}{3.3} \cdot VOPX \qquad CPX := \frac{3.0}{3.3} \cdot VCPX \qquad SP := \frac{4.1}{3.3} \cdot VSP$$

$SUM := OL + OPX + CPX + SP \qquad SUM = 0.998$

$$OL := \frac{OL}{SUM} \qquad OPX := \frac{OPX}{SUM} \qquad CPX := \frac{CPX}{SUM} \qquad SP := \frac{SP}{SUM}$$

$OL = 0.761 \qquad OPX = 0.195 \qquad CPX = 0.037 \qquad SP = 0.006$

Calculate coefficients for left-hand terms in three best-fit linear equations:

$a_1 := 0.0911 - 0.4621 \cdot OL \qquad a_2 := 0.1895 - 0.3098 \cdot (OL + OPX)$

$a_3 := 0.2873 - 0.3061 \cdot (OL + OPX + CPX)$

Calculate right-hand terms for equations:

$b_1 := 0.2906 - 0.4621 \cdot OL \qquad b_2 := 0.2725 - 0.3098 \cdot (OL + OPX)$

$b_3 := 0.3002 - 0.3061 \cdot (OL + OPX + CPX)$

Define column vectors A and B for A*F=B:

$$A := \begin{bmatrix} a_1 \\ a_2 \\ a_3 \end{bmatrix} \qquad B := \begin{bmatrix} b_1 \\ b_2 \\ b_3 \end{bmatrix}$$

Calculate least-squares solution for F:

$F := \left(A^T \cdot A\right)^{-1} \cdot A^T \cdot B \qquad F = 0.233$

Sample ID: RC27-9:35-52

Enter the volume fractions of the four phases:

$VOL := 0.696 \qquad VOPX := 0.258 \qquad VCPX := 0.041 \qquad VSP := 0.005$

Convert to mass fractions, assuming ρ_{rock} = 3.3 g/cm^3 and others as shown:

$$OL := \frac{3.3}{3.3} \cdot VOL \qquad OPX := \frac{3.3}{3.3} \cdot VOPX \qquad CPX := \frac{3.0}{3.3} \cdot VCPX \qquad SP := \frac{4.1}{3.3} \cdot VSP$$

$SUM := OL + OPX + CPX + SP \qquad SUM = 0.997$

$$OL := \frac{OL}{SUM} \qquad OPX := \frac{OPX}{SUM} \qquad CPX := \frac{CPX}{SUM} \qquad SP := \frac{SP}{SUM}$$

$OL = 0.698 \qquad OPX = 0.259 \qquad CPX = 0.037 \qquad SP = 0.006$

Calculate coefficients for left-hand terms in three best-fit linear equations:

$a_1 := 0.0911 - 0.4621 \cdot OL \qquad a_2 := 0.1895 - 0.3098 \cdot (OL + OPX)$

$a_3 := 0.2873 - 0.3061 \cdot (OL + OPX + CPX)$

Calculate right-hand terms for equations:

$b_1 := 0.2906 - 0.4621 \cdot OL \qquad b_2 := 0.2725 - 0.3098 \cdot (OL + OPX)$

$b_3 := 0.3002 - 0.3061 \cdot (OL + OPX + CPX)$

Define column vectors A and B for A*F=B:

$$A := \begin{bmatrix} a_1 \\ a_2 \\ a_3 \end{bmatrix} \qquad B := \begin{bmatrix} b_1 \\ b_2 \\ b_3 \end{bmatrix}$$

Calculate least-squares solution for F:

$F := (A^T \cdot A)^{-1} \cdot A^T \cdot B \qquad F = 0.153$

Sample ID: RC27-9:35-80

Enter the volume fractions of the four phases:

$VOL := 0.745 \qquad VOPX := 0.203 \qquad VCPX := 0.050 \qquad VSP := 0.002$

Convert to mass fractions, assuming ρ_{rock} = 3.3 g/cm^3 and others as shown:

$$OL := \frac{3.3}{3.3} \cdot VOL \qquad OPX := \frac{3.3}{3.3} \cdot VOPX \qquad CPX := \frac{3.0}{3.3} \cdot VCPX \qquad SP := \frac{4.1}{3.3} \cdot VSP$$

$SUM := OL + OPX + CPX + SP \qquad SUM = 0.996$

$$OL := \frac{OL}{SUM} \qquad OPX := \frac{OPX}{SUM} \qquad CPX := \frac{CPX}{SUM} \qquad SP := \frac{SP}{SUM}$$

$OL = 0.748 \qquad OPX = 0.204 \qquad CPX = 0.046 \qquad SP = 0.002$

Calculate coefficients for left-hand terms in three best-fit linear equations:

$a_1 := 0.0911 - 0.4621 \cdot OL \qquad a_2 := 0.1895 - 0.3098 \cdot (OL + OPX)$

$a_3 := 0.2873 - 0.3061 \cdot (OL + OPX + CPX)$

Calculate right-hand terms for equations:

$b_1 := 0.2906 - 0.4621 \cdot OL \qquad b_2 := 0.2725 - 0.3098 \cdot (OL + OPX)$

$b_3 := 0.3002 - 0.3061 \cdot (OL + OPX + CPX)$

Define column vectors A and B for A*F=B:

$$A := \begin{bmatrix} a_1 \\ a_2 \\ a_3 \end{bmatrix} \qquad B := \begin{bmatrix} b_1 \\ b_2 \\ b_3 \end{bmatrix}$$

Calculate least-squares solution for F:

$F := \left(A^T \cdot A\right)^{-1} \cdot A^T \cdot B \qquad F = 0.216$

Sample ID: RC27-9:44-1

Enter the volume fractions of the four phases:

$VOL := 0.736 \quad VOPX := 0.213 \quad VCPX := 0.046 \quad VSP := 0.005$

Convert to mass fractions, assuming ρ_{rock} = 3.3 g/cm^3 and others as shown:

$$OL := \frac{3.3}{3.3} \cdot VOL \quad OPX := \frac{3.3}{3.3} \cdot VOPX \quad CPX := \frac{3.0}{3.3} \cdot VCPX \quad SP := \frac{4.1}{3.3} \cdot VSP$$

$SUM := OL + OPX + CPX + SP \quad SUM = 0.997$

$$OL := \frac{OL}{SUM} \quad OPX := \frac{OPX}{SUM} \quad CPX := \frac{CPX}{SUM} \quad SP := \frac{SP}{SUM}$$

$OL = 0.738 \quad OPX = 0.214 \quad CPX = 0.042 \quad SP = 0.006$

Calculate coefficients for left-hand terms in three best-fit linear equations:

$a_1 := 0.0911 - 0.4621 \cdot OL \quad a_2 := 0.1895 - 0.3098 \cdot (OL + OPX)$

$a_3 := 0.2873 - 0.3061 \cdot (OL + OPX + CPX)$

Calculate right-hand terms for equations:

$b_1 := 0.2906 - 0.4621 \cdot OL \quad b_2 := 0.2725 - 0.3098 \cdot (OL + OPX)$

$b_3 := 0.3002 - 0.3061 \cdot (OL + OPX + CPX)$

Define column vectors A and B for A*F=B:

$$A := \begin{bmatrix} a_1 \\ a_2 \\ a_3 \end{bmatrix} \quad B := \begin{bmatrix} b_1 \\ b_2 \\ b_3 \end{bmatrix}$$

Calculate least-squares solution for F:

$F := (A^T \cdot A)^{-1} \cdot A^T \cdot B \quad F = 0.204$

Sample ID: RC27-9:46-1

Enter the volume fractions of the four phases:

$VOL := 0.677 \quad VOPX := 0.259 \quad VCPX := 0.052 \quad VSP := 0.012$

Convert to mass fractions, assuming ρ_{rock} = 3.3 g/cm^3 and others as shown:

$$OL := \frac{3.3}{3.3} \cdot VOL \quad OPX := \frac{3.3}{3.3} \cdot VOPX \quad CPX := \frac{3.0}{3.3} \cdot VCPX \quad SP := \frac{4.1}{3.3} \cdot VSP$$

$SUM := OL + OPX + CPX + SP \qquad SUM = 0.998$

$$OL := \frac{OL}{SUM} \quad OPX := \frac{OPX}{SUM} \quad CPX := \frac{CPX}{SUM} \quad SP := \frac{SP}{SUM}$$

$OL = 0.678 \quad OPX = 0.259 \quad CPX = 0.047 \quad SP = 0.015$

Calculate coefficients for left-hand terms in three best-fit linear equations:

$a_1 := 0.0911 - 0.4621 \cdot OL \qquad a_2 := 0.1895 - 0.3098 \cdot (OL + OPX)$

$a_3 := 0.2873 - 0.3061 \cdot (OL + OPX + CPX)$

Calculate right-hand terms for equations:

$b_1 := 0.2906 - 0.4621 \cdot OL \qquad b_2 := 0.2725 - 0.3098 \cdot (OL + OPX)$

$b_3 := 0.3002 - 0.3061 \cdot (OL + OPX + CPX)$

Define column vectors A and B for A*F=B:

$$A := \begin{bmatrix} a_1 \\ a_2 \\ a_3 \end{bmatrix} \qquad B := \begin{bmatrix} b_1 \\ b_2 \\ b_3 \end{bmatrix}$$

Calculate least-squares solution for F:

$F := (A^T \cdot A)^{-1} \cdot A^T \cdot B \qquad F = 0.115$

Sample ID: RC27-9:46-2

Enter the volume fractions of the four phases:

$VOL := 0.747 \quad VOPX := 0.222 \quad VCPX := 0.021 \quad VSP := 0.010$

Convert to mass fractions, assuming ρ_{rock} = 3.3 g/cm^3 and others as shown:

$$OL := \frac{3.3}{3.3} \cdot VOL \quad OPX := \frac{3.3}{3.3} \cdot VOPX \quad CPX := \frac{3.0}{3.3} \cdot VCPX \quad SP := \frac{4.1}{3.3} \cdot VSP$$

$SUM := OL + OPX + CPX + SP \quad SUM = 1.001$

$$OL := \frac{OL}{SUM} \quad OPX := \frac{OPX}{SUM} \quad CPX := \frac{CPX}{SUM} \quad SP := \frac{SP}{SUM}$$

$OL = 0.747 \quad OPX = 0.222 \quad CPX = 0.019 \quad SP = 0.012$

Calculate coefficients for left-hand terms in three best-fit linear equations:

$a_1 := 0.0911 - 0.4621 \cdot OL \quad a_2 := 0.1895 - 0.3098 \cdot (OL + OPX)$

$a_3 := 0.2873 - 0.3061 \cdot (OL + OPX + CPX)$

Calculate right-hand terms for equations:

$b_1 := 0.2906 - 0.4621 \cdot OL \quad b_2 := 0.2725 - 0.3098 \cdot (OL + OPX)$

$b_3 := 0.3002 - 0.3061 \cdot (OL + OPX + CPX)$

Define column vectors A and B for A*F=B:

$$A := \begin{bmatrix} a_1 \\ a_2 \\ a_3 \end{bmatrix} \quad B := \begin{bmatrix} b_1 \\ b_2 \\ b_3 \end{bmatrix}$$

Calculate least-squares solution for F:

$F := (A^T \cdot A)^{-1} \cdot A^T \cdot B \quad F = 0.22$

WHOLE ROCK COMPOSITIONS

F=0 SOURCE ROCK

			MODE	BULK	
Ol	SiO2	40.24	0.63	SiO2	43.47
	FeO	10.04		TiO2	0.08
	MnO	0.26		Al2O3	3.82
	MgO	49.55		FeO	8.66
	CaO	0.02		MnO	0.18
	NiO	0.32		MgO	40.87
OPX	SiO2	52.39	0.25	CaO	2.28
	TiO2	0.1		Cr2O3	0.33
	Al2O3	7.09		Na2O	0.10
	FeO	7.37		NiO	0.21
	MnO	0.05		SUM	100.00
	MgO	31.06			
	CaO	0.41			
	Cr2O3	0.7			
CPX	SiO2	50.28	0.1		
	TiO2	0.53			
	Al2O3	7.94			
	FeO	2.9			
	MnO	0.08			
	MgO	14.64			
	CaO	21.62			
	Cr2O3	0.86			
	Na2O	1.01			
SP	TiO2	0.12	0.02		
	Al2O3	62.51			
	FeO	10.17			
	MnO	0			
	MgO	21.56			
	Cr2O3	3.21			
	NiO	0.21			

F=0.02

			MODE	BULK	
Ol	SiO2	40.27	0.6388	SiO2	43.52
	FeO	9.95		TiO2	0.07
	MnO	0.25		Al2O3	3.57
	MgO	49.53		FeO	8.62
	CaO	0.02		MnO	0.18
	NiO	0.32		MgO	41.18
OPX	SiO2	52.62	0.2467	CaO	2.20
	TiO2	0.10		Cr2O3	0.36
	Al2O3	6.80		Na2O	0.09
	FeO	7.26		NiO	0.21
	MnO	0.06		SUM	100.00
	MgO	31.25			
	CaO	0.48			
	Cr2O3	0.70			
CPX	SiO2	50.39	0.0953		
	TiO2	0.49			
	Al2O3	7.63			
	FeO	2.86			
	MnO	0.08			
	MgO	14.83			
	CaO	21.74			
	Cr2O3	0.89			
	Na2O	0.94			
SP	TiO2	0.12	0.0192		
	Al2O3	60.74			
	FeO	10.54			
	MnO	0.00			
	MgO	21.23			
	Cr2O3	5.12			
	NiO	0.21			

WHOLE ROCK COMPOSITIONS

F=0.05

			MODE	BULK	
Ol	SiO2	40.32	0.6526	SiO2	43.58
	FeO	9.82		TiO2	0.06
	MnO	0.23		Al2O3	3.21
	MgO	49.50		FeO	8.57
	CaO	0.02		MnO	0.17
	NiO	0.32		MgO	41.65
OPX	SiO2	52.96	0.2416	CaO	2.08
	TiO2	0.09		Cr2O3	0.40
	Al2O3	6.37		Na2O	0.07
	FeO	7.08		NiO	0.21
	MnO	0.06		SUM	100.00
	MgO	31.54			
	CaO	0.58			
	Cr2O3	0.71			
CPX	SiO2	50.55	0.0879		
	TiO2	0.43			
	Al2O3	7.17			
	FeO	2.80			
	MnO	0.08			
	MgO	15.10			
	CaO	21.91			
	Cr2O3	0.92			
	Na2O	0.84			
SP	TiO2	0.11	0.0179		
	Al2O3	58.08			
	FeO	11.10			
	MnO	0.01			
	MgO	20.74			
	Cr2O3	7.99			
	NiO	0.21			

F=0.08

			MODE	BULK	
Ol	SiO2	40.37	0.6674	SiO2	43.63
	FeO	9.69		TiO2	0.05
	MnO	0.21		Al2O3	2.86
	MgO	49.47		FeO	8.52
	CaO	0.02		MnO	0.16
	NiO	0.32		MgO	42.13
OPX	SiO2	53.30	0.2361	CaO	1.95
	TiO2	0.08		Cr2O3	0.43
	Al2O3	5.94		Na2O	0.06
	FeO	6.91		NiO	0.22
	MnO	0.07		SUM	100.00
	MgO	31.83			
	CaO	0.69			
	Cr2O3	0.72			
CPX	SiO2	50.72	0.0800		
	TiO2	0.37			
	Al2O3	6.71			
	FeO	2.74			
	MnO	0.08			
	MgO	15.38			
	CaO	22.08			
	Cr2O3	0.96			
	Na2O	0.75			
SP	TiO2	0.10	0.0165		
	Al2O3	55.43			
	FeO	11.66			
	MnO	0.03			
	MgO	20.25			
	Cr2O3	10.85			
	NiO	0.21			

WHOLE ROCK COMPOSITIONS

F=1.0

			MODE	BULK	
Ol	SiO2	40.41	0.6778	SiO2	43.66
	FeO	9.60		TiO2	0.04
	MnO	0.20		Al2O3	2.63
	MgO	49.44		FeO	8.48
	CaO	0.03		MnO	0.16
	NiO	0.32		MgO	42.47
OPX	SiO2	53.53	0.2322	CaO	1.85
	TiO2	0.08		Cr2O3	0.44
	Al2O3	5.65		Na2O	0.05
	FeO	6.80		NiO	0.22
	MnO	0.08		SUM	100.00
	MgO	32.02			
	CaO	0.75			
	Cr2O3	0.72			
CPX	SiO2	50.83	0.0744		
	TiO2	0.33			
	Al2O3	6.40			
	FeO	2.70			
	MnO	0.07			
	MgO	15.57			
	CaO	22.20			
	Cr2O3	0.99			
	Na2O	0.68			
SP	TiO2	0.10	0.0156		
	Al2O3	53.65			
	FeO	12.03			
	MnO	0.04			
	MgO	19.92			
	Cr2O3	12.77			
	NiO	0.21			

F=0.12

			MODE	BULK	
OL	SiO2	40.44	0.6886	SiO2	43.69
	FeO	9.51		TiO2	0.04
	MnO	0.19		Al2O3	2.40
	MgO	49.42		FeO	8.45
	CaO	0.03		MnO	0.15
	NiO	0.32		MgO	42.82
OPX	SiO2	53.75	0.2282	CaO	1.74
	TiO2	0.07		Cr2O3	0.45
	Al2O3	5.36		Na2O	0.04
	FeO	6.68		NiO	0.22
	MnO	0.08		SUM	100.00
	MgO	32.21			
	CaO	0.82			
	Cr2O3	0.72			
CPX	SiO2	50.93	0.0686		
	TiO2	0.29			
	Al2O3	6.10			
	FeO	2.66			
	MnO	0.07			
	MgO	15.75			
	CaO	22.31			
	Cr2O3	1.01			
	Na2O	0.61			
SP	TiO2	0.10	0.0145		
	Al2O3	51.88			
	FeO	12.41			
	MnO	0.05			
	MgO	19.59			
	Cr2O3	14.68			
	NiO	0.21			

WHOLE ROCK COMPOSITIONS

F=0.14

			MODE	BULK	
OL	SiO2	40.48	0.7000	SiO2	43.70
	FeO	9.42		TiO2	0.03
	MnO	0.17		Al2O3	2.18
	MgO	49.40		FeO	8.42
	CaO	0.03		MnO	0.15
	NiO	0.32		MgO	43.18
OPX	SiO2	53.98	0.2240	CaO	1.62
	TiO2	0.07		Cr2O3	0.45
	Al2O3	5.07		Na2O	0.03
	FeO	6.57		NiO	0.22
	MnO	0.09		SUM	100.00
	MgO	32.41			
	CaO	0.89			
	Cr2O3	0.73			
CPX	SiO2	51.04	0.0626		
	TiO2	0.25			
	Al2O3	5.79			
	FeO	2.62			
	MnO	0.07			
	MgO	15.94			
	CaO	22.43			
	Cr2O3	1.04			
	Na2O	0.55			
SP	TiO2	0.09	0.0135		
	Al2O3	50.11			
	FeO	12.78			
	MnO	0.06			
	MgO	19.26			
	Cr2O3	16.59			
	NiO	0.21			

F=0.16

			MODE	BULK	
Ol	SiO2	40.51	0.7119	SiO2	43.72
	FeO	9.33		TiO2	0.03
	MnO	0.16		Al2O3	1.96
	MgO	49.38		FeO	8.39
	CaO	0.03		MnO	0.14
	NiO	0.31		MgO	43.55
OPX	SiO2	54.21	0.2195	CaO	1.50
	TiO2	0.06		Cr2O3	0.45
	Al2O3	4.79		Na2O	0.03
	FeO	6.45		NiO	0.23
	MnO	0.09		SUM	100.00
	MgO	32.60			
	CaO	0.96			
	Cr2O3	0.73			
CPX	SiO2	51.15	0.0562		
	TiO2	0.21			
	Al2O3	5.48			
	FeO	2.58			
	MnO	0.07			
	MgO	16.12			
	CaO	22.54			
	Cr2O3	1.06			
	Na2O	0.48			
SP	TiO2	0.09	0.0124		
	Al2O3	48.34			
	FeO	13.15			
	MnO	0.07			
	MgO	18.93			
	Cr2O3	18.50			
	NiO	0.21			

WHOLE ROCK COMPOSITIONS

F=0.18

			MODE	BULK	
Ol	SiO2	40.54	0.7244	SiO2	43.73
	FeO	9.25		TiO2	0.02
	MnO	0.15		Al2O3	1.75
	MgO	49.36		FeO	8.36
	CaO	0.03		MnO	0.13
	NiO	0.31		MgO	43.94
OPX	SiO2	54.43	0.2149	CaO	1.37
	TiO2	0.06		Cr2O3	0.44
	Al2O3	4.50		Na2O	0.02
	FeO	6.34		NiO	0.23
	MnO	0.10		SUM	100.00
	MgO	32.79			
	CaO	1.03			
	Cr2O3	0.74			
CPX	SiO2	51.26	0.0495		
	TiO2	0.18			
	Al2O3	5.18			
	FeO	2.55			
	MnO	0.07			
	MgO	16.31			
	CaO	22.66			
	Cr2O3	1.09			
	Na2O	0.41			
SP	TiO2	0.09	0.0112		
	Al2O3	46.57			
	FeO	13.53			
	MnO	0.07			
	MgO	18.60			
	Cr2O3	20.41			
	NiO	0.21			

F=0.2

			MODE	BULK	
Ol	SiO2	40.58	0.7375	SiO2	43.73
	FeO	9.16		TiO2	0.02
	MnO	0.14		Al2O3	1.54
	MgO	49.34		FeO	8.33
	CaO	0.03		MnO	0.13
	NiO	0.31		MgO	44.34
OPX	SiO2	54.66	0.2100	CaO	1.22
	TiO2	0.05		Cr2O3	0.43
	Al2O3	4.21		Na2O	0.01
	FeO	6.22		NiO	0.23
	MnO	0.10		SUM	100.00
	MgO	32.98			
	CaO	1.10			
	Cr2O3	0.74			
CPX	SiO2	51.37	0.0425		
	TiO2	0.14			
	Al2O3	4.87			
	FeO	2.51			
	MnO	0.07			
	MgO	16.49			
	CaO	22.77			
	Cr2O3	1.11			
	Na2O	0.35			
SP	TiO2	0.08	0.0100		
	Al2O3	44.80			
	FeO	13.90			
	MnO	0.08			
	MgO	18.27			
	Cr2O3	22.32			
	NiO	0.21			

WHOLE ROCK COMPOSITIONS

F=0.22

			MODE	BULK	
Ol	SiO2	40.61	0.7513	SiO2	43.73
	FeO	9.07		TiO2	0.01
	MnO	0.12		Al2O3	1.34
	MgO	49.32		FeO	8.31
	CaO	0.03		MnO	0.12
	NiO	0.31		MgO	44.76
OPX	SiO2	54.89	0.2049	CaO	1.07
	TiO2	0.05		Cr2O3	0.41
	Al2O3	3.92		Na2O	0.01
	FeO	6.11		NiO	0.24
	MnO	0.11		SUM	100.00
	MgO	33.17			
	CaO	1.17			
	Cr2O3	0.74			
CPX	SiO2	51.48	0.0351		
	TiO2	0.10			
	Al2O3	4.56			
	FeO	2.47			
	MnO	0.07			
	MgO	16.68			
	CaO	22.89			
	Cr2O3	1.14			
	Na2O	0.28			
SP	TiO2	0.08	0.0087		
	Al2O3	43.03			
	FeO	14.27			
	MnO	0.09			
	MgO	17.95			
	Cr2O3	24.23			
	NiO	0.21			

F=0.25

			MODE	BULK	
Ol	SiO2	40.66	0.7733	SiO2	43.72
	FeO	8.94		TiO2	0.01
	MnO	0.11		Al2O3	1.06
	MgO	49.29		FeO	8.27
	CaO	0.03		MnO	0.11
	NiO	0.31		MgO	45.42
OPX	SiO2	55.23	0.1967	CaO	0.82
	TiO2	0.04		Cr2O3	0.36
	Al2O3	3.49		Na2O	0.00
	FeO	5.93		NiO	0.24
	MnO	0.12		SUM	100.00
	MgO	33.46			
	CaO	1.27			
	Cr2O3	0.75			
CPX	SiO2	51.64	0.0233		
	TiO2	0.04			
	Al2O3	4.10			
	FeO	2.41			
	MnO	0.07			
	MgO	16.96			
	CaO	23.06			
	Cr2O3	1.17			
	Na2O	0.18			
SP	TiO2	0.07	0.0067		
	Al2O3	40.37			
	FeO	14.83			
	MnO	0.11			
	MgO	17.45			
	Cr2O3	27.10			
	NiO	0.21			

MELT COMPOSITIONS

MELT (F: 0-0.02)	
SiO2	41.31
TiO2	0.47
Al2O3	15.86
FeO	10.49
MnO	0.43
MgO	26.03
CaO	5.89
Cr2O3	-1.21
Na2O	0.64
NiO	0.09
SUM	100.00

MELT (F: 0.02-0.05)	
SiO2	41.63
TiO2	0.43
Al2O3	15.01
FeO	10.34
MnO	0.42
MgO	26.33
CaO	6.05
Cr2O3	-0.89
Na2O	0.59
NiO	0.09
SUM	100.00

MELT(F: 0.05-0.08)	
SiO2	42.00
TiO2	0.38
Al2O3	14.03
FeO	10.17
MnO	0.42
MgO	26.66
CaO	6.24
Cr2O3	-0.52
Na2O	0.52
NiO	0.09
SUM	100.00

MELT (F: 0.08-0.1)	
SiO2	42.31
TiO2	0.35
Al2O3	13.22
FeO	10.02
MnO	0.42
MgO	26.91
CaO	6.41
Cr2O3	-0.21
Na2O	0.47
NiO	0.09
SUM	100.00

MELT (F: 0.1-0.12)	
SiO2	42.56
TiO2	0.32
Al2O3	12.61
FeO	9.92
MnO	0.42
MgO	27.06
CaO	6.56
Cr2O3	0.04
Na2O	0.42
NiO	0.09
SUM	100.00

MELT (F: 0.12-0.14)	
SiO2	42.82
TiO2	0.29
Al2O3	11.90
FeO	9.79
MnO	0.42
MgO	27.35
CaO	6.67
Cr2O3	0.29
Na2O	0.38
NiO	0.09
SUM	100.00

MELT (F: 0.14-0.16)	
SiO2	43.07
TiO2	0.26
Al2O3	11.29
FeO	9.68
MnO	0.42
MgO	27.50
CaO	6.82
Cr2O3	0.54
Na2O	0.34
NiO	0.09
SUM	100.00

MELT (F: 0.16-0.18)	
SiO2	43.32
TiO2	0.23
Al2O3	10.67
FeO	9.57
MnO	0.42
MgO	27.65
CaO	6.98
Cr2O3	0.79
Na2O	0.29
NiO	0.09
SUM	100.00

MELT COMPOSITIONS

MELT (F: 0.18-0.2)	
SiO2	43.57
TiO2	0.19
Al2O3	9.97
FeO	9.45
MnO	0.42
MgO	27.94
CaO	7.08
Cr2O3	1.04
Na2O	0.25
NiO	0.09
SUM	100.00

MELT (F: 0.2-0.22)	
SiO2	43.82
TiO2	0.17
Al2O3	9.35
FeO	9.34
MnO	0.42
MgO	28.09
CaO	7.24
Cr2O3	1.29
Na2O	0.21
NiO	0.09
SUM	100.00

MELT (F: 0.22-0.25)	
SiO2	44.13
TiO2	0.13
Al2O3	8.55
FeO	9.20
MnO	0.42
MgO	28.30
CaO	7.42
Cr2O3	1.61
Na2O	0.15
NiO	0.09
SUM	100.00

MELT (F: 0-0.25)	
SiO2	42.75
TiO2	0.29
Al2O3	12.10
FeO	9.83
MnO	0.42
MgO	27.24
CaO	6.66
Cr2O3	0.23
Na2O	0.39
NiO	0.09
SUM	100.00